UNIVERSITY OF OSLO
Department of Physics

Hydrogen-related defects in hydrothermally grown ZnO studied by Fourier Transform Infrared Spectroscopy

Thesis submitted for the degree of Master of Science in Materials, Energy and Nanotechnology

Halvard Haug

June 2010

A molecule of hydrogen ... whether in Sirius or in Arcturus, executes its vibrations in precisely the same time. Each molecule, therefore, throughout the universe, bears impressed on it the stamp of a metric system as distinctly as does the metre of the Archives at Paris ...

- James Clerk Maxwell, 1873

Acknowledgments

First of all, I want to thank my main supervisor Bengt Svensson for introducing me to the exciting field of semiconductor physics, and for all the good advice, fruitful discussions and revising that made my thesis possible.

I also want to thank my co-supervisor Truls Norby for helping me remember that there is always more to it than just physics, and for guiding and inspiring me many times during all my five years at the university.

Klaus Magnus Johansen deserves a big thanks, I think we have had a very fruitful collaboration these last months. Thank you for helping with SIMS measurements and revising my thesis, and for being generally interested and a good discussion partner in the process of interpreting the data.

A big thanks goes to Viktor Bobal for helping me during countless hours of repairing and calibrating the old spectrometer and to Hans Normann, who willingly has used of his time to help and instruct me.

Thank you also to Ole Bjørn Karlsen for very much help in the process of making ampoules, and to all the people in the Solid State Ionics group who have helped me around in your lab. A special thanks goes to my friend Einar Vøllestad for helpful feedback.

On the social side, I have to thank my good friend and accomplice Magnus Kvalbein for making the office environment in the dungeon of MiNaLab an enjoyable place to be. Thank you also to all the other great people in the Physical Electronics group for welcoming me and giving me a nice and rewarding stay at MiNaLab.

The biggest thanks of all goes to my dear Kristine, for being such a wonderful person. Thank you for getting me up in the morning, motivating me when my inspiration was low and experiments failed, and for tolerating long working hours during these last months.

Halvard Haug, Oslo, May 2010

Abstract

Hydrogen is an important impurity in ZnO, and it is believed to act as a shallow donor and to passivate acceptors in the material. H is readily associated with other defects in ZnO, forming complexes with characteristic localized vibrational modes (LVMs). The H-related peaks observed in the IR absorption spectra of ZnO is thus highly dependent on the concentration of other impurities and native defects.

In this work, H-related defects in hydrothermally (HT) grown ZnO single crystals have been investigated by Fourier Transform Infrared Spectroscopy (FTIR), Secondary Ion Mass Spectrometry (SIMS) and four point resistivity measurements.

Due to a high concentration of Li acceptors, the LVM of a OH-Li complex dominates the IR spectra of the as-grown samples. Several other H-related peaks are however also observed. The results presented in this work indicate that the 3577 cm^{-1} peak associated to the OH-Li defect exhibits a complex annealing dependency, which may be explained by a process involving diffusion and recapture of H. Also, dissociation of the defect occurs at substantially lower temperatures than the previously reported thermal stability of 1200 °C. The absorption cross section of the OH-Li signal has been estimated to be $\epsilon_{3577} \geq 1.27 \cdot 10^{-17}$ cm.

A group of IR absorption peaks at 4216, 4240 and 4246 cm^{-1} have also been observed in the IR spectra of as-grown samples. By comparison with SIMS measurements, the previous identification of these peaks as internal electronic transitions of substitutional Ni^0_{Zn} impurities has been verified. The absorption cross section of the peaks has been found to be $\epsilon_{Ni} \geq 2.91 \cdot 10^{-17}$ cm.

Several other H-related peaks appeared in the IR spectra recorded after annealing of the samples in H_2 and/or D_2 atmospheres, caused by diffusion of H/D into the crystals. Two IR absorption peaks at 3303 and 3321 cm^{-1} were assigned to the LVMs of a defect complex labeled H-X, consisting of two O-H bonds associated to an unknown impurity atom. The 3321 cm^{-1} mode is oriented along the c-axis of ZnO, while the 3303 cm^{-1} mode is oriented at an angle with the c-axis. The H-X complex is thermally stable up to $\approx$ 600 °C and the activation energy for

dissociation was estimated to be 2.8 eV.

An IR absorption peak at 2783 cm^{-1} was also observed after hydrogenation. This peak was assigned to the LVM of a defect complex labeled H-Y, involving a single O-H bond oriented at an angle with the c-axis. Also, a pair of peaks at 3347 and 3374 cm^{-1} were observed in both as-grown and hydrogenated samples after annealing at $\sim$ 500 °C. These peaks were assigned to the LVMs of two O-H bonds associated to the same defect, labeled H-Z. The H-X defect is to our knowledge not reported in the literature. The H-Y and H-Z defects have previously been identified as OH-Ni_{Zn} $(OH)_2$-Cu_{Zn} complexes, respectively. However, the SIMS and IR absorption data presented in this work indicate that both these assignments should be revisited.

The H_2 and/or D_2 gas anneals were also followed by a substantial drop in resistivity, which was found to be stable after annealing at 200 °C. The resistivity however increased markedly after subsequent annealing at higher temperatures (>500 °C). The increased carrier density after hydrogenation is presumably caused by a combination of thermally stable H donors like H_O and H passivation of acceptors present in the as grown samples, forming neutral complexes like OH-Li_{Zn}.

Contents

Chapter 1

Introduction

Since the invention of the first semiconductor transistor in 1947, semiconductor materials have become a dominating part of our daily life. Semiconductor materials are the foundation of all modern electronics and have enabled our progress into the era of communication. Semiconductors are also used as the key materials for harvesting the sun's energy in photovoltaic solar cells, which are expected to contribute to a large fraction of the worlds supply of electrical energy in the future [1].

Silicon (Si) is and will remain the dominating semiconductor material, as it is widely abundant, has a strongly developed fabrication technology and excellent properties for a wide range of applications. Si has an indirect band gap, and is therefore normally not suitable for optoelectronic devices. For such applications, direct band gap semiconductors like GaAs are currently the materials of choice. However, for applications that require high temperature, high power or emission of blue or ultraviolet light, semiconductors with a wider band gap are needed [2].

Zinc oxide (ZnO) is an example of such a direct, wide band-gap semiconductor, and it has many promising properties for blue and ultraviolet optoelectronics, sensor applications and spintronic devices, among other things. It also possesses the unique property of being a transparent electrical conductor. Because of this, ZnO are currently evaluated as a transparent electrode in solar cells and might be an important material in future transparent electronics, e.g. flat screen displays [3].

Despite these promising opportunities, there is still much that needs to be learned about ZnO before commercially available electronic devices may be realized. ZnO is inherently n-type in the as-grown state, and reproducible and stable p-type conductivity in ZnO is yet to be shown. The reason for this and possible solutions are among the issues still under debate. Generally, there is a lack of control

and knowledge over dopants and defects in the material. Fundamental research on defects in general and how they affect the materials electrical and optical properties is therefore of great importance [4].

A particularly interesting impurity is hydrogen. H is believed to be one of the most abundant impurities in ZnO [5] and can be incorporated during crystal growth [6]. Moreover, ZnO has shown to take up H from H_2 gas at elevated temperatures, and H can easily diffuse into ZnO samples due to a high mobility in the material [7]. Hydrogen has been shown to behave as a shallow donor [8] and to passivate acceptors [9] in ZnO, thereby contributing to the n-type conductivity of the material.

As in many other oxides, hydrogen impurities in ZnO are normally closely bound to one of the host oxygen ions, creating a strong O-H bond. These bonds give rise to a localized vibrational mode with a frequency that is higher than the vibrational frequencies of the host crystal, and they can thus be studied using infrared absorption spectroscopy. OH^- ions may easily form complexes with both native defects and impurities in ZnO, which will influence the vibrational frequency of the O-H bond. H may thus be used as a sensitive probe of its local chemical environment [10].

In this thesis, we will attempt to gain a further understanding of the role of H-related defects in hydrothermally (HT) grown ZnO single crystals, using Fourier Transform Infrared Spectroscopy (FTIR) as the main characterization tool. H has previously been found to passivate Li acceptors [6], forming a neutral OH-Li complex which may be observed as the dominant absorption line in as-grown samples [11]. The thermal stability of the OH-Li complex and other H-related defects present in HT ZnO is however not well understood. A particular focus will therefore be put on this subject.

In addition, hydrogen and deuterium deliberately introduced into the crystals by annealing in H_2/D_2 atmospheres will be used as a subject of investigation. Secondary Ion Mass Spectrometry (SIMS) will be used for accurate determination of the concentration of different impurities in the sample. By combining the IR absorption studies with the SIMS data and previous literature, the main H-related defects and their most prominent characteristics may be identified.

By performing four point resistivity measurements after the various hydrogenation and annealing steps in this work, the effect of H on the electrical properties of ZnO will also be investigated. Hopefully, the combination of these studies may lead us one step further towards a complete understanding of the role of H in ZnO.

Chapter 2

Background and theory

In this chapter some relevant theory of vibrational motion in molecules and solids are presented. This is then used to explain the main principles of IR absorption spectroscopy, with a particular focus on the study of H impurities in oxides. First however, some basic semiconductor theory including crystals and crystal defects are briefly described. These sections are based on textbooks in material science [12] and semiconductor physics [13], and further literature can be found there.

2.1 Basic theory

2.1.1 Crystals and defects

A crystal is a solid material, where the constituent atoms or ions are arranged in an orderly repeating pattern. Crystals are described by a mathematical crystal lattice with one or more atoms (the basis) repeated at each lattice point. Such a perfect crystal is only theoretically possible at 0 K. At real temperatures deviations will occur because of entropy. Such deviations are called defects, and may be 0- 1- 2- or 3-dimensional. Only 0-dimensional (point) defects will be considered in this thesis. Vacancies, host atoms displaced from their normal positions and impurities are common examples of point defects. Many properties of crystalline solids are dependent on these small imperfections.

In semiconductor physics point defects are commonly described using the following notation:

$$X_s^c, \tag{2.1}$$

where M is the species, which may be a host atom, an impurity atom/molecule or a vacancy (V). S indicate the lattice site that the species occupies. If the species is located in an interstitial position the symbol "i" is used[1]. C corresponds to the electronic charge of the species *relative to the site that it occupies*. A (monovalent) Li atom residing on a (divalent) Zn site is thus written as Li_{Zn}^{-}. Defects in semiconductors may commonly have more than one possible charge state, so the charge is not always specified. Free electrons and holes are not bound to a specific lattice site and are written as e^{-} and h^{+}, respectively [12].

2.1.2 Semiconductor theory

When several atoms are brought together to form a solid crystal, the discrete energy levels of the atoms are "spread out", forming energy bands of allowed states for the electrons. As a consequence of the periodicity of the lattice, there will be some energy intervals without any electron states available. The way the electrons fill up these bands determines the main electrical properties of the material. Metals have half-filled or overlapping bands, so that the electrons have many available states they can move into, making the metal a good electronic conductor. An insulator have a completely filled band, called the valence band, separated from a completely empty band, called the conduction band. The forbidden energy interval between these two bands is called the band gap. Since there are no available states in the valence band and no electrons in the conduction band, no electrical conduction can occur. A semiconductor is similar to an insulator, but with a smaller band gap. At 0 K the semiconductor is insulating, but as the temperature increases, electrons can be thermally excited across the band gap. One such event gives rise to an electron in the conduction band and a hole in the valence band, together called an electron-hole pair. Both of these can conduct electricity. Electrons and/or holes may also be introduced in a semiconductor from charged defects like heterovalent impurities. When done on purpose, this process is called doping. A semiconductor is said to be n-type if electrons are the main charge carriers and p-type if holes are dominating. The Fermi level (or Fermi energy) E_F is defined by the electron with the highest energy at 0 K. At non-zero temperatures the distributions of filled and empty states are still symmetrical around the Fermi energy, making it a useful point of reference for calculating carrier concentrations in semiconductors [13].

[1] In this work, the additional symbols *BC* (bond centered), *AB* (antibonding), $||$ and $\perp$ are used to indicate different interstitial positions. See figure 3.2 for details.

2.2 Theory of vibrational spectroscopy

Light may interact with matter in different ways, with the interaction depending on the wavelength of the radiation. A measurement of the spectral response of this interaction is called spectroscopy, a useful tool for reflecting the physical (e.g. the electronic or structural) properties of a material. Infrared (IR) spectroscopy is the study of the interaction between IR light and matter. It covers a range of techniques, the most common being absorption spectroscopy, which exploits the fact that chemical bonds absorb radiation at specific frequencies that are characteristic of their nature and chemical environment. IR spectroscopy can therefore be used to investigate the chemical composition of a sample [14]. To understand the principles of vibrational spectroscopy of solid samples, some knowledge of the vibrational motion of atoms is necessary. In this section, the theory behind the vibrational motion of diatomic molecules is given, before the more complex situation of vibrational modes in three dimensional crystals is outlined. A more comprehensive description of the Fourier Transform Infrared Spectroscopy (FTIR) technique is given in section 4.1.

2.2.1 Molecular vibrations

Classical view

As a first approximation, vibrational motion in molecules can be considered using Newtonian mechanics, where the atoms are modeled as point masses connected with massless springs. If the displacement x is small, the force between two atoms in a diatomic molecule is proportional to the displacement from the equilibrium position, according to Hook's law [15]:

$$F = -kx. \tag{2.2}$$

Here, k is the force constant, in units of N/m. This assumption is called the harmonic approximation. By Newtons second law, the spring force is equal to the reduced mass of the molecule μ times the acceleration of one of the atoms with respect to the other:

$$-kx = \mu \frac{d^2x}{dt^2}. \tag{2.3}$$

The solution to this differential equation is a simple harmonic motion, e.g.

$$x(t) = A\,cos(\omega t), \tag{2.4}$$

where A is the amplitude and t is the time. The angular frequency, defined as 2π times the frequency f, is given by

$$\omega = \sqrt{\frac{k}{\mu}}. \tag{2.5}$$

For a heteronuclear diatomic molecule consisting of two masses m_1 and m_2, the reduced mass is defined as

$$\mu = \frac{m_1 m_2}{m_1 + m_2}. \tag{2.6}$$

Perhaps surprisingly, this simple classical calculation of molecular vibrations gives an accurate description of the vibrational frequencies in molecules, as long as the harmonical approximation holds. However, to understand IR spectroscopy, the interactions between light and vibrational modes must be considered. For this, the classical model can no longer be applied.

Quantum mechanical view

The spring force described in eq. 2.2 gives rise to the one-dimensional potential

$$U(x) = \frac{1}{2}kx^2. \tag{2.7}$$

The quantum mechanical equivalent of the derivation in the previous section is to solve the Schrödinger equation for a particle moving in such a potential

$$-\frac{\hbar}{2m}\frac{d^2\psi}{dx^2} + \frac{1}{2}kx^2 = E\psi. \tag{2.8}$$

The solution of this differential equation is not straightforward, but can be found in various textbooks [16]. The vibrational energy in a quantum mechanical harmonic oscillator is found to be

$$E_{vib} = \hbar\omega(n + \frac{1}{2}), \tag{2.9}$$

where $\hbar = \frac{h}{2\pi}$ is the reduced Planck's constant ($1.05457 \cdot 10^{-34}$ Js) and ω is defined as before. The vibrational quantum number n can take integer values 0, 1, 2, etc, and characterizes the different eigenstates of the harmonic oscillator. Notice that there

exists a lowest possible energy $E_0 = \frac{1}{2}\hbar\omega$, which is called the *zero-point energy* [16].

2.2.2 Vibrational spectroscopy

An incoming photon with energy equal to the energy difference between two eigenstates of the vibrational mode can be absorbed in the mode, exciting it to a higher eigenstate n. In vibrational spectroscopy, it is common to use the *wave number* unit $\tilde{\nu}$ instead of the frequency to describe vibrational modes. The wave number is given as the number of wavelengths of light per cm,

$$\tilde{\nu} = \frac{1}{\lambda} = \frac{f}{c} = \frac{\omega}{2\pi c}, \tag{2.10}$$

where c is the speed of light, $c = 2.9979 \cdot 10^{10}$ cm/s. The wave number unit is linear with energy, with E = $1.24{\cdot}10^{-4}$ $\tilde{\nu}$ in electron volts. The energy difference for transitions between the ground state (n=0) and the first excited state (n=1) of most vibrational stretch modes lies in the range of the mid-infrared spectrum, that is, from $\tilde{\nu}$ = 400 to 4000 cm^{-1} [17]. Studies of IR absorption is therefore an excellent tool to probe for vibrational modes in both gases, liquids and solids.

However, not all vibrational modes are detectable by IR absorption spectroscopy. The absorption of a photon follows from interaction between the mode and the time-varying electrical field of the incoming light. Hence, for a vibrational mode to absorb IR radiation, the bond must be polar, so that the dipole moment of the bond changes with time. As a result of this, symmetrical stretching modes like that of the N_2 molecule are not detectable by conventional IR spectroscopy. In such cases, another technique called Raman spectroscopy may be applied. Raman measurements rely on inelastic scattering, or Raman scattering, of monochromatic light. Raman-active vibrations are governed by different rules than those that govern direct IR absorption; that is, there must be a change of polarizability of the molecule during the vibration. Hence, the vibrations in the Raman spectrum are most often symmetrical modes, giving similar, but complementary information to that of IR absorption spectroscopy [18]. In the rest of this thesis, the focus will lie on conventional vibrational spectroscopy of solid state samples.

2.2.3 Vibrational modes in crystals - phonons

In this section, a simplified summary of lattice vibrations in crystals are given, as treated by the textbooks in solid state physics by Ashcroft [19] and Kittel [20].

In three-dimensional crystals, the displacement of one or more atoms from their equilibrium positions will generally not lead to a localized vibration as in the treatment above. Instead, a set of vibration waves propagating through the lattice are formed. A full treatment of such a system would involve calculating all the forces on all the particles originating from the potential energy function of the entire lattice

$$V_{lattice} = \sum_{i,j} V(r_i - r_j), \tag{2.11}$$

where r_i is the position of the ith atom and V is the potential between a pair of atoms. Solving this many-body problem is extremely complicated, so several simplifications are usually applied. By only considering nearest-neighbour interactions and assuming harmonic potentials, the lattice can be modeled as a grid of N masses connected with springs, giving a total of 3N coupled harmonic oscillators. The *normal modes* of of this system are the simplest type of solutions of the equations of motion, where all the masses oscillate with the same frequency. These modes are important because an excitation of one mode will never cause motion of a different mode, and any general motion of the system can be considered as a superposition of such modes. In this way, a collection of coupled oscillators can be reduced to a set of decoupled, effective oscillators.

It can be shown that to specify the energy levels of a N-ion harmonic crystal, one may regard it as 3N independent oscillators, with frequencies given by the 3N classical normal modes described above. As the allowed energies of a quantum mechanical harmonic oscillator are quantified, the contribution to the total energy from a particular normal mode s will also be quantified, and is given by the discrete values:

$$E_s = \hbar\omega_s(n_s + \frac{1}{2}), \tag{2.12}$$

where $n_s = 0, 1, 2, ...$ is the excitation number of the normal mode. This quantization of energy is analogous to the quantum theory of electromagnetic waves, where the quantization of light is described by particles called photons. In the same way, instead of saying that a specific normal mode is in its n_sth state, it is more common to state that there are n_s *phonons* of type s present in the crystal. Phonons are quasiparticles that carry lattice vibrations through the lattice and play a major part in many of the physical properties of solids, including electrical and thermal conductivity.

Phonons in solids may be of longitudinal polarization, where the atoms vibrate in the same direction as the propagation of the wave, or of transverse polarization, where the atoms vibrate in a plane perpendicular to the wave. For crystals with two or more atoms in their primitive unit cell, there are two types of phonons: acoustic phonons and optical phonons. Acoustic phonons correspond to sound waves in the lattice, with neighbouring atoms vibrating together. The frequencies of these phonons go to zero at long wavelengths. In optical phonons neighbouring atoms vibrate against each other, with opposite velocities. These vibrations can be considered as molecular vibrations within each unit cell, somewhat broadened out by weak interactions between the cells. If the two types of atoms carry different charges, they will create a time-varying electrical dipole moment. Phonons of this type can therefore easily be excited by interaction with electromagnetic radiation, normally in the far-infrared range.

ZnO has four atoms in the primitive unit cell, giving 12 different classes of phonons, one longitudinal acoustic (LA), two transverse acoustic (TA), three longitudinal optical (LO) and six transverse optical (TO) [2].

2.2.4 Localized vibrational modes

If point defects are present in a crystal, the translational symmetry of the lattice is destroyed and the normal modes of vibration are altered. If a modified mode lies within the frequencies of the optical or acoustic bands of the perfect lattice, then any disturbance of the mode can propagate throughout the crystal. These modes are called *band modes*. If the modified mode has a frequency that lies outside these bands, a disturbance will be spatially localized around the defect, with the amplitude of vibration decreasing exponentially with distance. These modes are called *localized vibrational modes* (LVMs) [21].

2.2.5 The OH^- ion

Hydrogen impurities in oxides are usually closely bound to one of the host oxygen ions, and can therefore be regarded as a OH^- ion substituting on an oxygen site, or OH_O^+ in defect notation [10]. A value for the spring force constant k of a free O-H-bond can be found in tables [22] to be $k = 780$ N/m. Inserting this into in eq. 2.13 gives a value for the O-H stretch frequency of $\omega_H = 7.065 \cdot 10^{14}\, s^{-1}$, or $\tilde{\nu}_H$=3748 cm^{-1} in terms of wave numbers.

In ZnO, strong absorption bands from the interaction between incoming light

and various combinations of optical phonons are observed in the range 800 - 1200 cm^{-1} [23]. As the O-H vibrational frequency is significantly higher than the optical phonon frequency in most materials, vibrational modes from O-H-defects in the crystal lattice behave as localized modes, with a frequency only somewhat perturbed by the surrounding crystal lattice. Because of these interactions and anharmonic effects (see section 2.2.7) the O-H stretch frequencies are shifted to somewhat lower values, and have been measured in the range of 3200-3700 cm^{-1} in a large variety of oxides. The interaction with the atoms surrounding the O-H-bond gives rise to a characteristic vibrational frequency that can be used for identification of a specific defect configuration[2]. Hence, IR vibrational spectroscopy is a particularly useful tool to study various H-related defects in oxides [10].

2.2.6 Isotopic shifts

Notice that from eq. 2.5, the frequency of a vibrational mode is higher when the force constant is stronger and when the involved masses are lighter. The latter effect is commonly used in vibrational spectroscopy to determine which atoms that are involved in a specific vibrational mode. Returning to a heteronuclear, diatomic molecule, we can calculate the shift in the wave number of the vibrational mode as a function of the two masses. By combining eqs. 2.5 and 2.6 we get an expression for the angular frequency of heteronuclear bond between masses m_A and m_B

$$\omega = \sqrt{\frac{k}{\mu}} = \sqrt{\frac{m_A + m_B}{m_A m_B} k}. \tag{2.13}$$

If one of the elements is replaced by one of its isotopes a chemically (almost) equivalent bond results, but the frequency will shift due to the change in the reduced mass. If m_B is replaced by m_B^*, this shift is given by

$$\frac{\omega}{\omega^*} = \sqrt{\frac{\mu^*}{\mu}} = \sqrt{\frac{(m_A + m_B)(m_A m_B^*)}{(m_A + m_B^*)(m_A m_B)}}. \tag{2.14}$$

This technique is particularly useful for bonds involving hydrogen, because of the relatively big difference in mass between hydrogen and its isotope deuterium. Eq. 2.14 may be applied to an isolated oxygen-hydrogen bond, with $m_A = m_O =$ 16.00 atomic mass units (amu), $m_B = m_H =$ 1.00 amu and $m_B^* = m_D =$ 2.00 amu, giving a isotopic frequency shift of

[2] See tables 3.1 and 3.2 for examples from ZnO

$$\frac{\omega_{OH}}{\omega_{OD}} = \frac{\tilde{\nu}_{OH}}{\tilde{\nu}_{OD}} = 1.374. \tag{2.15}$$

This value is also approximately true for many vibrational modes involving oxygen-hydrogen bonds in oxides, with typical reported values for O-D bonds in the range 2350 - 2750 cm^{-1} [10]. Substitution of hydrogen with deuterium may therefore give strong evidence of that a certain vibrational mode arises from an O-H bond.

2.2.7 Anharmonic effects

In all the derivations until now, the harmonic approximation has been assumed to be valid. The real potential however deviates somewhat from the one in eq. 2.7. Normally this is solved by replacing U(x) with an anharmonic, or Morse-type, potential function. The solution for the vibrational energies then becomes

$$E_{vib} = \hbar\omega_e[(n + \frac{1}{2}) - \chi_e(n + \frac{1}{2})^2], \tag{2.16}$$

where ω_e is the harmonic frequency and χ_e is a dimensionless anharmonicity constant. χ_e typically takes values between 0.01 and 0.05 [10].

As described in the previous section, the frequency ratio between the O-H and O-D stretch modes is given by $\eta^{-1} \equiv \sqrt{\frac{\mu_H}{\mu_D}} = 1.374$ in the harmonic approximation. The small deviations from this value that are normally observed in experiments can be explained by the anharmonicity of the vibrational potential. As derived in appendix A.3, $\tilde{\nu}$ and χ_e can be calculated from the measured frequency shift R and the theoretical shift η^{-1} using the following relations [10]:

$$\chi_e = \frac{1 - R\eta}{2(1 - R\eta^2)}, \tag{2.17}$$

$$\tilde{\nu}_e = \frac{\tilde{\nu}_{OH}}{1 - 2\chi_e}. \tag{2.18}$$

2.2.8 Other absorption mechanisms

Radiation can be absorbed in matter by many different mechanisms. In this section, other absorption mechanisms that will be used in later discussions are described.

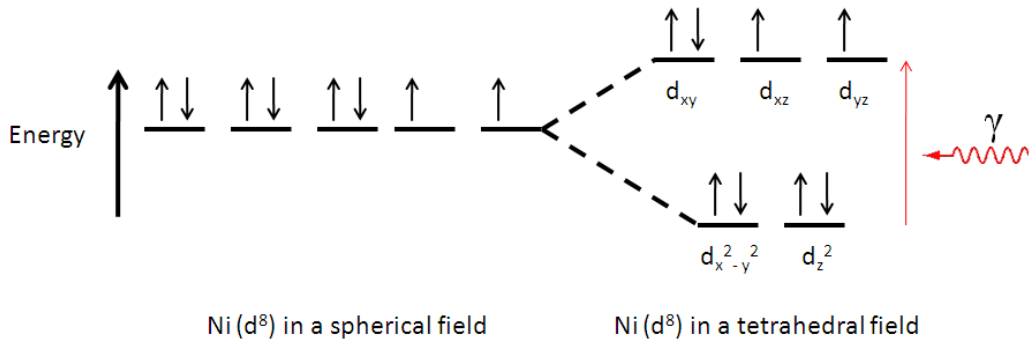

Figure 2.1: Crystal field splitting of the d-orbitals of a Ni ion in a tetrahedral configuration. Edited from [18].

Free electron absorption

Free carriers in the semiconductor valence- or conduction band, arising from electrically active defects and impurities in the crystal, may give a significant contribution to the IR absorption by the sample. The conduction band electrons can be excited by any photon energy into the continuum of higher energy states in the band, and similarly for the holes in the valence band. Free electron absorption is therefore visible over the whole IR spectrum, varying as a function of wave number. The wave number dependency of the absorption is characteristic of the dominant scattering mechanism in the sample. IR spectroscopy may therefore also provide a signature related to the scattering processes and carrier transport in the material [23].

Internal electronic transitions in impurities

When substitutional impurities of transition metals are present in the crystal lattice, the energy of the five atomic d-levels of the metal ion will depend on the local crystal field. The electronic structure of the host lattice will give a splitting of the energy of the d-levels, resulting in a loss of degeneracy. The splitting is affected by the nature of the metal ion and the lattice, the symmetry of the lattice site and the metal oxidation state. Light can be absorbed by exciting an electron from one d-level to another lying higher in energy, giving rise to characteristic absorption lines. The process is illustrated in figure 2.1, where the splitting of the Ni d-levels in a tetrahedral field is used as an example. The energy involved in such transitions may be located in the infrared part of the spectrum, making IR transmission experiments also suitable for studies of this kind of defects [24].

2.3 Infrared transmission measurements

The simplest geometry for a IR absorption measurement is a transmission experiment. As radiation passes through a sample, the intensity decreases exponentially with the sample thickness d:

$$I(\tilde{\nu}) = I_0(\tilde{\nu})e^{-\alpha(\tilde{\nu})d}, \tag{2.19}$$

where the decay constant $\alpha(\tilde{\nu})$ is called the *linear absorption coefficient*. The intensity ratio between the incoming and outgoing light I/I_0 is defined as the *transmittance* T. In eq. 2.19, the losses in intensity due to reflectance from the sample surfaces have been neglected. The fraction of the incident radiation at a wave number $\tilde{\nu}$ that is reflected from a surface is called the *reflectance* $R_{\tilde{\nu}}$ and is given by

$$R_{\tilde{\nu}} = \frac{(n_{\tilde{\nu}} - 1)^2 + \kappa_{\tilde{\nu}}^2}{(n_{\tilde{\nu}} + 1)^2 + \kappa_{\tilde{\nu}}^2}, \tag{2.20}$$

where $n_{\tilde{\nu}}$ is the refractive index and $\kappa_{\tilde{\nu}}$ is the extinction coefficient of the material [25]. As the beam can be reflected from both the front and back surface of the sample, the total transmitted intensity will be given as the sum of the directly transmitted and all the multiply reflected beams:

$$I = I_0(1-R)^2e^{-\alpha d} + I_0(1-R)^2R^2e^{-\alpha 3d} + I_0(1-R)^2R^4e^{-\alpha 5d} + ... \tag{2.21}$$

$$= \frac{I_0(1-R)^2e^{-\alpha d}}{1 - R^2e^{-2\alpha d}}. \tag{2.22}$$

The refractive index of ZnO is fairly constant at $n_{\tilde{\nu}} = 1.9$ [26] and $\kappa_{\tilde{\nu}}$ is small compared with unity in the wave number intervals used in this work [27], giving a constant reflectance of $R \approx 0.1$. The denominator in eq. 2.22 can therefore be taken as 1 without introducing any significant error. Also, the absorption coefficient may be written as $\alpha = \alpha_1 + \alpha_2$, where α_1 corresponds to the absorption from the host crystal and free electrons, and α_2 results from the presence of defects in the crystal lattice. eq. 2.22 can then be rewritten as

$$T = \frac{I}{I_0} = (1-R)^2e^{-(\alpha_1(\tilde{\nu})+\alpha_2(\tilde{\nu}))d} \equiv C(\tilde{\nu})e^{-\alpha_2(\tilde{\nu})d}. \tag{2.23}$$

The factor $C(\tilde{\nu})$ in this expression varies only slowly with the wave number $\tilde{\nu}$, while the impurity absorption from α_2 can be seen as sharp lines at low temperature.

Hence, measurements of the transmission at an absorption peak and on either side of it allows the contribution from a single localized vibrational mode to be measured in a simple manner [21].

Beer's law

Beer's law, named after the German physicist August Beer, relates the absorption of light transmitted through a sample to the concentration of the absorbing species. The *absorbance* at a wave number $\tilde{\nu}$, is defined as the negative natural logarithm of the transmittance. Both the absorbance and the absorption coefficient α is directly proportional to the concentration of absorbers through the relation

$$A(\tilde{\nu}) = -ln\left(\frac{I}{I_0}\right) = \alpha(\tilde{\nu})d = \epsilon cd, \tag{2.24}$$

where ϵ is the absorption cross section, c is the number density of the absorbing species and d is the sample thickness [28]. As the absorption peaks always are somewhat broadened, it is common to define the absorption cross section ϵ of a species i by means of the integrated absorption coefficient:

$$\epsilon_i = \frac{\int \alpha_i(\tilde{\nu})d\tilde{\nu}}{c_i}. \tag{2.25}$$

Beer's law holds as long as the absorbing species absorb independently of each other, that is, when there are no screening effects taking place. Hence, as long as dilute concentrations are being measured, transmission experiments may be used for both qualitative and quantitative investigations of many different compounds [14].

Chapter 3

Zinc Oxide - previous work

In this chapter, the main properties and possible applications of zinc oxide (ZnO) is described. Some motivation for the extensive research that is being done on the material is also given. A selected part of the previous work conducted on native defects and impurities in ZnO is presented, with a particular emphasis on literature related to infrared absorption and the role of various hydrogen-related defects.

3.1 General properties

Zinc oxide (ZnO) is a wide band gap semiconductor with a direct band gap of $\sim$ 3.4 eV, emitting light in the near-UV part of the spectrum. It is not a newly discovered material (characterization reports go at least back to 1935 [3]), but it has gained a renewed interest during the last decade. Among the reasons for this is that ZnO is one of the few known and readily available transparent conductors. Another particularly interesting property is the high exciton binding energy of 60 meV, resulting in a high emission efficiency at room temperature. ZnO also has some advantages over other wide band gap semiconductors like GaN in its low cost, availability and non-toxicity. Together with recent advances in crystal growth, ZnO is a promising material for optoelectronic applications and devices [29].

3.2 Applications

Even though ZnO is a promising candidate semiconductor for future devices, the material is also widely used in today's society. It is an important compound in the fabrication of paints, rubber, sunscreen and many other non-electronic products

[2]. ZnO also is an important material for varistors, used to protect circuits against excessive transient voltages [30]. Heavily n-doped ZnO is also currently used to replace $(In,Sb)_2O_3$ as a transparent conducting electrode in solar cells [31].

In the future, ZnO epitaxial layers and single crystals may also be important in the development of new devices. The high exciton binding energy makes ZnO strong candidate for optoelectronic applications like blue and UV light emitters and detectors, and may be used for solid-state white lighting [2]. ZnO also has the potential of being used as a transparent transistor, opening up for opportunities in liquid-crystal displays [32].

In addition, ZnO may become a key material for spintronic applications, where both the charge and the spin of electrons are exploited. To obtain the mixed magnetic and semiconducting properties that is needed for such applications, a semiconducting material is doped with randomly distributed magnetic elements giving a so-called *dilute magnetic semiconductor* (DMS). Numerous reports of ferromagnetism in ZnO doped with magnetic elements such as Co and Ni have inspired a great deal of research interest in the material [33], and films of ZnO doped with Co have even been reported to exhibit ferromagnetism at 300 K [34]. These reports are however not indisputable, as ferromagnetism frequently arises from secondary phases such as ZnCo. Correct identification of the involved phases and further investigations of the role of TM defects in ZnO is therefore of great importance for further development of a ZnO-based DMS [29].

3.3 Crystal structure

As many other binary semiconductors, ZnO crystallize in a cubic zinc blende or hexagonal wurtzite structure, where each atom is tetrahedrally coordinated with four atoms of the opposite type. At normal pressures and temperatures, the wurtzite structure is thermodynamically favourable. The wurtzite structure, illustrated in figure 3.1, belongs to the space group C_{6v}^4 or $P6_3mc$ and has a hexagonal unit cell described by the lattice parameters a and c, with $c/a = \sqrt{8/3} \approx 1.63$. Real ZnO crystals actually have a distorted wurtzite structure, because the ratio $c/a \approx 1.60$ deviates from the ideal case. As seen in figure 3.1, the atoms are still tetrahedrally coordinated, but the length of the bond along the c-axis is smaller than the length of the three other bonds. There are two formula units (four atoms) in each unit cell, in such a way that the zinc and oxygen ions each form a hexagonal close-packed sublattice. Since the wurtzite structure lacks inversion symmetry along the c-axis,

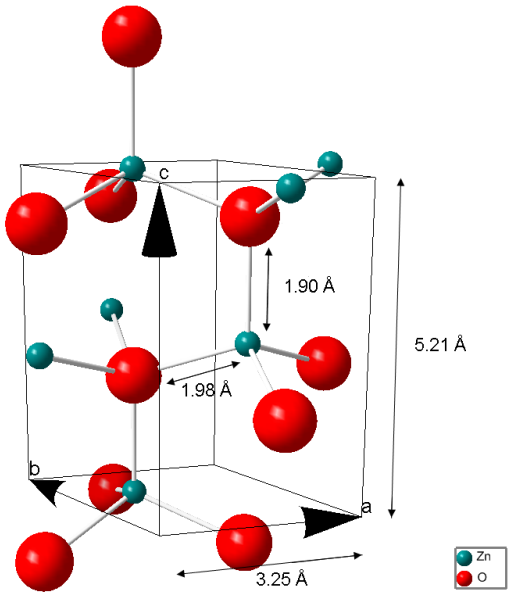

Figure 3.1: ZnO in the wurtzite structure. Bond lengths and lattice parameters are indicated

the atomic arrangement depends on which direction that is defined as the positive c-axis. The convention is that the bonds along the c-axis (in the [0001] direction) goes from cation to anion, so that the Zn-terminated side of the crystal is the $< 0001 >$ plane and the O-terminated side is the $< 000\bar{1} >$ plane. Many aspects of ZnO crystals, like etching, growth, defect concentrations and piezoelectric properties depend on this polarity [3].

The lattice parameters *a* and *c* of ZnO have been studied by several groups, using high resolution x-ray diffraction (HRXRD), reflection high energy electron diffraction (RHEED), transmission electron microscopy (TEM) and different computational methods. The lattice constants at room temperature range from 3.2475 to 3.2501 for the *a* parameter and 5.2042 to 5.2075 for the *c* parameter.

3.4 Single crystal synthesis

Bulk ZnO crystals are currently synthesized by either hydrothermal, vapor phase or melt growth techniques. The chosen method of fabrication is an important factor for both the crystal quality and the concentrations of different impurities in the resulting material [35].

3.4.1 Hydrothermal growth

In the hydrothermal (HT) synthesis technique, crystals are grown from a aqueous solvent at elevated temperature and pressure to dissolve a solute which is insoluble under ordinary conditions. The growth is then obtained by convection between the high temperature zone and a growth zone with lower temperature, where the seed crystals are placed. LiOH or KOH are commonly used as solvents, resulting in large concentrations ($\sim 10^{17}$ cm^{-3}) of lithium or potassium in the product material. As described in section 3.5.3, Li acts as a compensating acceptor in ZnO, so carrier concentrations in HT samples are usually low. Other common impurities reported in HT samples include Cu, Fe, Mn, Si, Ag, Mg and Ni. Another problem with the HT technique is a slow and anisotropic growth rate, with a growth rate in the fastest direction (the [0001] direction) of 0.06-0.25 mm/day. This gives a undesirable spatial variation in the impurity concentration that may affect device performances. On the positive side, HT growth have superior manufacturing cost, gives the best crystallographic quality and has the advantage of being scalable, making it suitable for industrial processes. Also, impurities may be readily incorporated *in-situ* during the growth, which is a clear advantage provided that the auto-doping with Li can be brought under control [5]. Commercial producers of HT ZnO include CrysTec Gmbh, Tokyo DenPa and SPC GoodWill, and samples from the latter company has been used in this work [35].

3.4.2 Vapor phase growth

Crystals of ZnO have been obtained by chemical vapor transport in open or closed tubes using several different precursors and carrier gases. Samples grown by the vapor phase (VP) method are commercially available from Eagle Picher. In their process, crystals are grown by seeded chemical vapor transport at 1000-1200 °C in horizontal tubes using H_2 as a carrier gas and a controlled amount of water vapor to maintain the right stoichiometry. Samples grown by this method usually have a lower concentration of impurities and a higher mobility and carrier density compared to HT samples [35].

3.4.3 Melt growth

ZnO is also grown directly from the melted material in a pressurized melt growth process patented by Cermet, Inc. The process is carried out under a controlled oxygen overpressure of 50 atm to obtain good stoichiometry. Kilogram-sized ingots

of high purity can be grown by this method in a reasonable time. However, it is difficult to obtain a large grain size using this technique [35].

3.5 Defects in ZnO

ZnO has many inherent advantages, but a lack of control of defects in the material hinders the realization of practical devices. Continued research on this subject is therefore of crucial importance [2]. The literature on the topic of defects in ZnO is vast, and a full overview is not attempted here. Instead, some reported properties of the common native defects and selected impurities involved in spectroscopic features in the IR-range are given. A particular weight will be given to various reported H-related defects and complexes in ZnO, treated in section 3.6. For a comprehensive summary of defects in ZnO, see reviews [3], [4] and references therein.

3.5.1 The p-type issue

As has been the case with other wide-band gap semiconductors like GaN, the main issue currently limiting the realization of ZnO-based devices is the challenge of achieving stable p-type material [2]. Even though theory predicts pure ZnO to be an intrinsic semiconductor, it is almost invariably occurring in the n-type state. The cause of this background conductivity and the difficulty in achieving p-type material is not properly understood [3]. Nevertheless, several groups have reported p-type doping of ZnO using both group I elements like Li and the group V elements N, P, As and Sb as acceptors. However, there are still problems with the reproducibility and stability of these results [4, 36].

3.5.2 Intrinsic defects

There has been some controversy in the literature regarding the origin of the prevailing n-type conductivity of ZnO. In the past, it was usually attributed to one or both of the intrinsic donors Zn_i and V_O [36]. This assignment has however been questioned by several groups [37, 38, 39]. Based on first principle calculations, both Kohan et al. [37] and Janotti and Van der Walle [40] concluded that the oxygen vacancy produces a deep donor state, with a (0/2+) level estimated to be 1-2 eV below the conduction band minimum, and therefore can not be the dominant donor at room temperature. The zinc interstitial was also ruled out because of its high

formation energy. In addition, both theory and experiments have shown that Zn_i is unstable at room temperature, with reported diffusion activation energies as low as 0.57 eV. V_O and Zn_i may however be important compensating centers, as a low formation energy has been calculated for both defects in p-type ZnO [38]. Intrinsic defects are still believed to contribute to the n-type conductivity in ZnO, but there seems to be a general consensus that impurities also has to be taken into account. Look et al. [36] have performed calculations and experiments indicating that complexes between intrinsic defects and impurities such as Zn_i-N_O and Zn_i-Li_{Zn} could act as stable, shallow donors.

According to theory, zinc vacancies and oxygen interstitials should behave as acceptors. Of the two, V_{Zn} is the most studied, as it should be prevalent in n-type ZnO grown under oxidizing conditions. Also, since it is a negatively charged open volume, it can be studied by positron annihilation spectroscopy (PAS). PAS studies by Tuomisto et al. [41] have shown V_{Zn} concentrations of $2 \cdot 10^{15} cm^{-3}$ in as-grown samples and $2 \cdot 10^{16} cm^{-3}$ in irradiated samples. These findings are in good agreement with total acceptor concentrations determined by temperature dependent Hall measurements, indicating that V_{Zn} may act as the dominant acceptor in n-type ZnO. First principle calculations find that V_{Zn} are double acceptors, with the (0/-) and (-/=) acceptor levels 0.1-0.2 eV and 0.9-1.2 above the valence band maximum.

3.5.3 Selected extrinsic defects

Common impurities

Vines et al. [42] have previously investigated several impurities in ZnO crystals produced by SPC GoodWill, similar to the samples used in this study. Both as-grown samples and samples subjected to 1 h heat treatments in ambient air at temperatures between 1100 and 1500 °C were investigated, using Secondary Ion Mass Spectrometry (SIMS). The most pronounced impurities were Mg ($\sim 5 \cdot 10^{17}$ cm^{-3}), Li ($\sim 3 \cdot 10^{17}$ cm^{-3}), Si, Al, Ni ($\sim 10^{17}$ cm^{-3}), Fe ($\sim 5 \cdot 10^{16}$ cm^{-3}) and Mn ($\sim 3 \cdot 10^{16}$ cm^{-3}). A reduction in the bulk Li concentration was observed in the annealed samples, with [Li] $\approx 10^{16}$ cm^{-3} after 1300 °C and [Li] $\approx 10^{15}$ cm^{-3} after 1500 °C. The concentration of the other mentioned elements remained fairly constant with annealing. The H concentration in the samples was below the SIMS detection limit, that is $\leq 5 \cdot 10^{17}$ cm^{-3}.

Lithium

As described in section 3.4.1, Li is a common impurity in hydrothermally grown ZnO. Li substituting for Zn acts as a shallow acceptor in ZnO [36], and it has a high solubility in the material [43]. However, p-type doping of ZnO using lithium has turned out to be difficult, because the Li interstitial Li_i has a lower formation energy than Li_{Zn} in p-type ZnO [44], and this defect acts as a compensating donor. Thus, introducing high concentrations of Li into a ZnO crystal will give a balance between Li_{Zn} and Li_i, resulting in a highly compensated, semi-insulating material [36]. It is crucial to understand whether it is possible to stabilize Li in one of the two configurations, electrically deactivate it, or completely remove it from the material [5]. Li has been shown to mainly reside in the Li_{Zn} configuration as an important acceptor in HT samples similar to the ones used in this work [42].

Transition metals

Transition metals (TMs) are common impurities in as-grown ZnO, both in substitutional and interstitial sites. Optical transitions are reported for Cu_{Zn}, Co_{Zn}, Fe_{Zn} and several oxidation states of Ni_{Zn} [45].

Several authors [46, 47] have reported relatively strong IR absorption lines at 4216, 4240 and 4247 cm^{-1} in hydrothermal ZnO. These lines were first investigated by Kaufmann et al. [24] by IR absorption measurements on ZnO crystals with Ni added to the starting material. The authors apply a theoretical model in which they conclude that the absorption lines arise from internal electronic transitions between the d-levels of substitutional Ni_{Zn} ions, in good agreement with the experimental data. The Ni lines were also reported in 1986 by Schulz and Thiede [48], in a study of emission and absorption spectra from vapor phase single crystals of ZnO doped by Co and Ni by in-diffusion.

Another common impurity in ZnO is copper [49]. In the ZnO lattice, Cu normally occupies a Zn site, giving a deep acceptor level (-/0) in the band gap at E_c-0.17 eV. Internal electronic transitions between the d-levels of the Cu atom give rise to an IR absorption line at 5781 cm^{-1} [50]. In addition, Cu, Ni and other transition metal impurities are believed to form complexes with hydrogen in ZnO. Some literature on this topic is presented in section 3.6.3

3.6 Hydrogen in ZnO

3.6.1 Solubility and diffusion

In the 1950s Thomas and Lander [7] found that heating ZnO samples in hydrogen atmospheres at elevated temperatures leads to diffusion of hydrogen into the crystals. This was followed by an increase in the electrical conductivity, indicating that H act as a donor in ZnO. By assuming that all the hydrogen is ionized at the temperatures that were used, the authors proposed the reaction

$$H_{2(g)} \rightleftharpoons 2H_i^+ + 2e^-, \tag{3.1}$$

with the equilibrium coefficient

$$K_H = \frac{[H_i^+]^2 n^2}{P_{H_2}}. \tag{3.2}$$

Here, n is the electron concentration [e^-]. If the free electrons from the hydrogen ionization are present in excess, the following electroneutrality holds:

$$[H_i^+] = n. \tag{3.3}$$

By combining eqs. 3.2 and 3.3 a relationship between the hydrogen pressure, temperature (through K_H) and the free electron concentration can be found as

$$n = K_H^{\frac{1}{4}} P_{H_2}^{\frac{1}{4}}. \tag{3.4}$$

Assuming a constant mobility μ, the conductivity $\sigma = q\mu n$ will have the same dependency on the hydrogen partial pressure and temperature, and this was indeed found. Hence, by monitoring the change in electrical conductivity as the temperature and hydrogen pressure were varied, the authors were able to determine the solubility of hydrogen under various conditions, and found the activation energy for hydrogen diffusion to be 0.91 eV. More recently, Nickel [51] have performed H effusion experiments, concluding that the diffusion activation energy of H is not lower than 0.8 eV. Also, Johansen et al. [52] measured deuterium diffusion profiles with Secondary Ion Mass Spectroscopy (SIMS), finding a diffusion activation energy of 0.85 eV, in agreement with the previous findings. The diffusion was also found to be limited by H traps.

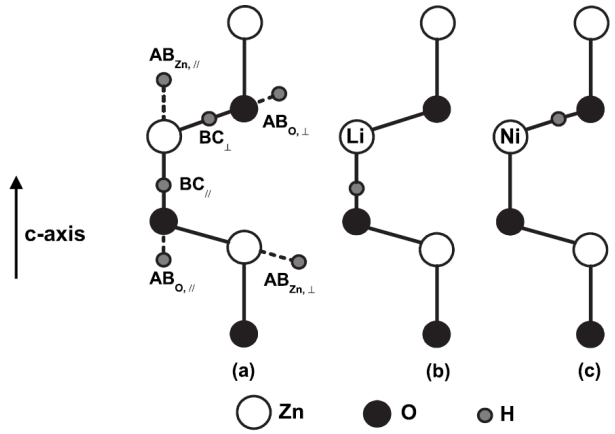

Figure 3.2: (a) Suggested positions for interstitial hydrogen in the ZnO crystal lattice. (b) and (c) Proposed configurations for the 3577 and 2783 cm^{-1} lines, respectively. From [47].

3.6.2 Electrical properties

Since the pioneering work of Thomas and Lander [7], it has been known that H incorporates as donor in ZnO, even in n-type material. In contrast, H is amphoteric in most other semiconductors, that is, the preferred charge state changes with the position of the Fermi level. Van de Walle [8] reproduced this behavior in DFT-calculations, showing that H act as a shallow donor in ZnO, and that H^+ always is energetically favorable at thermodynamic equilibrium. Several configurations for an interstitial H atom were considered, shown in figure 3.2, and it was found that the bond centered position $BC_\perp$ is the most stable position. Experiments on muonium implanted into ZnO [53] and electron-nuclear resonance measurements [54] later confirmed the role of H as a shallow donor. Hydrogen is invariably present during growth and is commonly regarded as a contributor to the prevailing n-type conductivity of ZnO [5].

Lavrov et al. [55] have performed a combined study of Raman scattering, IR absorption, photoluminescence (PL), and photoconductivity on ZnO, in which two shallow H donors were identified in hydrogenated VP samples. The dominant donor after hydrogenation was assigned to an unassociated OH_O ion, resulting in an IR absorption line at 3611 cm^{-1}. The involved H atom was found to reside in the $BC_\parallel$ interstitial position, contrary to the predictions of Van der Walle [8]. The ionization energy was determined from the temperature dependency of the free

carrier concentration to be 53 meV, and the decay of an exciton bound to O-H_{BC} results in a PL line at 3360.1 meV. O-H_{BC} was found to be unstable against annealing at 190 °C, suggesting that it is mobile also at room temperature.

The role of free H as a dominant donor in ZnO is not unproblematic, as H is both relatively mobile and has been shown to react with other defects and impurities. In ZnO crystals with a significant concentration (10^{17} cm^{-3}) of traps, H is therefore not expected to occur in the free, interstitial configuration [5]. Lattice vacancies and impurities have been shown to trap hydrogen, making complexes with higher thermal stability [52].

Such H complexes may also act as shallow donors [45]. Lavrov et al. [55] reported a second shallow H donor, which was assigned to a H atom associated with an oxygen vacancy, H_O. This defect was only observed after annealing in oxygen-poor ambients with subsequent or simultaneous incorporation of hydrogen. The donor has a ionization energy of 47 meV, and excitonic recombination of the H_O donor results in a photoluminescence (PL) line at 3.3628 meV, known as the I_4 line from previous reports [56]. PL measurements were also performed on a profiled sample to reveal that the H_O signal decreases exponentially as a function of depth, with a penetration depth of $\sim$ 2 μm after annealing in H_2 gas at 745 °C for 1 h, consistent with the known formation of oxygen vacancies near the sample surface. No IR absorption signature of this defect has observed, as the LVM frequency is expected to be approximately 760 cm^{-1} [57], where direct IR studies of ZnO are hardly possible [58]. The identification of H_O is therefore less established in comparison with O-H_{BC}. Theoretical investigations of H_O have been performed by Janotti and Van de Walle [57], who concluded that H_O is stable in n-type material, with an dissociation energy of $\sim$ 3.8 eV needed to break it up into V_O and H_i. The PL signal labeled I_4 was found to anneal out at around 500 °C, which is consistent with a dissociation energy of $\sim$ 3 eV [56].

Photoluminescence and temperature dependent Hall effect measurements performed by Look et al. [36] established the existence of a donor level 44 meV below the conduction band, with a donor concentration of 2-3·10^{16} cm^{-3}. A sharp emission line at 3362.70 meV in the photoluminescence spectrum were assigned to a recombination of an exciton bound to this donor, in good agreement with the findings of Lavrov et al. for the H_O defect. Based on thermal stability experiments and comparison with H diffusion and effusion experiments, the authors also assigned these PL and T-Hall fingerprints to a H donor level.

Many reports of the effects of H on ZnO may not be explained by pure donor

activity. As H is found in the positive charge state in both n-type and p-type material, it is particularly easily attracted to negatively charged acceptors, leading to the formation of neutral complexes. This neutralizing of acceptors by passivation is commonly the dominant electrical effect of H in ZnO, rather than contribution of electrons to the conduction band via shallow donor states [5].

Look et al. [59] have performed Hall effect and SIMS measurements on HT grown ZnO crystals annealed in 5 % H_2 in N_2, interpreting the results using a model involving two different conductive layers. Surprisingly, the authors found no evidence that H-related donors are active in the surface region. However, the H treatment strongly increased the bulk conductivity, which was attributed to the passivation of acceptors by H.

A similar conclusion was reached by Seager and Myers [60] who examined the effect of introducing hydrogen and/or deuterium on the electrical properties of ZnO. Hydrothermally grown samples with high resistivities were used in the study, and H (D) was introduced by in-diffusion from H_2 (D_2) atmospheres at 750 °C. Four-terminal conductivity and Hall-effect measurements were performed before and after the H_2/D_2 gas anneals. The electron densities in the as-grown samples were low and varying with crystal origin (10^{12}-10^{15} cm^{-3} at RT) and the Hall mobilities were 150-200 cm^2/Vs. From the magnitude and temperature dependency of the measured mobilities, the authors suggest that carriers are mainly scattered by charged impurities in the as-grown samples. After the H_2/D_2 gas anneals the carrier concentration increased to $1 - 2 \cdot 10^{17} cm^{-3}$ at RT for all samples. The Hall mobilities also increased, with a more pronounced temperature dependency, peaking at $\sim$ 800 cm^2/Vs. This behavior resembles what is expected when phonon scattering is the dominant scattering mechanism. From this, the authors concluded that the in-diffused hydrogen does not only increase the electron concentration by acting as a shallow donor, but also by passivating negatively charged impurities.

3.6.3 IR absorption studies of H-related defects

H in ZnO is normally assumed to be closely bound to an oxygen atom in the crystal, giving rise to O-H stretch vibrational modes [10]. IR-absorption spectroscopy is therefore a useful tool for studying these types of defects, as the frequency of the LVMs is dependent on the mass, bonding and local environment of the defect complex [45]. DFT calculations have also shown that the preferred interstitial position of H depends on the type of nearby impurities [61]. In the literature on the subject so far, IR spectra measured on hydrothermal (HT) samples are quite different

from the spectra from samples grown by the vapor-phase and melt growth methods. As described in section 3.4.1 HT growth introduces relatively large concentrations ($\sim 1 - 5 \cdot 10^{17}$) of Li and other impurities. IR absorption and electron paramagnetic resonance (EPR) studies indicate that hydrogen easily forms complexes with such substitutional impurities [47], and these impurity complexes seem to dominate the IR spectra of HT samples. To best of our knowledge, spectroscopic signatures of the unassociated O-H_{BC} configuration have not been reported in HT ZnO. In the following sections, the results obtained for the different growth techniques will therefore be described separately. A summary of the reported H-related defects in ZnO is given in tables 3.1- 3.3 on page 32.

Samples grown by the vapor phase (VP) method

In recent years, several groups have actively been studying hydrogen-related localized vibrational modes (LVMs) in ZnO by IR spectroscopy. In an "early" paper from 2002, McCluskey et al. reported an absorption line at 3326 cm^{-1} in VP samples annealed in H_2 gas at 700 °C. Based on comparison with the DFT calculations of Van der Walle [8], they ascribed this absorption line to hydrogen residing in an antibonding configuration, O-H_{AB}. The LVM at 3326 cm^{-1} was observed both with the light propagating parallel ($\vec{k} \| \vec{c}$) and perpendicular to the c-axis ($\vec{k} \perp \vec{c}$) with the ratio of the peak intensities indicating that the O-H bond has an angle of 119 ° as compared to the c-axis. The origin of the 3326 cm^{-1} LVM is not yet clarified. Both a single H bound to a zinc vacancy OH-V_{Zn} [62] and a OH-Ca_{Zn} complex [63] have been proposed as possible configurations.

Lavrov et al. [64] later did a more comprehensive work on the subject. VP samples were exposed to a remote hydrogen and/or deuterium dc plasma at 100-380 °C and measured with Fourier Transform IR spectroscopy at 9 K. No hydrogen-related peaks were observed in the samples before the hydrogen plasma treatment, but three absorption lines at 3611.3, 3349.6 and 3312.2 cm^{-1} emerged after hydrogenation, all showing deuterium replicas shifted to a lower wave number with the expected ratio of $\sim$ 1.37. Mixed hydrogen and deuterium treatment did not result in any splitting of the 3611-line, indicating that the absorbing defect contains a single O-H-bond. The absorption lines at 3312.2 and 3349.6 however showed a small splitting, indicating that they originate from the same defect, containing two, non-equivalent and weakly coupled hydrogen atoms. The thermal stability of these defects and the orientation of the involved O-H bonds were also investigated by Lavrov et al. [64], and the results are summarized in table 3.1. Based on these

findings, the authors proposes an unassociated O-H bond with hydrogen residing in a $BC_{||}$ configuration as the most probable model for the 3611 cm^{-1} line. This defect is the same as the unassociated H donor presented in section 3.6.2 above. A zinc vacancy decorated with two hydrogen atoms was proposed as a model for the 3312.2 and 3349.6 cm^{-1} lines. Later, isochronal annealing studies showed that the O-H_{BC} defect anneals out at $\sim$ 190 °C [55], while the $(OH)_2$-V_{Zn} defect is more stable, disappearing at $\sim$ 550 °C [46].

Jokela and McCluskey [65] have performed FTIR studies of ZnO crystals grown by chemical vapor transport with NH_3 added to the ambient gas. The dominant absorption line at 3150.6 cm^{-1} was assigned to a neutral N_O-H complex and found to be stable up to $\sim$ 700 °C. Substituting of D for H and ^{15}N for ^{14}N resulted in the expected frequency shifts, strongly supporting the identification of the complex. The difficulty of achieving p-type doping of ZnO using N_O acceptors is believed to be (at least partially) caused by passivation by hydrogen, resulting in the formation of neutral N-H complexes [9].

Hydrothermally grown samples

In contrast to vapor-phase ZnO, HT samples were shown to contain hydrogen in the as-grown state. Lavrov et al. [46] observed a strong absorption line at 3577.3 cm^{-1}, and three weaker lines at 3335.6, 3482.9 and 3516.3 in as-grown samples, all in the characteristic wave number range of O-H stretch modes. Deuterium plasma treatment did not result in deuterium replicas of the three weakest lines, so their nature is still unknown. They demonstrate distinct polarization properties, shown in table 3.1. The strong absorption line at 3577.3 cm^{-1} is invariably dominating the spectra of hydrothermal samples, and is the most studied H defect in these crystals.

Both deuterium plasma treatment [64] and in-diffusion from D_2 gas [11] have been shown to introduce a new absorption line at 2644.4 cm^{-1} in HT ZnO. This is in good agreement with the expected isotope shift of the 3577.3 cm^{-1} line. No additional splitting of the line was seen after exposure to a mixture of H and D, proving that a single O-H bond is responsible for the observed absorption. In a paper from 2005 [58], Lavrov et al. published further investigations of this defect. In this study, polarized light was used to determine the orientation of the involved O-H bond, finding that it is aligned along the c-axis. Also, the defect was found to exhibit remarkably high thermal stability, withstanding annealing at 1200 °C for several hours [58]. Isochronal annealing studies at 1200 °C were performed to investigate the stability of the defect, giving some puzzling results. The decay

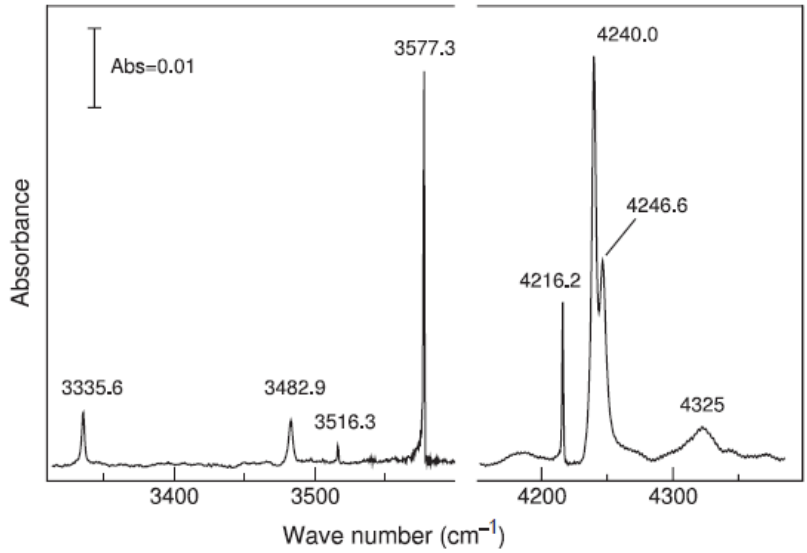

Figure 3.3: IR absorption spectrum of HT ZnO, by Lavrov et al. [64]. The spectrum was measured at 10 K using unpolarized light propagating in the $\vec{k} \perp \vec{c}$ direction.

rate of the 3577 cm^{-1} signal was shown to vary from experiment to experiment, seemingly depending on the annealing time step. The authors commented that this behavior indicate that the apparent stability of the defect is mainly determined by recapture and diffusion of hydrogen, and that dissociation of the absorbing defect may occur at lower temperatures. Even more surprisingly, after the 3577 cm^{-1} line disappeared, the lines at 3312.2 and 3349.6 cm^{-1} previously assigned to $(OH)_2$-V_{Zn} appear in the spectra. Subsequent hydrogen plasma treatment does not result in the regeneration of the 3577 cm^{-1} line, but slightly increases the $(OH)_2$-V_{Zn} signals. A proposed explanation of this behavior may be that the ZnO crystals decompose at the high temperatures employed in the study, resulting in the formation of native defects like V_{Zn}, which may trap hydrogen that is released from the defect responsible for the 3577 cm^{-1} line [58].

Halliburton et al. [6] have confirmed many of these findings. The authors also measured the peak position and the Full Width at Half Hight (FWHH) of the 3577 cm^{-1} peak as a function of measurement temperature, in the range from 9 K to room temperature. As expected from the theory of vibrational modes, a significant broadening and redshift towards lower wave numbers were observed. The authors tentatively assigned the defect to an O-H bond adjacent to a substitutional Li ion on a Zn site, based on the fact that lithium is introduced into the hydrothermal crystals during the growth. Also, the vibrational frequency of 3577 cm^{-1} is in reasonable

agreement with the value of 3556 cm^{-1} calculated for the OH-Li_{Zn} complex by first principle calculations [66]. Calculations performed in ref. [6] indicated that over 99% of the Li present in the sample reside in the OH-Li configuration, leading the authors to propose that one of the primary roles of hydrogen in ZnO is to provide passivation of singly ionized acceptors.

The involvement of Li was later confirmed experimentally by Shi et. al. [11], who showed that the O-D stretching counterpart of the 3577.3 cm^{-1} line is split into two components with intensities consistent with the natural abundances of the two isotopes of Li, (7.5% ^{6}Li and 92.5% ^{7}Li). Based on DFT calculations of the stability of different configurations of the defect, they presented a bond-centered structure as the most probable configuration (see figure 3.2 b). [11] This is also supported by the findings of Lee and Chang [67], who performed theoretical investigations on the stability of various OH-Li configurations.

OH-TM complexes

Transition metals (TMs) are interesting defects in ZnO, because of the possibility to make use of their magnetic properties in addition to the semiconducting properties of the host material. First principle calculations performed by Park and Chadi [68] indicated that hydrogen may be an important factor in achieving high temperature ferromagnetism in ZnO, and experimental results [69] indicate that hydrogenation of TM-doped ZnO may enhance the ferromagnetism in the material. The study of complexes between hydrogen and various transition metals may be an important factor in understanding the behavior of a possible ZnO-based dilute magnetic semiconductors.

Wardle et al. [45] have calculated the properties of various configurations of OH-TM complexes using density functional theory (DFT) under the local density approximation. The relative formation energies of the defects indicated strongly bound impurity-hydrogen complexes. The relevant LVM frequencies were also calculated and showed reasonable agreement with experimental observations.

Cu and H may form a variety of complexes, as shown by Gärtner and Mollwo [70] in the late seventies. The dominant absorption line at 3192 cm^{-1} was assigned as a OH-Cu_{Zn} complex, a result that recently was confirmed by Börrnert et al. [71]. The density functional calculations by Wardle et al. [45] suggested that OH-Cu_{Zn} may bind one more hydrogen atom, which results in the formation of a $(OH)_2$-Cu_{Zn} complex. Lavrov et al. [72] identified this complexes experimentally by IR absorption spectroscopy. Two LVMs at 3347 and 3374 cm^{-1} were observed after

in-diffusion of Cu at 1200 °C and hydrogen/deuterium from gas phase at 725 °C. Isotope substitution and uniaxial stress experiments showed that two equivalent O-H bonds in bond-centered positions are involved in the defect. The annealing dependency of the defect was found not to be monotonous. The IR absorption lines nearly disappeared after annealing at 390 °C, but regained their original intensity after annealing at higher temperatures. After annealing at 800 °C, the defect complex disappeared a second time. The authors presented a possible explanation for this unusual annealing dependency. In the same way as the OH-Li defect presented above, the thermal stability of $(OH)_2$-Cu_{Zn} is not determined by a traditional thermal decay, but is governed by a process involving dissociation, diffusion and recapture of a hydrogen species not visible in the IR spectra. Figure 3.4 shows the $(OH)_2$-Cu_{Zn} IR peaks as presented in the original article.

Substitutional Ni atoms have also been reported to form complexes with hydrogen in ZnO. Li et al. [47] reported an new LVM at 2782.9 cm^{-1} in nominally undoped hydrothermal samples hydrogenated in H_2 gas. Isotope substitution experiments and polarized IR absorption experiments revealed that the absorbing defect consists of a single O-H bond oriented at an angle of 108 ° to the c-axis. Isochronal annealing studies showed that the defect starts to dissociate at 500 °C, and completely disappears after annealing at 600 °C. The Ni_{Zn} absorption peaks at 4216, 4240 and 4247 cm^{-1}, described in section 3.5.3, were also observed, indicating that substitutional Ni impurities are present in the samples. Based on these results, comparisons with the first principles calculations by Wardle et al. [45] and electronegativity considerations, the absorption peak at 2782.9 cm^{-1} was assigned to a OH-Ni_{Zn} complex related to a bond-centered hydrogen. The reported peaks presented in the original article are shown in figure 3.5 and the proposed atomic arrangement is shown in figure 3.2 c.

This assignment was recently challenged by Lavrov and Weber [73] who have observed the 2783 cm^{-1} line in a HT sample annealed for several hours at 1190 °C, in which the LVM at 3577 cm^{-1} had disappeared. The appearance of the 2783 line did not occur at the expense of the Ni absorption lines around 4240 cm^{-1} which led the authors to doubt that Ni is involved in the absorbing defect. Instead, Lavrov et al. [73] suggested that the LVM at 2783 cm^{-1} originates from an impurity introduced during annealing.

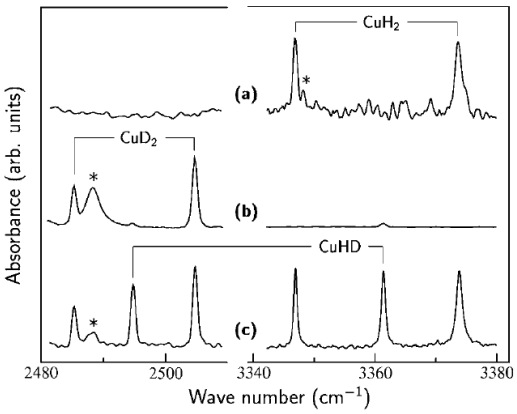

Figure 3.4: IR absorption spectra measured by Lavrov et al. [72] of HT grown ZnO after in-diffusion of Cu and subsequent annealing in (a) H_2, (b) D_2 and (c) H_2 + D_2. The measurement was done at 6 K, using unpolarized light propagating perpendicular to the c-axis. From [72].

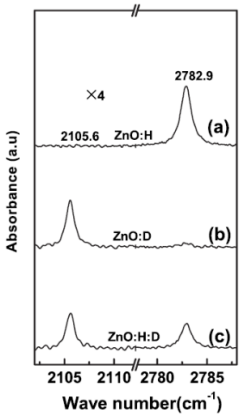

Figure 3.5: IR absorption spectra measured by Li et al. [47] of HT grown ZnO annealed in (a) H_2, (b) D_2 and (c) H_2 + D_2 at 725 °C. The measurement was done at 10 K using unpolarized light propagating perpendicular to the c-axis. From [47].

3.6.4 Hidden hydrogen

Shi et al. [74] have reported proof of so called "hidden hydrogen" in ZnO, that is, hydrogen species that can not be seen by IR absorption spectroscopy. In this study, vapor phase and melt grown samples were annealed in inert atmospheres and quenched to room temperature. For annealings at 400 °C, the O-H LVM at 3326 cm^{-1} appeared in the IR-spectra, showing that IR-inactive hydrogen must be present as a H source in the as-grown samples. Interstitial hydrogen molecules were proposed as the most probable candidate species. This prediction was later confirmed by the use of Raman spectroscopy by Lavrov et al. [75]. Hydrogen was introduced into VP samples by annealing in H_2 and/or D_2 atmospheres. The 3611 cm^{-1} LVM associated to the free O-H_{BC} defect was observed in the IR spectra of the hydrogenated samples. The signal was shown to be unstable under subsequent annealing, leading to the formation of electrically inactive H_2, HD and D_2 molecules in the Raman spectra.

The H_O defect, where H is associated with an oxygen vacancy, is another H species that is not detectable by IR absorption spectroscopy [55]. A substantial fraction of H in ZnO may therefore be located in this configuration for samples containing oxygen vacancies. Some of the reported results on the "IR-hidden" H_2 and H_O defects are reported in table 3.3.

Assignment	IR (O-H) (cm^{-1})	IR (O-D) (cm^{-1})	Configuration	Temperature stability	Ref.
N_O-H	3150.6	2339.7	N_O-H ($AB_{N,\perp}$)	700 °C	[65]
$(OH)_2$-V_{Zn}	3312.2	2460.7	O-H $\parallel \vec{c}$	550 °C	[64]
OH-V_{Zn}	3326.3	2470	O-H ($AB_{O,\perp}$)	150 °C	[62]
HO-Ca_{Zn}	"	"	"		[63]
$(OH)_2$-V_{Zn}	3349.6	2484.6	O-H $\perp \vec{c}$	550 °C	[64]
O-H_{BC}	3611.3	2668	O-H ($BC_{\parallel}$)	190 °C	[64, 55, 76]

Table 3.1: Summary of the hydrogen-related LVMs reported in VP ZnO. The notation for the configuration is defined in figure 3.2

Assignment	IR (O-H) (cm^{-1})	IR (O-D) (cm^{-1})	Configuration	Temperature stability	Ref.
OH-Ni_{Zn}	2782.9	2105.6	O-H ($BC_{\perp}$)	500 °C	[47]
OH-Cu_{Zn}	3191.8	2379	O-H ($BC_{\perp}$)	650 °C	[71, 70]
?	3335.6	-	Visible for $\vec{k}\|\|\vec{c}$ and $\vec{k}\perp\vec{c}$	-	[77, 58]
$(OH)_2$-Cu_{Zn}	3346.9	2485.3	O-H ($BC_{\perp}$)	350 °C	[72]
$(OH)_2$-Cu_{Zn}	3373.9	2504.7	O-H ($BC_{\perp}$)	350 °C	[72]
?	3482.2	-	O-H $\parallel \vec{c}$	-	[58]
?	3516.3	-	O-H $\parallel \vec{c}$	-	[77]
OH-Li_{Zn}	3577.3	2644.4	O-H ($BC_{\parallel}$)	1200 °C	[64, 6, 11]

Table 3.2: Summary of the hydrogen-related LVMs reported in HT ZnO. The notation for the configuration is defined in figure 3.2

Assignment	Raman LVM (cm^{-1})	PL signature (meV)	Temperature stability	Ref.
H_2 molecule	4145	-	-	[75]
H_O	-	3362.8 (I_4)	500 °C	[55]

Table 3.3: Reported results on Raman spectroscopy, photoluminescence (PL) and thermal stability on H species in ZnO not detectable by IR spectroscopy.

Chapter 4

Experimental techniques and procedure

In this chapter, the theory behind the characterization techniques relevant for this thesis is presented, with a particular focus on Fourier Transform Infrared Spectroscopy. The samples used in this study and details of the experimental procedure are then described.

4.1 Fourier transform infrared spectroscopy

Traditionally, grating spectrometers employing a monochromator have been used for IR transmission measurements. Today however, the Fourier Transform technique (FTIR) is almost invariably used [17]. To understand why this is so, it is useful to study the most important component of an FTIR spectrometer, the *interferometer*.

4.1.1 The Michelson interferometer

The Michelson interferometer was invented by the American physicist Albert Abraham Michelson in 1891, and has been an important instrument in the history of optics. For instance, it was the central part of the famous Michelson-Morley experiment, which was the first strong evidence against the conception of a luminiferous aether, and an important milestone in our modern understanding of light. A schematic illustration of the Michelson interferometer is depicted in figure 4.1. Many of the interferometers that are used today are still of this same design, or have other designs developed from it. Although the interferometer used in this

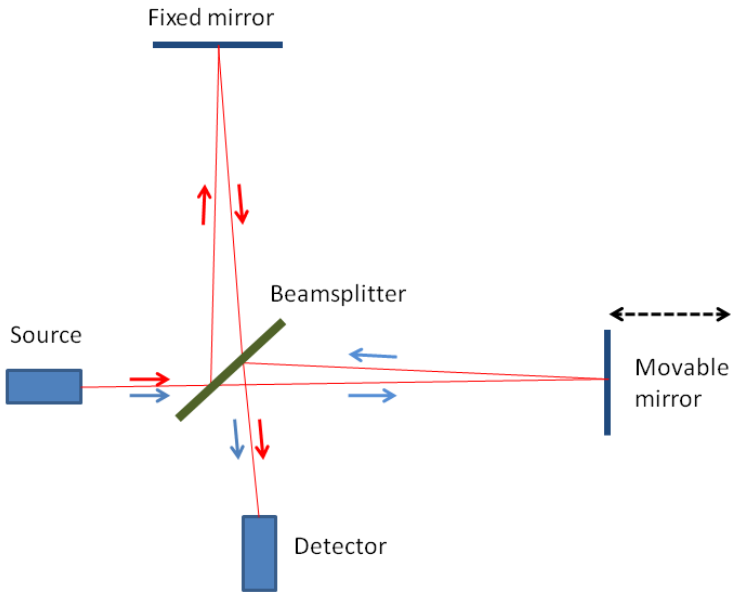

Figure 4.1: Schematic overview of the Michelson interferometer.

thesis is of another type than Michelsons original (a so-called Genzel type), the theory behind all scanning two-beam interferometers is essentially the same, and are more easily understood by examining the simplest case.

4.1.2 Theoretical background

A Michelson interferometer consists of two mutually perpendicular plane mirrors and a semitransparent mirror called a beam splitter. The setup is shown in figure 4.1. The beam from a light source is directed onto the beam splitter, which splits the beam into a reflected and a transmitted part. The reflected part is reflected again by a fixed mirror and returns to the beam splitter having passed a distance of $2L$. The transmitted part is passed onto a movable mirror, which can be moved a distance x from the position L. The transmitted beam thus passes a distance $2(L + x)$ before returning to the beam splitter. Parts of the transmitted beam is then reflected and parts of the reflected beam transmitted, so that the two beams recombine, with a path length difference of $\delta = 2x$. Since the two beams are spatially coherent, they interfere after the recombination. If we consider the simplest case of a monochromatic light source, the two beams will interfere constructively if the optical path difference δ is a multiple of the wavelength λ,

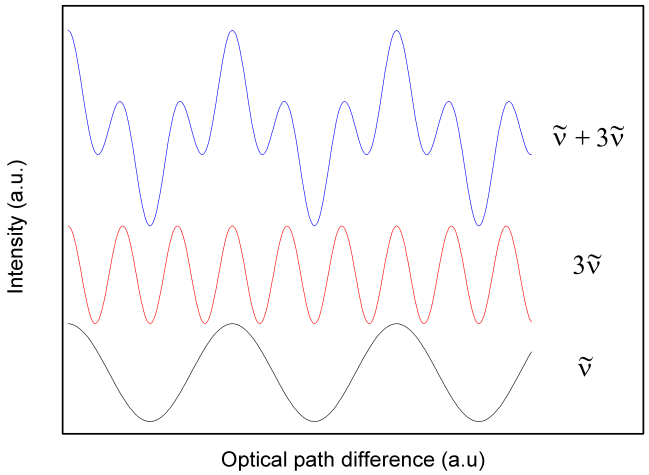

Figure 4.2: Illustration of the generation of an interferogram by superposition of cosine waves. Bottom: The interferogram from a monochromatic source with wavenumber $\tilde{\nu}$. Middle: The interferogram from a wavenumber $3\tilde{\nu}$. Top: The sum of the these two interferograms gives the interferogram for the polychromatic source.

$$\delta = m\lambda, \tag{4.1}$$

and destructively if δ is an odd multiple of $\lambda/2$

$$\delta = (2m+1)\frac{\lambda}{2}, \qquad m = 0, 1, 2, ... \tag{4.2}$$

The intensity I at the detector will therefore vary sinusoidally with the optical path difference (OPD) δ:

$$I^*(\delta) = \frac{I_0^*}{2} + \frac{I_0^*}{2} cos(\frac{2\pi\delta}{\lambda}). \tag{4.3}$$

As seen from eq. 4.3, the measured intensity consists of a constant and a modulated component. In infrared spectroscopy, it is common practice to omit the constant part, as this does not contain any information. The modulated component of the intensity as a function of OPD, is what is referred to as the *interferogram*. Substituting $\tilde{\nu} = \frac{1}{\lambda}$ we get:

$$I(\delta) = S_{\tilde{\nu}} cos(2\pi\tilde{\nu}\delta). \tag{4.4}$$

If the the source emits radiation with different wave numbers $\tilde{\nu}_1$, $\tilde{\nu}_2$, $\tilde{\nu}_3$, . . ., the interferogram will be a superposition of the cosines originating from each wavelength:

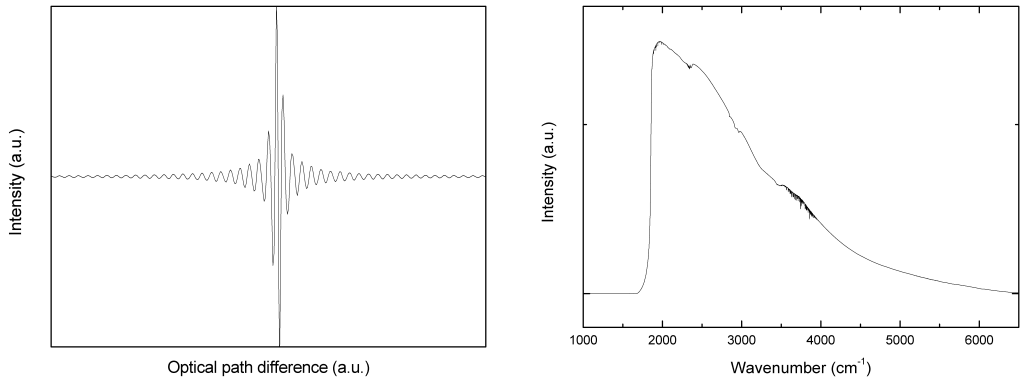

Figure 4.3: (a) Interferogram, (b) The resulting spectrum

$$I(\delta) = S_{\tilde{\nu}_1} cos(2\pi\tilde{\nu}_1\delta) + S_{\tilde{\nu}_2} cos(2\pi\tilde{\nu}_2\delta) + S_{\tilde{\nu}_3} cos(2\pi\tilde{\nu}_3\delta) + ... \tag{4.5}$$

Figure 4.2 shows this for the simple case of two waves with wave numbers $\tilde{\nu}$ and $3\tilde{\nu}$. The sources used for infrared spectroscopy normally operate by emission of thermal radiation from a heated black body, and thus have a continuous spectral distribution $S(\tilde{\nu})$. The interferogram then becomes an integral over all wave numbers $\tilde{\nu}$:

$$I(\delta) = \int_{-\infty}^{\infty} S(\tilde{\nu}) cos(2\pi\tilde{\nu}\delta)\, d\tilde{\nu}. \tag{4.6}$$

An example of an interferogram from a continuous source is shown in figure 4.3. Note the large intensity at zero OPD δ, where all wave numbers interfere constructively. This central peak is called the *center burst* of the interferogram. As the OPD increases, sinusoidal waves of different frequency interfere with each other, and give rise to a complex pattern of oscillations, symmetrically dispersed on each side of the center burst. The maximum intensity rapidly drops off as the mirror move away from the point of zero OPD, and these parts are therefore called the *wings* of the interferogram.

To obtain the recorded spectrum $S(\tilde{\nu})$ from the interferogram, one can recognize that eq. 4.6 is a cosine Fourier transform of $S(\tilde{\nu})$. The spectrum can therefore be retrieved by taking the inverse Fourier transform

$$S(\tilde{\nu}) = \int_{-\infty}^{\infty} I(\delta) cos(2\pi\tilde{\nu}\delta)\, d\delta. \tag{4.7}$$

Apodization

According to eq. 4.7, any spectrum can be measured perfectly by moving the mirror an infinitely long distance during the scan. This is of course not possible, and in practice the maximum optical path difference δ has a finite value Δ. The effect of restricting the maximum OPD is to multiply the interferogram by a so called boxcar function, given by:

$$A_{BC}(\delta) = \begin{cases} 1 & \text{for } -\Delta \leq \delta \leq \Delta \\ 0 & \text{otherwise} \end{cases} \tag{4.8}$$

The Fourier transform of the product of the two functions is given by a *convolution* of the Fourier transforms of the individual functions [14]:

$$S^*(\tilde{\nu}) = S(\tilde{\nu}) \otimes f_A(\tilde{\nu}). \tag{4.9}$$

The Fourier transform of the boxcar function $f_A(\tilde{\nu})$ has the shape of the *sinc* function $sin(x)/x$, illustrated in figure 4.4. As a result of this, the spectrum of a monochromatic source will not be a infinitely narrow line, but a broadened peak with several lobes of diminishing amplitudes on each side. The side lobes originating from one absorption line can be difficult to separate from other spectral features nearby, and they also make quantification of the spectral intensity more difficult. To suppress the amplitude of the side lobes, it is therefore common to multiply the interferogram by a trunctuation function $A(\delta)$ other than the boxcar function prior to the Fourier Transform. This process is called *apodization*. The price to pay for reducing the side lobes in this manner is broadening of the spectral lines, followed by a loss of resolution. Several apodization functions have been investigated over the years, and the functions used today give good side lobe suppression without sacrificing too much resolution. The apodization function used in this thesis is the so called *Blackman-Harris 3-term* function, given by

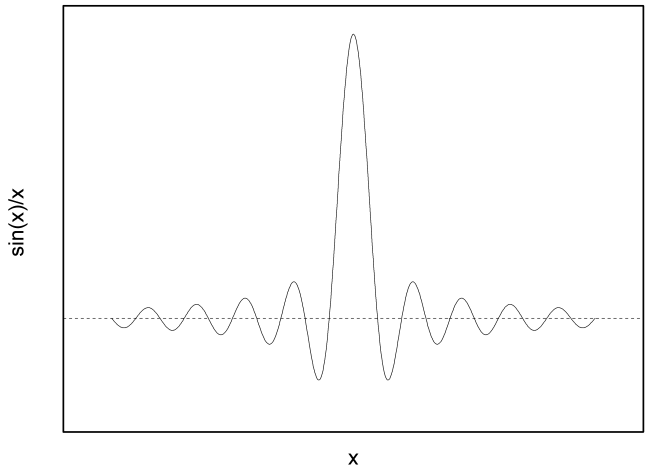

Figure 4.4: An illustration of the line shape of unapodized spectra, with side lobes surrounding the main peak.

$$A_{BH}(x) = \begin{cases} 0.42323cos(\pi\frac{x}{\Delta}) + 0.49755cos(2\pi\frac{x}{\Delta}) \\ +0.07922cos(3\pi\frac{x}{\Delta}) & \text{for } -\Delta \leq x \leq \Delta \\ \\ 0 & \text{otherwise} \end{cases} \tag{4.10}$$

The obtained resolution in a FTIR spectrum depends on the maximum OPD Δ and the apodization function that is applied. As a good rule of thumb, the resolution is given by the inverse of the maximum OPD

$$\Delta\tilde{\nu} \approx \frac{1}{\Delta}. \tag{4.11}$$

According to eq. 4.11, the spectrum can be measured at any desired resolution by increasing the maximum OPD Δ. In practice, this is only beneficial up to a certain point, because the noise level also increases linearly as Δ increases. Hence, the signal-to-noise ratio (SNR) of the spectrum is roughly proportional to the resolution [28]:

$$SNR \propto \Delta\tilde{\nu}. \tag{4.12}$$

As a trade-off between resolution and SNR, a resolution of $\Delta\tilde{\nu} = 1$ cm^{-1} was used for the measurements performed in this work.

Sampling the interferogram

When measuring the interferogram, the signal must be sampled at a discrete number of points. The *Nyquist criterion* states that a sinusoidal wave can be unambiguously sampled if the sampling frequency is at least twice the frequency of the wave [14]. Since the interferogram is a superposition of a large number of cosine waves, the analog signal from the detector can be sampled without any loss of information if the sampling frequency is at least twice the frequency of the highest wavenumber in the spectrum [14]:

$$f_{Nyquist} \geq 2f_{max} = 2\tilde{\nu}_{max}V_{opt}. \tag{4.13}$$

This is equivalent of sampling the interferogram every $(2\tilde{\nu}_{max})^{-1}$ cm. To ensure the highest possible SNR in the spectrum, it is common to average a large number of scans (see section 4.1.5). For the measured interferograms to be co-added correctly, it is important that the detector intensity is sampled at exactly the same points of the mirror position. This is accomplished by using a second interferometer sharing the same moving mirror as the interferometer measuring the spectra. The reference interferometer is equipped with a monochromatic light source, usually a HeNe-laser. The single-wavenumber interferogram in eq. 4.4 can then be used for very precise tracking of the moving mirror. At every second zero-crossing (once per wavelength) of the HeNe laser interferogram the analog-to-digital converter (ADC) is triggered to read out the IR interferogram. This setup is illustrated in figure 4.6. The wavenumber of the HeNe laser is $\tilde{\nu}_{HeNe} = 15800$ cm^{-1}, so the Nyquist frequency $\tilde{\nu}_{max}$ becomes 7900 cm^{-1}. If higher frequencies are to be measured, the interferogram can also be digitized at every zero-crossing, giving a Nyquist frequency of 15800 cm^{-1}.

To obtain correct signal averaging by co-adding spectra, it is also important that each measurement scan is started at exactly the same position of the moving mirror. In older FTIR instruments like the IFS 133v, this is accomplished by measuring the interferogram of a broadband, white light source together with the sinusoidal laser interference. This gives a sharp interference peak which is used to trigger the start of the measurement of each mirror scan. The process is illustrated in figure 4.5 [14].

4.1.3 Strengths and limitations of FTIR spectroscopy

Fourier Transform spectrometers have several advantages compared to the traditional, dispersive spectrometers which are based on a monochromator. One of the

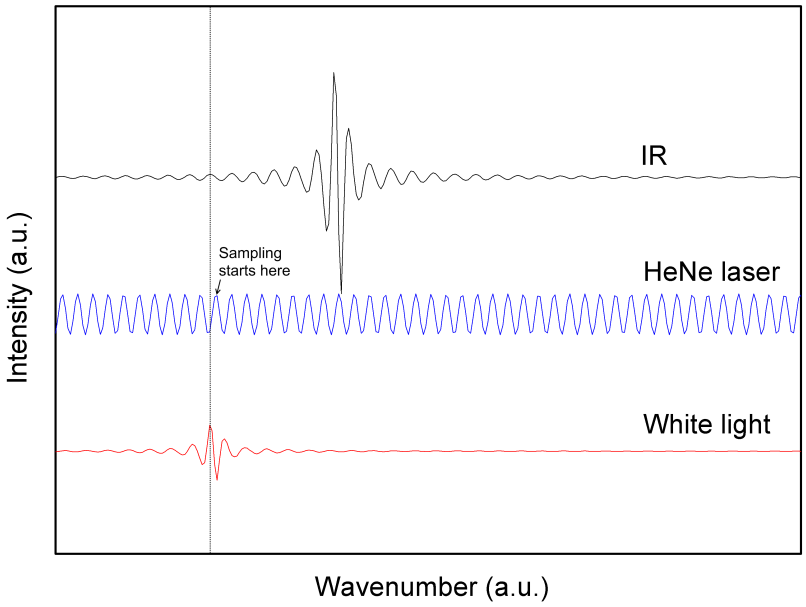

Figure 4.5: Illustration showing the three interferograms used in the sampling system.

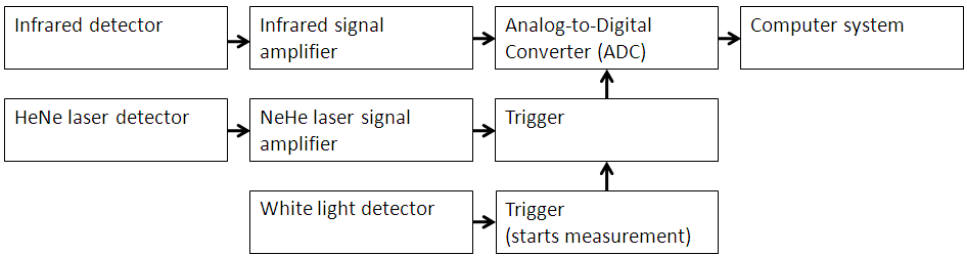

Figure 4.6: Schematic flowchart showing the signal processing in an FTIR instrument

most important benefits is the possibility to measure the whole spectrum with a single scan of the mirror. This is called the multiplex (or Fellgett) advantage. The optical velocity V_{opt} of the scanner in modern FTIRs can be quite high ($\sim 1-3$ cm/s), so complete spectra can be measured within fractions of a second. Together with the possibility to perform signal averaging of subsequent measurements to reduce random noise, this gives a substantial increase in the signal-to-noise ratio (SNR) of FTIRs compared to dispersive spectrometers. More precisely, for a given measurement time, optical throughoutput and resolution, the SNR is $\sqrt{N}$ times better for a spectrum measured on a FTIR spectrometer, where N is the number of resolution elements [14].

A dispersive spectrometer also requires the use of a narrow slit which reduces the optical throughoutput of the instrument. In a FTIR, the throughoutput is only limited by the effective area of the mirrors, thus giving a higher signal and a better SNR. This advantage is known as the Jacquinot advantage.

Lastly, the so-called Connes advantage rises from the fact that all modern FTIR instruments have a very precise internal system for wavenumber calibration, as described in section 4.1.2. This gives a error in $\Delta\tilde{\nu}$ solely determined by the error of the reference laser wavelength ($0.01cm^{-1}$).

These factors, together with the high mechanical stability and relatively low cost of modern FTIR instruments, have resulted in that almost all infrared spectrometers used today are of the FTIR type [14].

Despite the many advantages, the FTIR technique have limitations that applies to IR spectroscopy in general. As described in section 2.2.2, only chemical bonds with a time-varying dipole moment may be detected. For measurements performed in the transmission mode the sample must be sufficiently transparent in the IR spectral region. Accurate determination of the concentrations of absorbers is only possible if the relevant conversion factor ϵ is known. Also, FTIR is a *single beam* technique, meaning that background spectra must be recorded at a different time than the sample spectra, which may result in atmospheric absorption disturbing the spectrum. More specific for this work, the detection limit for H in single crystal oxide samples is estimated to be 10^{14}-10^{15} cm^{-3}, based on the typical noise level of the spectrometer and previously reported values for the aborption cross section for O-H bonds ϵ_{OH} (see table 5.6).

4.1.4 Spectral manipulation

Interference fringes

When a sample of thickness d is placed in the beam, light can be reflected from both its front and back surface. A portion of the light may therefore be internally reflected twice inside the sample before hitting the detector, interfering with the light that is directly transmitted. A constructive interference will be seen for

$$m\lambda = 2dn \Leftrightarrow \tilde{\nu} = \frac{m}{2dn}, \tag{4.14}$$

where m is an integer and n is the refractive index of the sample. As a result of this, a sinusoidal noise will bee observed over the hole spectrum.

To correct for such unwanted interference effects, it is common to manipulate the interferogram before taking the Fourier Transform. Since the Fourier Transform of a narrow peak is a sinusoidal wave (see eq. 4.4), the sinusoidal interference fringes will appear as an extra peak in the interferogram. For the samples used in this thesis, this interference peak lies in an area with little amplitude of the interferogram. The peak may therefore simply be replaced with a straight line, without significantly altering the real spectrum. An illustration of how this kind of manipulation affects the absorbance spectra is shown in figure 4.7.

Interference fringes can also be useful. By using eq. 4.14 it is possible to calculate the thickness d of the sample. If there are m interference fringes between two wave numbers $\tilde{\nu}_1$ and $\tilde{\nu}_2$, the thickness of the sample can be calculated as

$$d = \frac{m}{2n(\tilde{\nu}_2 - \tilde{\nu}_1)}. \tag{4.15}$$

Glitches

Electrical, optical or mechanical oscillations may also occasionally contribute to the measurement, giving a sinusoidal interference of frequency f in the interferogram. Such an oscillation will be manifested as a sharp peak at the wavenumber f/V in the spectrum, where V is the optical velocity of the interferometer in cm/s. In addition, glitches arising from various overtones may be seen at the wave numbers $2f/V$, $3f/V$ and so on. This type of nonrandom noise are called *glitches* and are commonly seen in FTIR spectra. Glitches can both be identified and shifted away from important regions of the spectrum by changing the optical velocity V [14].

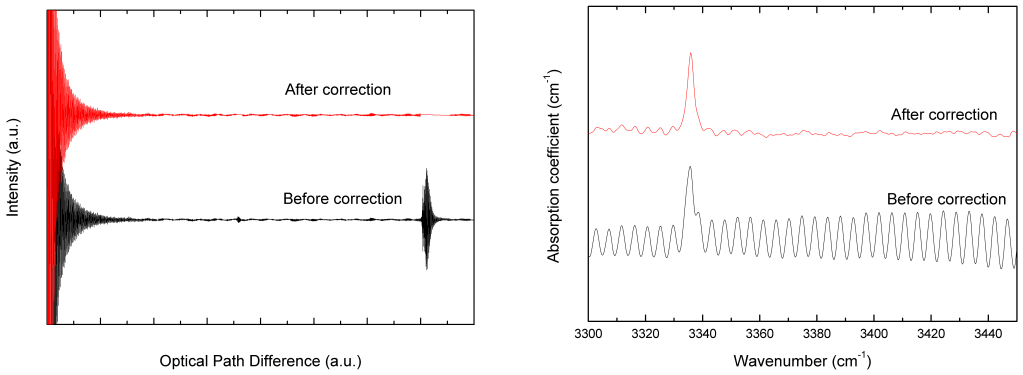

Figure 4.7: (a) Correction of a bad case of interference fringes by inserting a straight line in the interferogram (b) The resulting effect on the spectrum

Baseline correction

Due to reflection from the sample surfaces and broad absorption features in the sample, e.g. from free carrier absorption, the transmitted intensity is usually lower than the background intensity over the hole spectrum. Because of this, the baseline in the absorbance spectrum is almost always shifted somewhat upwards from the zero absorbance level, and it usually has some slope or curvature (see eq. 2.23). To facilitate the presentation and interpretation of the spectra, it is therefore common to perform a baseline correction. This can be done by fitting a straight line or a polynomial to data, or by manually defining a number of baseline points connected with straight lines.

4.1.5 The FTIR instrument in MiNaLab

A Bruker IFS 113v infrared spectrometer was used for the measurements presented this work. This is a so called Genzel type interferometer, and is designed for measurements in the far- and mid-infrared region. An overview of the optical beam path inside the instrument are shown in figure 4.10. After the beam has been split by the beam splitter, the two different parts are passed onto a double-sided, moving mirror and then recombined. For a mirror displacement x, the optical path length difference is therefore $4x$, so that the optical velocity is four times the mirror velocity. The performance and optical configuration of the spectrometer is given in table 4.1. For a more complete description and a guide for practical operation, see the user instructions, available from the author on request.

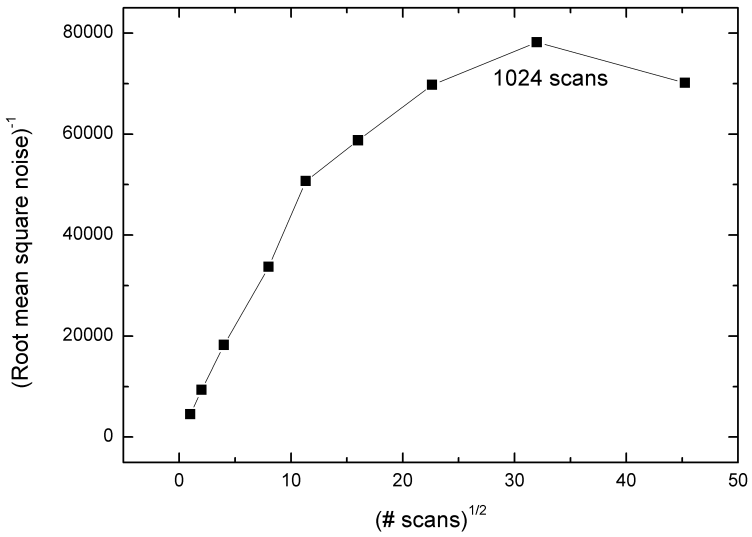

Figure 4.8: The inverse of the root mean square noise versus the number of scans that has been averaged.

Signal statistics

100%-lines are used to indicate how the noise varies across the spectrum, and are obtained by calculating the absorbance given by two background spectra taken under identical conditions. To determine how the noise level varies with the number of scans N, 100%-lines were measured for 1, 4, 16, 64, 128, 256, 512, 1024 and 2048 scans. As most of the hydrogen LVM's are ecpected between 3200 and 3600 cm^{-1}, the noise in this region is particularly interesting, and these data points were therefore used in the calculations. The noise is taken to be the root-mean-square (rms) of all the data points in this region. As the signal-to-noise ratio (SNR) is proportional to the inverse of the rms noise, this gives a good indication of the number of scans for optimum SNR. Ideally, the SNR should vary as the square root of the number of scans [28]. This is however only true up to a certain point, where instrument drift can cause nonrandom errors that do not average out. From figure 4.8 it can be seen that the SNR rises linearly with $\sqrt{N}$ for low numbers of scans, before the curve start to flatten out. The best SNR is obtained when averaging 1024 scans. This number of scans was therefore used for all the following measurements.

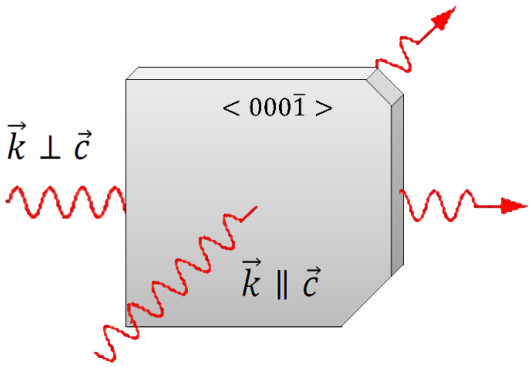

Figure 4.9: Illustration of a typical ZnO wafer, indicating the two possible different geometries for the IR transmission measurements.

Instrumental configuration

The infrared absorption spectra were recorded with a Bruker IFS 113v Fourier transform spectrometer. Table 4.1 describes some selected instrument specifications, as described in the instrument manual. Spectra were measured using unpolarized light propagating through the sample in two non-equivalent crystallographic directions, perpendicular ($\vec{k} \perp \vec{c}$) and parallel ($\vec{k} \| \vec{c}$) to the c-axis, as illustrated in figure 4.9. Data collection and manipulation were done using version 3.0.16 of the OPUS software.

The samples were mounted inside a Closed Helium CTI-Cryogenics Helix 22 Compressor 8200 cryostat, and the temperature was recorded with a LakeShore Cryotronics DRC 82C temperature controller.

Sources of error

There are several factors that may affect the positions and intensities of the IR peaks. Firstly, there is currently no functional system for accurately controlling the sample temperature. A random variation in sample temperature between 16 and 24 K was measured, giving rise to small shifts up to $\sim$ 0.3 cm^{-1} in the peak positions and widths. The integrated intensity of the peaks arising from O-H stretch modes does however not change as a result of this variation [14].

There is also a potential error (estimated to be $1 - 5\%$) in the measured sample thickness, which is used to calculate the absorption coefficient α in eq. 2.24. Relative changes measured on the same sample will however not be affected by this uncertainty.

Light that reaches the detector without having passed through the sample reduces the apparent absorption intensity, and may thus also be a potential source of error. Great care was therefore taken to seal any stray light.

In addition, random noise in the spectra caused by background IR radiation, mechanical instabilities in the spectrometer and other factors limit the accuracy of the measured peak intensities. The signal-to-noise ratio (SNR), calculated from the maximum peak intensity and the rms noise level, was found to vary between 10 and 250, depending on the measurement conditions. The integrated intensity of all the absorption peaks are given in appendix A.1, and the relevant SNR is reflected by the given number of significant figures.

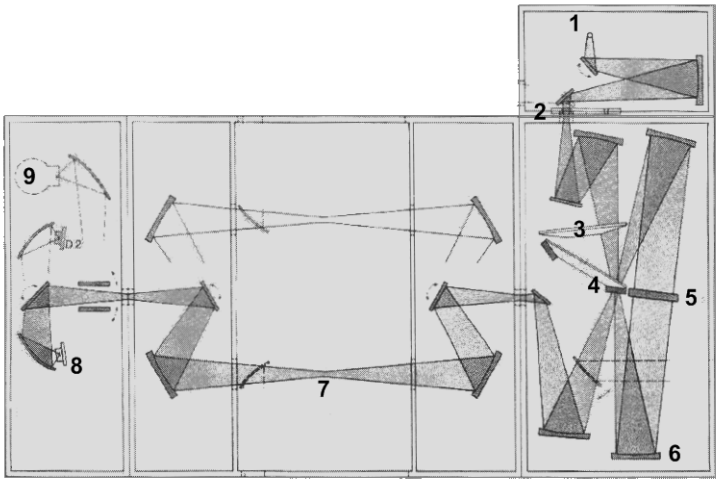

Figure 4.10: Overview of the beam path in the Bruker IFS 113v FTIR spectrometer, edited from the instrument manual. 1) Globar source, 2) Aperture, 3) Filter exchanger (not used), 4) Beam splitter, 5) Double-sided movable mirror, 6) Stationary mirrors, 7) Sample position, 8) DTGS detector (not used), 9) InSb detector.

	Given instrument specifications	Setup used in this work	
	Overall performance		
Resolution	0.1 cm^{-1}	1 cm^{-1}	
Accuracy	0.01 cm^{-1}	*	
Optical velocity	0.23 - 3.14 cm/s	0.94 cm/s	
	Optical components		Spectral range
IR-source	SiC Globar	SiC Globar	100 - 6000 cm^{-1}
Beam splitters	Si on CaF_2 substrate	Si on CaF_2 substrate	1250 -15000 cm^{-1}
	Ge on KBr substrate		400 - 5200 cm^{-1}
Detectors	LN_2-cooled InSb (Photovoltaic)	LN_2-cooled InSb (Photovoltaic)	1850 - 10000 cm^{-1}
	LN_2-cooled HgCdTe (Photovoltaic)		625 - 5000 cm^{-1}
	DTGS (Pyroelectric bolometer)		350 - 7000 cm^{-1}

Table 4.1: Instrumental configuration of the FTIR instrument in MiNaLab. Values are obtained from the instrument manual or from ref. [78].

4.2 Four point probe measurements

The resistivity of the samples were measured with a four point probe setup, shown schematically in figure 4.11. The setup consists of four co-linear, equidistant probes. Current is passed between the two outer probes and the voltage is measured across the two inner ones. The probe tips were dipped in eutectic InGa to improve contact to the sample. The sample resistivity is then calculated as

$$\rho = 2\pi KP\frac{V}{I}, \tag{4.16}$$

where K is a geometrical correction factor dependent on the thickness of the sample and P is the probe spacing. To obtain a higher statistical accuracy, the resistivity was calculated from the average of several values obtained by applying different currents. If the carrier mobility (μ) of the sample is known, the carrier density n may be calculated from the resistivity using the relation

$$\frac{1}{\rho} = q\mu n, \tag{4.17}$$

where q is the elementary charge, q = $1.602 \cdot 10^{-19}$ C.

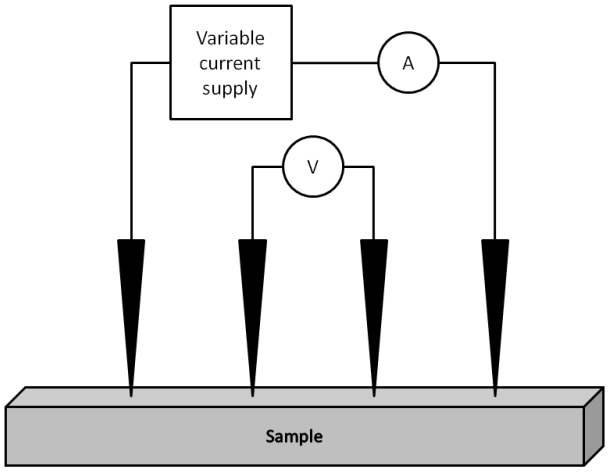

Figure 4.11: Schematic illustration of the setup used for resistivity measurements

4.3 Secondary Ion Mass Spectrometry

Secondary Ion Mass Spectrometry (SIMS) is a technique for analysis of impurities present in bulk and thin film samples with a thickness up to a few tens of microns. A beam of energetic primary ions is focused onto the sample surface, leading to a sputtering process where neutral or charged atoms and molecules are ejected from the target. The sputtered particles that are ionized can then be accelerated by an electric field, creating what is called the secondary ion beam. This beam is analyzed in a mass spectrometer to determine the impurity content of the sample. The beam is first passed through a electrostatic sector analyzer, where it is bent by a constant electric field and passed through a narrow slit. This filters out the ions of a specific kinetic energy, which are then passed onto a magnetic sector analyzer. Here, the ions are deflected by a constant magnetic field and passed through another slit, filtering them by momentum. A schematic illustration of the setup is shown in figure 4.12. By varying the strength of the magnetic field, particles with a given momentum can be studied, or a spectrum may be recorded. The technique however has one fundamental disadvantage: Since the sputtered particles are accelerated by a constant voltage, ions of higher charge are accelerated to higher velocities, making them inseparable from heavier particles with lower charge. Combining the energy filter (electrostatic analyzer) and the momentum filter (magnetic analyzer), the spectrum is therefore obtained as a function of the mass-to-charge ratio, given by [79]

$$\frac{m}{q} = \frac{B^2 r_m}{E r_e}, \tag{4.18}$$

where B, E, r_m and r_e are defined in figure 4.12.

The SIMS technique can be used in three different modes of operation. Perhaps the most common one is depth profiling, where the beam is rastered over a square, making a crater at the sample surface. The number of counts of a given mass-to-charge ratio is measured as a function of time, which can then be translated to the concentration as a function of depth. By rastering the beam over an area of the sample SIMS can also be used for imaging, giving the concentration of one or more elements as a function of lateral coordinates. Also, by scanning the magnetic field in the magnetic sector analyzer it is possible to record the entire mass-to-charge spectrum, in principle determining the complete impurity content of a sample.

The primary ion beam in a SIMS instrument usually consists of Cs^+ or O_2^+ ions. A source of Cs^+-ions is normally used to promote sputtering of electronegative

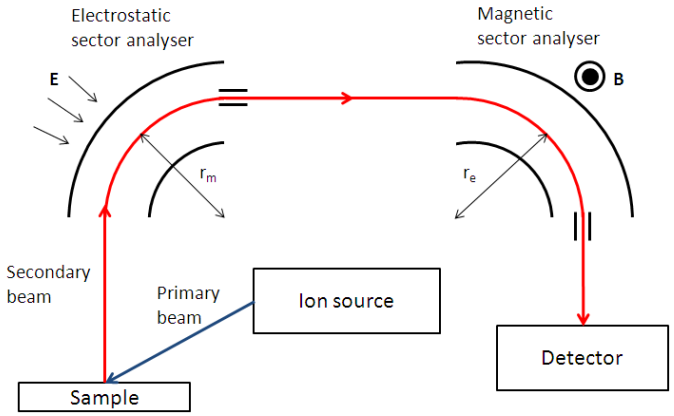

Figure 4.12: Basic principles of the SIMS technique

elements, while O_2^+ ions are used to sputter electropositive elements. The *ionization yield* of an element measured with SIMS vary widely depending on many different factors, making quantitative analysis difficult without the use of calibration standards. Usually a known dose of the element to be studied is ion-implanted into a pure sample and the implantation profile is measured with SIMS and integrated to produce a calibration factor. With good calibration, a SIMS is capable of detecting a range of concentrations that covers up to five orders of magnitude, and is sensitive down to concentrations of $\sim 10^{13} - 10^{17}$ cm^{-3}, depending on the element. With a depth resolution down to $\sim$ 2 nm and a lateral resolution down to $\sim$ 500 nm in several commercial instruments (like Cameca IMS), SIMS gives a combination of resolution and sensitivity that no other technique achieves today [79].

4.3.1 Instrumental configuration

The SIMS mass spectra and chemical concentration versus depth profiles presented in this work were measured in a Cameca IMS7f microanalyzer. The primary beam was rastered over a surface area of 150×150 μm^2 and secondary ions were collected from the central part of the sputtered crater. Mass spectra were recorded using both 10 keV O_2^+ and 15 keV Cs^+ ions as the primary beam, while Ni and Li depth profiles were recorded using 10 keV O_2^+ ions only. Crater depths were subsequently measured with a Dektak 8 stylus profilometer, and a constant erosion rate was assumed for depth calibration. The concentration calibration was performed using an as-implanted sample as reference.

4.4 Experimental procedure

4.4.1 Samples and work flow

In this work, as-received ZnO wafers commercially available from SPC Goodwill were used as starting material. The wafers are grown by the hydrothermal (HT) method, with a reported purity of > 99.99%, and are cut perpendicular to the c-axis, to a size of $10 \times 10 \times 0.5$ mm^3 [80]. Two ZnO wafers labeled "A" and "B" were used as the main subject of this study. The as-recieved resistivities of the wafers were measured with four point probe measurements to be $\rho = 5400$ ohm cm and $\rho = 420$ ohm cm for wafers A and B, respectively. The wafers were cut into samples labeled "A-1", "A-2", "B-1" and "B-2". In addition, two samples cut from other wafers, labeled "C" and "D", have been used for complementary measurements. Figure 4.13 gives a survey of all the sample treatment and characterization steps that have been performed in this work.

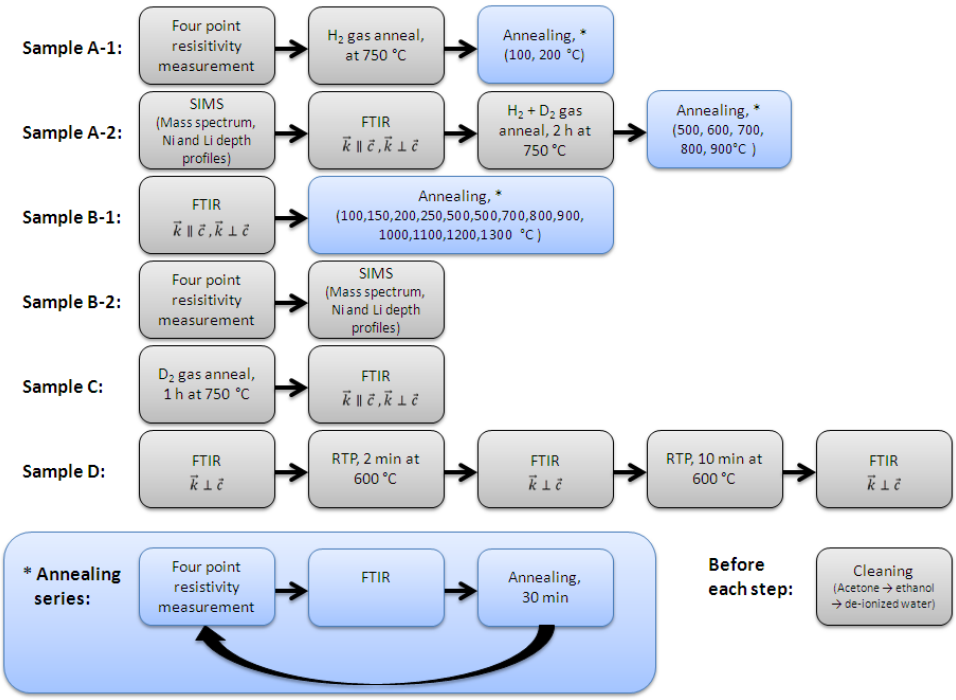

Figure 4.13: Overview of the experimental procedure used in this work.

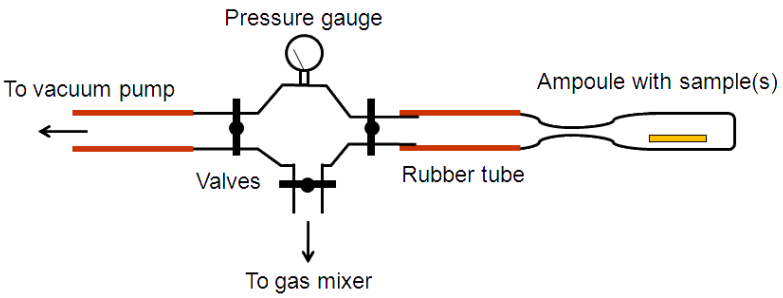

Figure 4.14: A schematic drawing of the setup used to fill the ampoules with controlled gas atmospheres.

4.4.2 Introduction of H and D from gas phase

To introduce hydrogen/deuterium into the ZnO crystals, samples were sealed in quartz ampoules filled with 1/2 atm of H_2 and/or D_2 gas at room temperature. In the mixed gas atmosphere equal partial pressures of H_2 and D_2 gas within 10 % were obtained by controlling the gas flow. The setup used for filling of the ampoules is shown in figure 4.14. The H_2/D_2 gas was passed through a humidifier and saturated with $\sim$ 2.5% H_2O/D_2O vapour before being filled into the ampoules, in order to reduce the degradation of the samples by the reduction reaction:

$$ZnO_{(s)} + H_{2(g)} \rightleftharpoons Zn_{(g)} + H_2O_{(g)}. \tag{4.19}$$

Both the hydrogen solubility in ZnO and the sample degradation have previously been found to increase with H_2 pressure and temperature [7, 81]. Based on previous hydrogen in-diffusion experiments [47, 73], an annealing temperature of 750 °C was used, as a compromise between the two. The ideal gas law gives a relation between the pressure p, the absolute temperature T, volume V and number of molecules N in a gas as [82]

$$pV = Nk_BT, \tag{4.20}$$

where k_B is Boltzmann's constant. When the temperature inside the ampoules increases while N and V are held constant, the pressure p also needs to increase:

$$\frac{N}{V} = \frac{p_1}{k_BT_1} = \frac{p_2}{k_BT_2}. \tag{4.21}$$

By solving for p_2 and inserting $p_1 = 1/2$ atm, $T_1 = 300$ K and $T_2 = 1023$ K, the pressure at 750 °C can be found to be $p_2 \approx 1.25$ atm. According to the experiments

and calculations of Thomas and Lander [7], the hydrogen solubility in ZnO at this pressure and temperature is approximately $5 \cdot 10^{17}$ cm^{-3}.

To obtain a uniform H concentration throughout the sample it was necessary to determine the minimum H_2 annealing time. As a guide line, a theoretical diffusion profile was calculated from the reported H diffusion coefficients of Thomas and Lander [7] and Johansen et al. [52]. Fick's second law describes the concentration of a randomly diffusing species c as a function of position x and time t [12]. In one dimension it is given by the differential equation

$$\frac{dc}{dt} = D\frac{d^2c}{dx^2}, \tag{4.22}$$

where D is the diffusion coefficient. The solution of this equation for doubled-sided diffusion into a plane sheet with constant and equal surface concentrations can be found in diffusion reference books [83]:

$$\frac{C - C_0}{C_s - C_0} = 1 - \frac{4}{\pi}\sum_{n=0}^{\infty}\frac{(-1)^n}{2n+1}exp\{\frac{-D(2n+1)^2\pi^2 t}{4l^2}\}. \tag{4.23}$$

Here, C is the concentration in the middle of the sample after t seconds, C_0 is the initial concentration, C_s is the surface concentration, taken as the H solubility, and l is the sample thickness. Figure 4.15 shows the solution for C(t) for the two previously reported diffusion coefficients [7, 52].

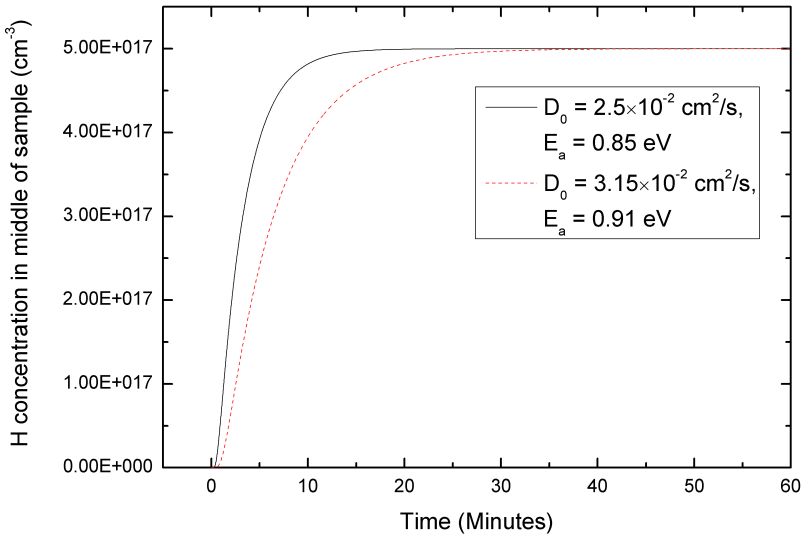

Figure 4.15: H concentration in the center of the sample as a function of hydrogenation time at 750 °C. Calculated from eq. 4.23 and diffusion data from [52] and [7]

Sample	Atmosphere (RT)	Annealing
A-1[a]	1/2 atm H_2 + H_2O	600 °C, 1h
		+700 °C, 4 h
		+750 °C, 1 h
A-2	1/2 atm (H_2+D_2) + H_2O	750 °C, 2 h
C	1/2 atm D_2 + D_2O	700 °C, 1 h

[a] Sample A-1 was passed through several subsequent annealing steps to investigate the reduction of the sample by the H_2 gas.

Table 4.2: Experimental conditions used for the different gas anneals.

As seen from figure 4.15, a uniform H concentration should be reached after 15-45 min, depending on the diffusion coefficient. Previously, Johansen et al. [52] have concluded that H diffusion is trap limited between 100 and 400 °C, reducing the H diffusion length from what is expected according to the model. However, the effect of traps will probably be less pronounced at higher temperatures due to a high dissociation rate [52]. The gas annealing conditions for the three samples are shown in figure 4.2. Based on the above discussion, it is reasonable to assume that equilibrium conditions were reached, or at least that H diffuses into the whole bulk of the samples. If a non-uniform concentration was obtained after hydrogenation, the calculations performed in the next chapter will relate to the average H concentration in the samples.

After the annealing, the ampoules were quenched in cold water in order to freeze in the H concentration and the sample surfaces were polished using a suspension of 3 μm diamond particles.

Chapter 5

Results and discussion

This chapter presents the results of the experimental procedure outlined in section 4.4. To minimize confusion, various aspects of the results are presented and discussed in separate sections. For a full overview of all the infrared absorption measurements and intensities of the various peaks, see appendix A.1.

5.1 IR spectra measured on as-grown samples

Figures 5.1 and 5.2 show the IR spectra of the as-grown state of samples A-2 and B-1, respectively. Several absorption lines are seen in the wave number region from 3300 to 3600 cm^{-1}, characteristic of OH stretch modes. In both samples the dominating line is found at 3577 cm^{-1}, with weaker lines observed at 3279, 3336, 3483 and 3516 cm^{-1}. The intensity of the 3577 cm^{-1} peak is comparable in the two samples, while the other lines are more pronounced in sample B-1. As shown in figure 5.2 the intensity of the 3336 cm^{-1} line measured in the $\vec{k}||\vec{c}$ orientation is comparable to that of the 3577 cm^{-1} line for sample B-1. In addition, several other, weaker features are seen in the spectrum for sample B-1. However, they will not be discussed any further in this thesis. In addition, absorption lines are also found at 4216, 4240 and 4246 cm^{-1} in both samples, with the integrated intensity being approximately one order of magnitude higher in sample A-2 than in sample B-1. The integrated intensity of the main absorption lines are summarized in tables 5.1 and 5.3.

5.1.1 Defect identification

The localized vibrational mode (LVM) at 3577 cm^{-1} has previously been found to be the dominating absorption line in hydrothermal (HT) ZnO and is almost

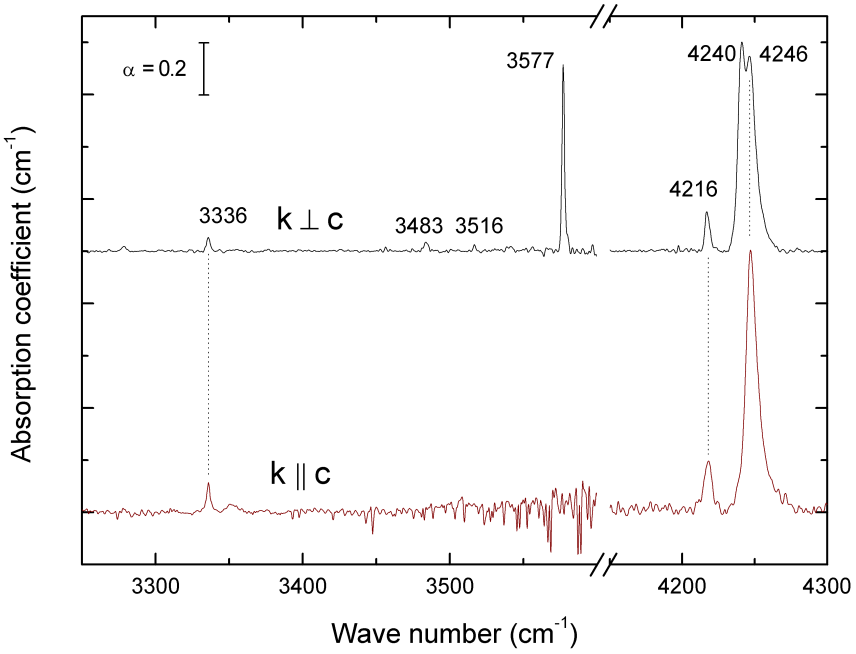

Figure 5.1: IR absorption spectra of sample A-2 in the as-grown state, measured in the $\vec{k} \perp \vec{c}$ (top) and $\vec{k} \| \vec{c}$ (bottom) orientations.

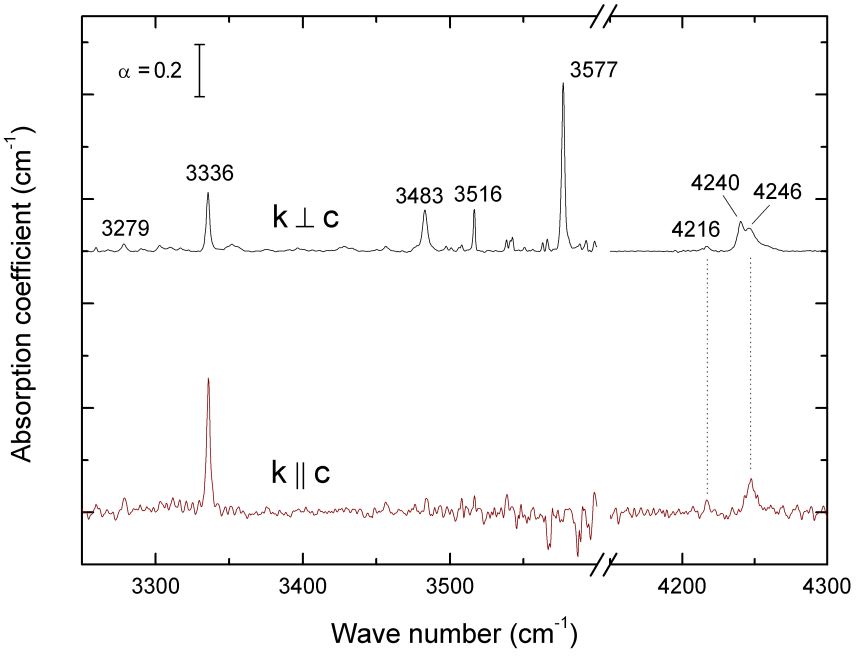

Figure 5.2: IR absorption spectra of sample B-1 in the as-grown state, measured in the $\vec{k} \perp \vec{c}$ (top) and $\vec{k} \| \vec{c}$ (bottom) orientations.

invariably observed in the IR spectra of HT ZnO samples. The line has previously been assigned to a defect complex involving a single O-H bond perturbed by a neighboring Li substituting on a Zn site [6, 11] (see section 3.6.3 for details). Measured isotope shifts of both Li and H [11] give strong evidence for this assignment. The exact defect configuration is however not clear, and it is possible that additional native defects or impurities are involved in the absorbing defect complex. In section 5.5.1 some results on the thermal stability of the complex are discussed and in section 5.5.2 the 3577 cm^{-1} peak intensity is related to the concentration of OH-Li complexes in the samples.

The absorption lines at 3336, 3483 and 3516 cm^{-1} have previously been observed by Lavrov et.al. [58] in as-grown HT ZnO. To our knowledge, no deuterium replicas of these lines have been reported, so no direct evidence exist that the absorbing defects involve O-H stretch modes. However, the fact that H is present in as-grown ZnO and that the absorption takes place in the expected frequency range of O-H stretch modes indicate that H-related defects are responsible. In this work the thermal stability of these absorption lines have been investigated, and the results are given in section 5.4.1

The absorption peaks close to 4200 cm^{-1} have previously been identified as internal electronic transitions of substitutional Ni^0_{Zn}, split by the local crystalline field [24, 48]. This previous assignment was based on the fact that Ni had been intentionally introduced into the samples that were studied, and that the observed absorption peak positions showed an agreement with calculations. However, reference spectra without Ni were not presented in refs. [24, 48], and the authors of ref. [48] comment that "the assignment of this line is still not indisputable." The results presented in this work give strong evidence supporting the assignment of the absorption lines to Ni impurities. This is further discussed in section 5.3.

5.2 Effect of H_2/D_2 gas anneals

To obtain a further understanding of the role of H in ZnO, hydrogen and/or deuterium were introduced into the three different ZnO crystals, labeled A-1, A-2 and C, by annealing the samples in quartz ampoules filled with H_2, mixed H_2/D_2 and D_2 gas, respectively (see section 4.4.2 for details). A marked decrease in resistivity was observed in all three samples after the H_2/D_2 gas anneals, as discussed further in section 5.10.

Several changes were also observed in the IR spectra after the gas anneals,

including changes in the existing absorption peaks and the appearence of new ones, summarized in tables 5.1 and 5.3. In sample A-1, the strong absorption line at 3577 cm^{-1}, assigned to a OH-Li complex, increases with a factor of $\sim$ 1.5 after the H_2 anneal, while the less stable 3336 cm^{-1} line disappears. The same behavior is also observed in sample A-2 after the mixed H/D treatment, however with a less pronounced increase in the 3577 cm^{-1} peak. This is to be expected, as a fraction of Li will also be bound up in the equivalent OD-Li configuration. A new line is observed at 3303 cm^{-1} in both samples after hydrogenation, visible in both the $\vec{k}\perp\vec{c}$ and $\vec{k}\|\vec{c}$ orientations. In addition, a broad line emerges at 3321 cm^{-1} in sample A-1 measured in the $\vec{k}\perp\vec{c}$ orientation, while a sharp peak is seen at 2783 cm^{-1} in the $\vec{k}\|\vec{c}$ orientation of sample A-2. All these lines are located in the region characteristic of O-H stretch modes (3200-3700 cm^{-1}) [10], except the line at 2783 cm^{-1}. This line has however previously been assigned to an O-H LVM with a high degree of anharmonicity [47] (see section 5.9 for details). The intensity of these peaks before and after the gas anneals are summarized in table 5.1.

When hydrogen is substituted by deuterium, the frequencies of the 3577, 3303 and 2783 cm^{-1} peaks are shifted to 2644, 2465 and 2106 cm^{-1}, representing a frequency ratio of 1.35, 1.34 and 1.32, respectively. The frequency ratios are close to the value 1.37 expected for a harmonic oscillator consisting of a oxygen atom bound to hydrogen/deuterium, as calculated in section 2.2.6. Based on this, we identify the three lines at 3577, 3303 and 2783 cm^{-1} as LVMs of O-H stretch modes. To facilitate the discussion, the defect absorbing at 3577 cm^{-1} will be referred to as OH-Li in the following. Because the origin of the defects responsible for the 3303 and 2783 cm^{-1} LVMs are less known than that of the 3577 cm^{-1} line, they are labeled H-X and H-Y, respectively.

Because of the low resistivy of the samples after hydrogenation, a strong electronic absorption was observed. Particularly, this was a challenge for the measurements performed in the $\vec{k}\perp\vec{c}$ orientation, due to a larger absorption thickness. This resulted in a close to zero transmission in the low frequency range, and consequently, only the O-D replica of the 3577 cm^{-1} line was observed in the sample annealed in D_2 gas, while no O-D replica was found for the 3321 cm^{-1} line. However, due to the fact that the 3321 cm^{-1} peak was observed after hydrogenation and that the frequency is in the expected range of O-H stretch modes, this LVM is also assigned to a O-H LVM.

In addition to the peaks mentioned above, two weaker peaks at 2461 and 2480 cm^{-1} were observed in the samples treated in D_2 and H_2/D_2, near the O-D LVM of

Measurement			Absorption peaks (cm^{-2})							
Sample	Treatment	Orientation	O-D LVMs			O-H LVMs				
			2106	2465+	2644	2783	3303+	3321	3336	3577
A-2	As-grown	$\vec{k}\perp\vec{c}$	NA	NA	NA	-	-	-	0.16	1.73
A-2	As-grown	$\vec{k}\parallel\vec{c}$	-	-	-	-	-	-	0.33	-
B-1	As-grown	$\vec{k}\perp\vec{c}$	-	-	-	-	-	-	0.64	1.72
B-1	As-grown	$\vec{k}\parallel\vec{c}$	-	-	-	-	-	-	1.55	-
A-1	H_2	$\vec{k}\perp\vec{c}$	-	-	-	-	0.99	1.04	-	2.54
A-1	H_2	$\vec{k}\parallel\vec{c}$	-	-	-	-	2.59	-	-	-
A-2	H_2/D_2	$\vec{k}\perp\vec{c}$	NA	NA	NA	-	3.35	-	-	1.79
A-2	H_2/D_2	$\vec{k}\parallel\vec{c}$	1.52	3.07	-	3.73	4.44	-	-	-
D	D_2	$\vec{k}\perp\vec{c}$	NA	NA	1.00	-	-	-	-	-
D	D_2	$\vec{k}\parallel\vec{c}$	2.01	6.00	-	0.18	-	-	-	-

Table 5.1: Integrated absorption coefficients of the main observed peaks before and after H_2 and/or D_2 gas anneals, measured in both $\vec{k}\perp\vec{c}$ and $\vec{k}\parallel\vec{c}$ directions. "+" denotes that an absorption feature may consist of several overlapping peaks. In these cases, the total integrated intensity is shown. "-" denotes no observable peak, and *"NA"* that spectroscopic data were not available in the relevant region, due to a strong absorption from free carriers.

the H-X defect at 2465 cm^{-1}. Also, a splitting was observed in the 3303 and 2465 cm^{-1} peaks arising from the H-X defect after mixed H_2/D_2 treatment. A further discussion of this splitting, together with the temperature stability and origin of these lines can be found in section 5.6. It will also be argued that the LVM at 3321 cm^{-1} is associated with the H-X defect. In the same way, the O-H/O-D stretch LVMs of the H-Y defect at 2783 and 2106 cm^{-1} will be discussed separately in section 5.7.

The increased intensity of the OH-Li LVM at 3577 cm^{-1} after H_2 anneal will be discussed further in section 5.5.2, and related to the concentration of OH-Li complexes in the sample.

5.3 Ni-related absorption lines

As shown in figure 5.1 and 5.2, there is a large difference in the intensity of the IR absorption peaks around 4200 cm^{-1} in the as-grown spectra of samples from wafers A and B. Motivated by this, a mass spectrum was measured by SIMS on samples from both wafers to reveal a possible variation in impurity concentration in between the two wafers. As shown in figure 5.3, the only isotopes which showed a significant difference in concentration between wafers A and B is the two stable isotopes of Ni, ^{58}Ni and ^{60}Ni. To obtain a more precise determination of the Ni concentrations, Ni depth profiles were measured on both samples, and the results are presented in figure 5.4. Notice that the total Ni concentration is $\sim$ 11 times higher in wafer A as

Wafer	$I_{Ni,tot} = \int \alpha(\tilde{\nu})d\tilde{\nu}$ (cm^{-2})	$[Ni]$ (cm^{-3})	$\epsilon = I_{Ni}/[Ni]$ (cm)
A	11.47	$5.93 \cdot 10^{17}$	$1.93 \cdot 10^{-17}$
B	1.53	$5.24 \cdot 10^{16}$	$2.91 \cdot 10^{-17}$

Table 5.2: Absorption cross sections ϵ for the Ni absorption lines at 4216, 4240 and 4246 cm^{-1} measured on samples from two different ZnO wafers.

compared to wafer B. This difference is comparable that in the integrated intensity of the IR peaks around 4200 cm^{-1}.

Based on the direct correlation between the Ni concentration and intensity of the IR absorption lines we conclude that the lines indeed are Ni-related, supporting the original assignment of Kaufmann et al. [24]. The absorption lines at 4216, 4240 and 4246 cm^{-1} will in the following discussion therefore be assumed to originate from substitutional Ni_{Zn} defects, where Ni is in the 2+ charge state (in ionic terms). From the measured Ni concentrations and IR absorption strengths, it is also possible to determine an absorption cross section ϵ_{Ni} for Ni^0_{Zn} impurities, as defined in eq. 2.25. The results are shown in table 5.2, where the absorption per ion per cm is defined from the total integrated intensity of the lines at 4216, 4240 and 4246 measured in the $\vec{k} \perp \vec{c}$ orientation. As seen from table 5.2, the value of ϵ_{Ni} varies with a factor of $\sim$ 1.5 depending on the sample. It is important to remember that the values for ϵ_{Ni} assume that all of the Ni concentration measured by SIMS takes part in the absorption, and ϵ_{Ni} should therefore be considered as a minimum value. The value of ϵ_{Ni} calculated from wafer A is the smallest of the two, and is thus disregarded, giving the (minimum) absorption cross section as the value calculated from wafer B:

$$\epsilon_{Ni} \geq 2.91 \cdot 10^{-17} cm. \tag{5.1}$$

One possible explanation for the discrepancy in ϵ_{Ni} is that the high Ni concentration in wafer A leads to formation of Ni-related complexes, resulting in a lower absorption than expected. Another possibility is that not all the Ni ions present in wafer A take part in the absorption because they are not in the effectively neutral, $Ni^0{}_{Zn}$ charge state. It has previously been found that Ni in ZnO shows luminescence from a different charge state [48], indicating a donor-like behavior, e.g.

$$Ni^0_{Zn} \rightleftharpoons Ni^+_{Zn} + e^- \tag{5.2}$$

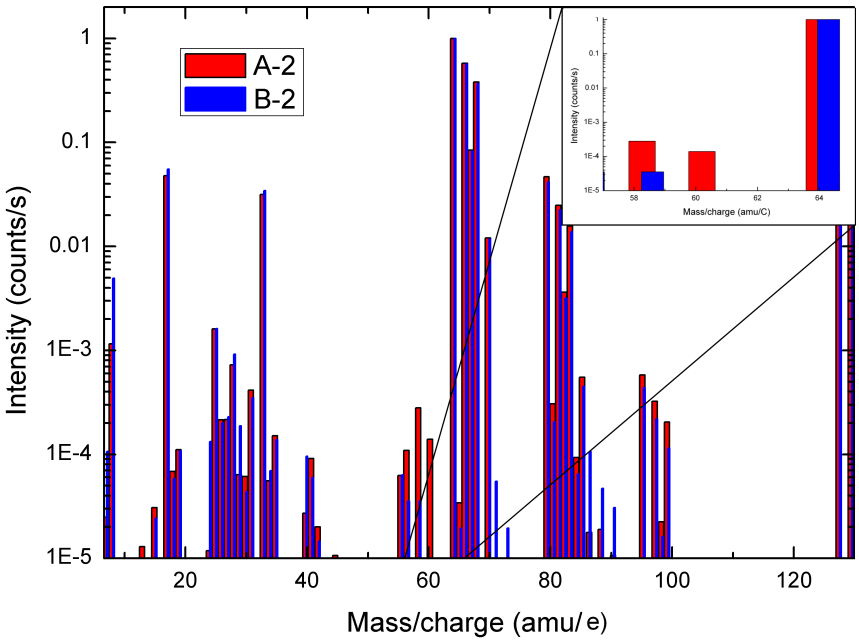

Figure 5.3: SIMS mass spectra of two different ZnO samples, normalized to the ^{64}Zn-signal. Inset: The peaks originating from ^{58}Ni and ^{60}Ni show the biggest relative difference.

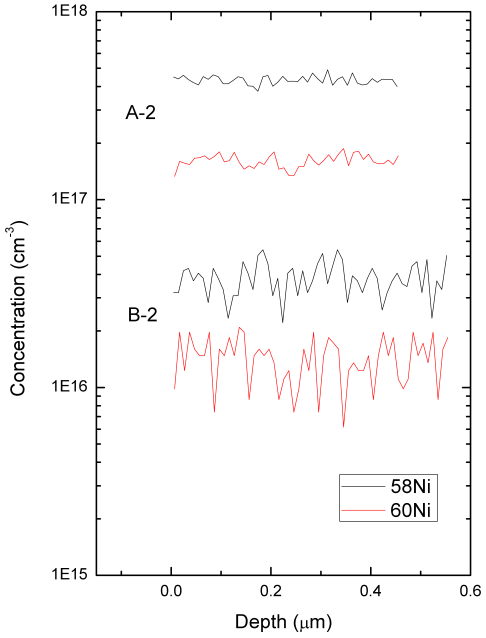

Sample	$[Ni]_{total}$ (cm^{-3})
A-2	$5.93 \cdot 10^{17}$
B-2	$5.24 \cdot 10^{16}$

Figure 5.4: Left: SIMS depth profiles showing the concentration of the ^{58}Ni- and ^{60}Ni-isotopes of Ni in two different ZnO samples. Right: Average total Ni concentrations calculated from the SIMS data.

Measurement			Absorption peaks (cm^{-2})	
Sample	Treatment	Orientation	4216	4240/4246
A-2	As-grown	$\vec{k}\perp\vec{c}$	0.54	10.93
A-2	As-grown	$\vec{k}\parallel\vec{c}$	1.30	9.45
B-1	As-grown	$\vec{k}\perp\vec{c}$	0.10	1.43
B-1	As-grown	$\vec{k}\parallel\vec{c}$	0.14	0.87
A-1	H_2	$\vec{k}\perp\vec{c}$	0.73	13.14
A-1	H_2	$\vec{k}\parallel\vec{c}$	1.65	10.60
A-2	H_2/D_2	$\vec{k}\perp\vec{c}$	0.66	11.17
A-2	H_2/D_2	$\vec{k}\parallel\vec{c}$	1.35	9.55

Table 5.3: Integrated absorption coefficients of the Ni-related absorption peaks before and after H_2 and H_2/D_2 gas anneals, measured in both $\vec{k}\perp\vec{c}$ and $\vec{k}\parallel\vec{c}$ directions.

The measured resistivity is approximately 10 times higher in the samples from wafer A than the samples from wafer B, suggesting that the concentration of conduction band electrons is lower in wafer A. This will shift the equilibrium in eq. 5.2, thus favoring Ni_{Zn}^{+} over Ni_{Zn}^{0}, resulting in a higher apparent absorption cross section. This interpretation is also supported by hydrogenation experiments. As shown in table 5.10, hydrogenation of samples A-1 and A-2 is followed by a four orders of magnitude decrease in resistivity. Table 5.3 shows the intensity of the Ni_{Zn}^{0}-related peaks close to 4200 cm^{-1} before and after hydrogenation, showing that this treatment also results in an up to 20 % increase in the Ni absorption peak intensity, giving a value for ϵ_{Ni} approaching the one that was found for wafer B. In any case, using the value for ϵ_{Ni} given in eq. 5.1, IR data may now be used for quantification of the (minimum) Ni_{Zn}^{0} concentration in ZnO samples.

5.4 Weak LVMs present in the as-grown samples

5.4.1 Thermal stability

In order to study the annealing behavior of the hydrogen-related defects present in the as-grown state, a series of isochronal heat treatments (annealings) were performed on sample B-1 at various temperatures in the range 100-1300 °C, and IR absorption spectra were recorded in the $\vec{k}\perp\vec{c}$ orientation at a sample temperature of $\sim$ 15 K after each step. The annealings were performed in an open tube furnace and the duration of each treatment was 30 min.

As seen in figure 5.5, the intensities of the three absorption lines at 3336, 3483 and 3516 cm^{-1} decrease markedly already after annealing at 100 °C. The intensities continue to decrease after 150 °C, before starting to increase after both 200 and 250 °C. After the sample had been stored in room temperature for six weeks, the IR

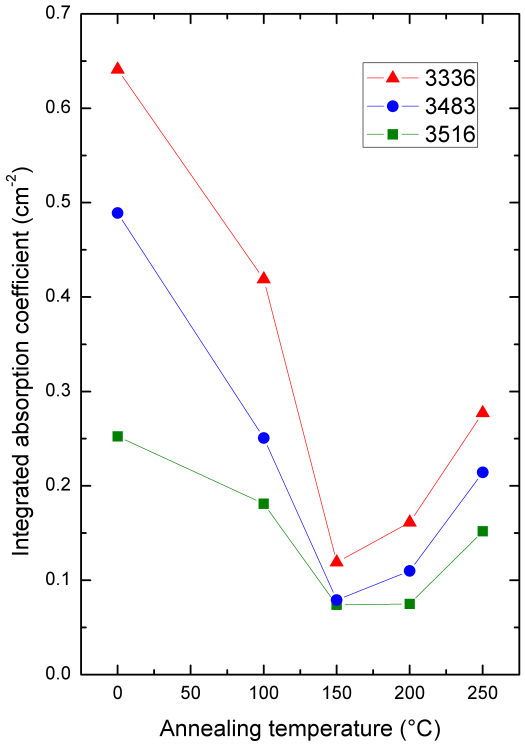

Figure 5.5: Intensity (integrated absorption coefficient) of selected peaks presented in figure 5.2 as a function of annealing temperature. The annealing time step was 30 min and the annealings were performed in air. The spectra were measured in the $\vec{k} \perp \vec{c}$ orientation.

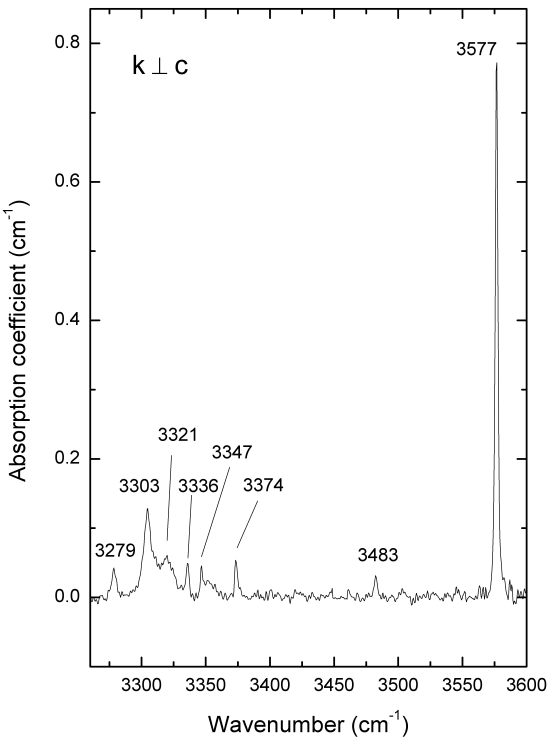

Figure 5.6: IR absorptions spectrum of sample B-1 after annealing in air at 500 °C for 30 min, measured in the $\vec{k} \perp \vec{c}$ orientation. New absorption peaks are observed in the spectrum at 3303, 3321, 3347 and 3374 cm^{-1}.

spectrum showed almost complete disappearance of all the three peaks.

Surprisingly, after annealing the sample at 500 °C for 30 min, the peaks at 3279, 3336 and 3483 cm^{-1} reappeared, as shown in figure 5.6. In addition, new peaks emerged at 3303, 3321, 3347 and 3374 cm^{-1}. The lines at 3336 and 3483 cm^{-1} disappeared after further annealing at 600 °C, while the rest of the peaks persisted until 800 °C (not shown).

The results related to the thermal stability of the absorption lines at 3279, 3336, 3483 and 3516 cm^{-1} are not conclusive, and it is beyond the scope of this work to conclude on this subject. However, it is possible to say that the absorbing defects seem to dissociate at low temperatures, but that H may be retrapped in one of these configurations even after annealing at moderate temperatures (500 °C). Since the common methods of introducing H and/or D into ZnO involve annealing at higher

temperatures, this may also explain why no deuterium replicas of these lines have been reported in the literature.

The appearing LVMs at 3303 and 3321 cm^{-1} were also found in samples A-1 and A-2 after hydrogenation and was assigned to the H-X defect. This defect will be discussed further in section 5.6. The lines at 3347 and 3374 cm^{-1} have previously been shown to originate from the same defect [72], here labeled H-Z. The H-Z defect will be discussed in section 5.8.

5.5 The OH-Li defect

5.5.1 Thermal stability

The 3577 cm^{-1} peak arising from a OH-Li complex has previously been shown to be highly stable, even withstanding annealing at 1200 °C for 30 min [58]. Only after several hours at 1200 °C could the 3577 cm^{-1} peak be eliminated. Oddly enough, no reproducible value was found for the decay rate [58] (see section 3.6.3 for details).

By continuing the isochronal annealing study presented in the preceding section, we have investigated the thermal behavior of the OH-Li complex in the temperature range from 100 to 1300 °C, with an annealing time of 30 min. IR absorption spectra were measured in the $\vec{k} \perp \vec{c}$ orientation after each annealing step.

Figure 5.7 shows the integrated intensity of the 3577 cm^{-1} peak as a function of annealing temperature. The intensity varies between 1.5 and 2.5 cm^{-2} in the whole temperature range from RT to 1250 °C. After subsequent annealing of the sample at 1300 °C, the 3577 peak completely disappeared.

In an attempt to gain a further understanding of these results, the data presented in figure 5.7 have been fitted to a thermally activated dissociation model, as described in ref. [84]. Under the assumption that the defect dissociates irreversibly during annealing, the defect concentration can be expressed as a function of the annealing time t and the temperature T. In a first order dissociation reaction, the rate of change in the concentration is proportional to the remaining concentration at any time t. By eq. 2.25, the same relation holds for the integrated peak intensity I:

$$\frac{dI(t)}{dt} = -cI(t). \tag{5.3}$$

A solution to this differential equation for the boundary conditions $I(0) = I_o$ and $I(\infty) = 0$ is

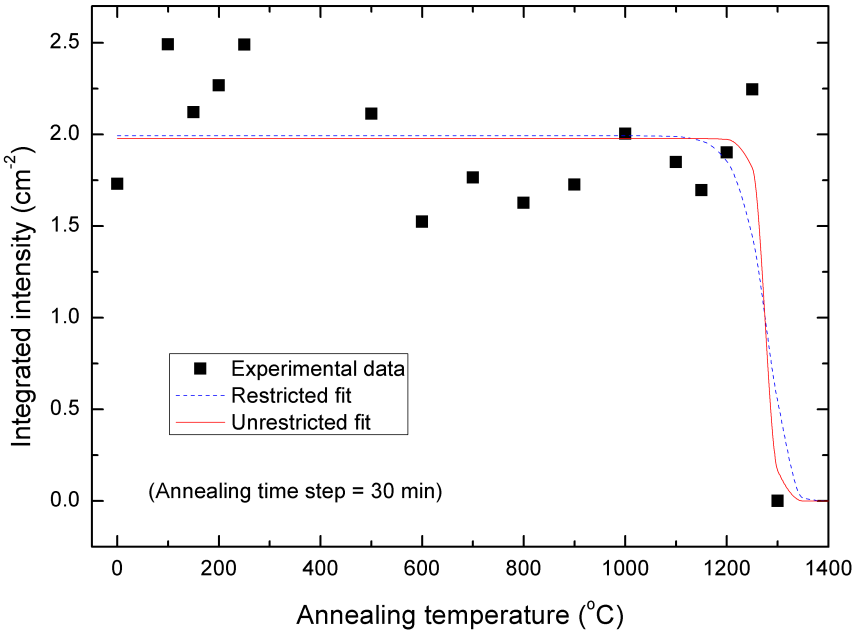

Figure 5.7: The intensity (integrated absorption coefficient) of the 3577 cm^{-1} peak as a function of annealing temperature for a series of 30 min anneals. The solid line shows an unrestricted fit to a model assuming first order dissociation kinetics. The dashed line is a fit to the same model, constraining the preexponential factor c_0 to a value of $1{\cdot}10^{13}$ s^{-1}.

$$I(t) = I_o e^{-ct} \tag{5.4}$$

With the decay constant c defined as

$$c = c_o e^{-E_a/k_B T} \tag{5.5}$$

where c_o is the "attempt frequency", E_a is the activation energy for dissociation, T is the absolute temperature and k_B is Boltzmann's constant. c_o is given by the frequency of vibration of the crystal lattice, and normally takes values close to the Debye frequency ($\approx 10^{13}$ s^{-1}) [12]. A non-linear, least-squares optimalization algorithm was used to fit the model to the data, with I_o, c_o and E_a as free parameters. From the results, it is evident that to fit the model to the abrupt drop in the integrated intensity between 1250 and 1300 °C, the c_o parameter needs to take an unphysical value of $\sim 10^{40}$ s^{-1}. By fitting the data while constricting the c_o parameter to a more reasonable value of 10^{13} s^{-1}, the intensity drop of the model is less abrupt and does not match the experimental values. Both fits are shown in figure 5.7, and the

	I_o (cm^{-2})	c_o (s^{-2})	E_a (eV)	χ^2	Comment
Unrestricted fit	1.98	$9.13 \cdot 10^{39}$	13.92	1.46	(Unphysical c_0)
Restricted fit	1.99	$1.00 \cdot 10^{13}$ (fixed)	5.63	2.18	(Unjust fit)

Table 5.4: Calculated parameters of the first order dissociation model given by eq. 5.3-5.5, fitted to the data shown in figure 5.7. The χ^2 value indicates the quality of the fit (lower is better).

calculated parameters are given in table 5.4.

In addition, the first order model predicts a constant intensity when annealing at lower temperature, and can thus not be used to explain the observed intensity variation in this temperature range. Based on this lack in correspondence between the first order model and the experimental data, we conclude that the OH-Li defect does not dissociate irreversibly following first order dissociation kinetics. This is in agreement with the findings of Lavrov et al. [58], who proposed that the apparent stability of the defect is determined mainly by the recapture and diffusion of hydrogen and that dissociation of OH-Li may occur also at lower temperatures. This however implies that an exchange of H between the OH-Li complex and a another not IR-active H configuration is taking place during the annealing. This assumed other configuration, possibly H_2 molecules, must also be thermally stable at temperatures up to ~ 1200 °C.

Another strong evidence for this view is presented in figure 5.8, showing an IR absorption spectrum measured on sample C after annealing in a D_2 atmosphere at 700 °C for 1 hour. The absorption line at 3577 cm^{-1} is not observed in the spectrum, however a new peak has appeared at 2644 cm^{-1}, with an intensity comparable to that of the 3577 cm^{-1} peak normally found in as-grown samples. The peak at 2644 cm^{-1} has previously been identified as a O-D replica of the 3577 cm^{-1} line, and may thus be assigned to a OD-Li complex analogous to OH-Li. This indicates that all the H bound to Li in the as-grown sample has been exchanged with D. Assuming a similar formation energy for OH-Li and OD-Li, OH-Li must dissociate with a substantial rate at 700 °C for this to be possible. Also, within 1 hour at 700 °C, D must be able to diffuse into the bulk of the crystal. A similar behavior has previously been observed by Li et al. [47] in HT samples annealed in D_2 gas.

Figure 5.9 shows the 3577 cm^{-1} line in sample A-2 in the as-grown state, after mixed H_2/D_2 treatment and subsequent annealing at 800 °C. A marked drop in intensity is seen already after the annealing at 800 °C. After 900 °C the intensity

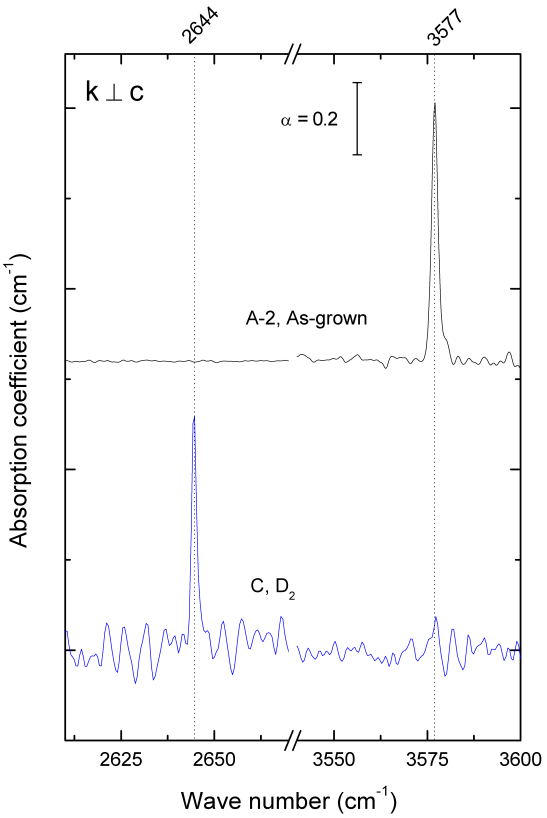

Figure 5.8: IR absorption spectrum of sample A in the as-grown state (top) and sample C after annealing in D_2 gas (bottom), measured in the $\vec{k} \perp \vec{c}$ orientation. A new absorption peak emerges at 2644 cm^{-1}, after the D_2 anneal, substituting the 3577 cm^{-1} line.

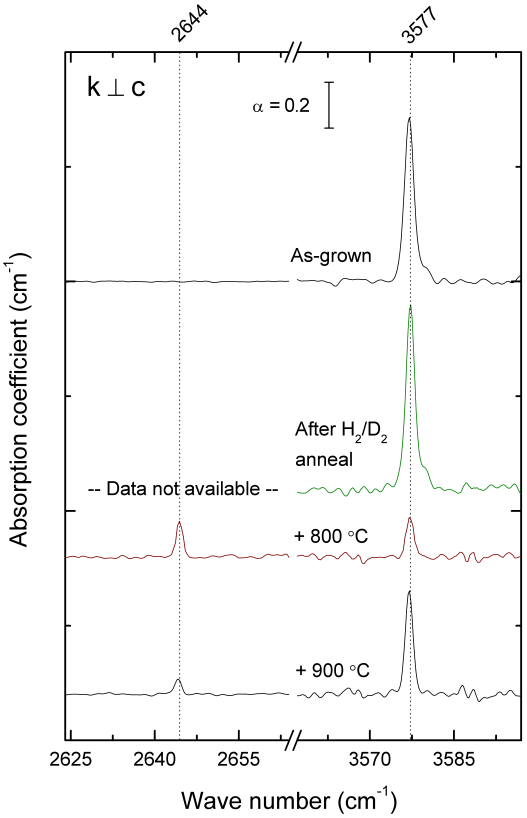

Figure 5.9: IR absorption spectra showing the 3577 and 2644 cm^{-1} lines in the as-grown state (top), after H_2/D_2 gas anneal (middle) and after subsequent annealing in air at 800 and 900 °C for 30 min (bottom). Spectra are measured on sample A-2 in the $\vec{k} \perp \vec{c}$ orientation.

of the OH-Li LVM rises to almost half its original value, while the OD-Li LVM decreases. These findings also suggests that a exchange of H is going on during the annealing. Note that the (apparent) stability of the OH-Li complex may vary from sample to sample, and may possibly also be affected by the hydrogenation procedure. Further investigations are needed to clarify these matters. Some experiments are suggested in section 6.2.

If the OH-Li concentration after annealing is determined by a combined mechanism of dissociation, diffusion and recapture, the heating and cooling process may have a big influence on the result. A possible hypothesis is that a fraction of the OH-Li complexes dissociate into free Li_{Zn}/Li_i and H_i during annealing, which then recombine into OH-Li and e.g. H_2 molecules when the sample is cooled to room temperature. To examine this possibility, an as-grown ZnO sample (sample D) was subjected to two rapid thermal processings (RTP) at 600 °C for 2 min and 10 min. In RTP, rapid heating rates are attained by the use of high intensity lamps. The sample may also be rapidly cooled by cutting the lamp power and purging the sample chamber with cold gas[1]. IR absorption spectra were measured in the $\vec{k} \perp \vec{c}$ orientation between each treatment. As shown in figure 5.10, no significant change was observed in the intensity of the 3577 cm^{-1} line after the 2 min RTP treatment, but a $\sim$ 20% drop was observed after the 10 min treatment. It is diffucult to draw any conclusions based on this experiment alone, however the data seem to be in agreement with the results presented above, suggesting that the OH-Li complex may dissociate also at lower annealing temperatures than 1200 °C. In addition to the 3577 cm^{-1} line, two weak absorption lines emerge at 3303 and 3321 cm^{-1} after the RTP treatment. These two lines have been assigned to the H-X defect, and will be discussed further in section 5.6.

5.5.2 Quantification of the OH-Li content

Because O-H stretch modes are easily detected by IR absorption spectroscopy they may serve as a tool for a quantitative determination of the hydrogen content. The largest intensity of the 3577 cm^{-1} peak associated with the OH-Li complex was observed in sample A-1 after the H_2 gas anneal, with $I = 2.54\, cm^{-2}$. From table 5.5, the average Li concentration in wafer A is found to be $2 \cdot 10^{17}$ cm^{-3}. Assuming that a single Li ion is involved in the OH-Li defect, this value gives an upper bound for the OH-Li concentration in the sample A-1.

[1] The temperature profile for the RP treatment is given i appendix A.2

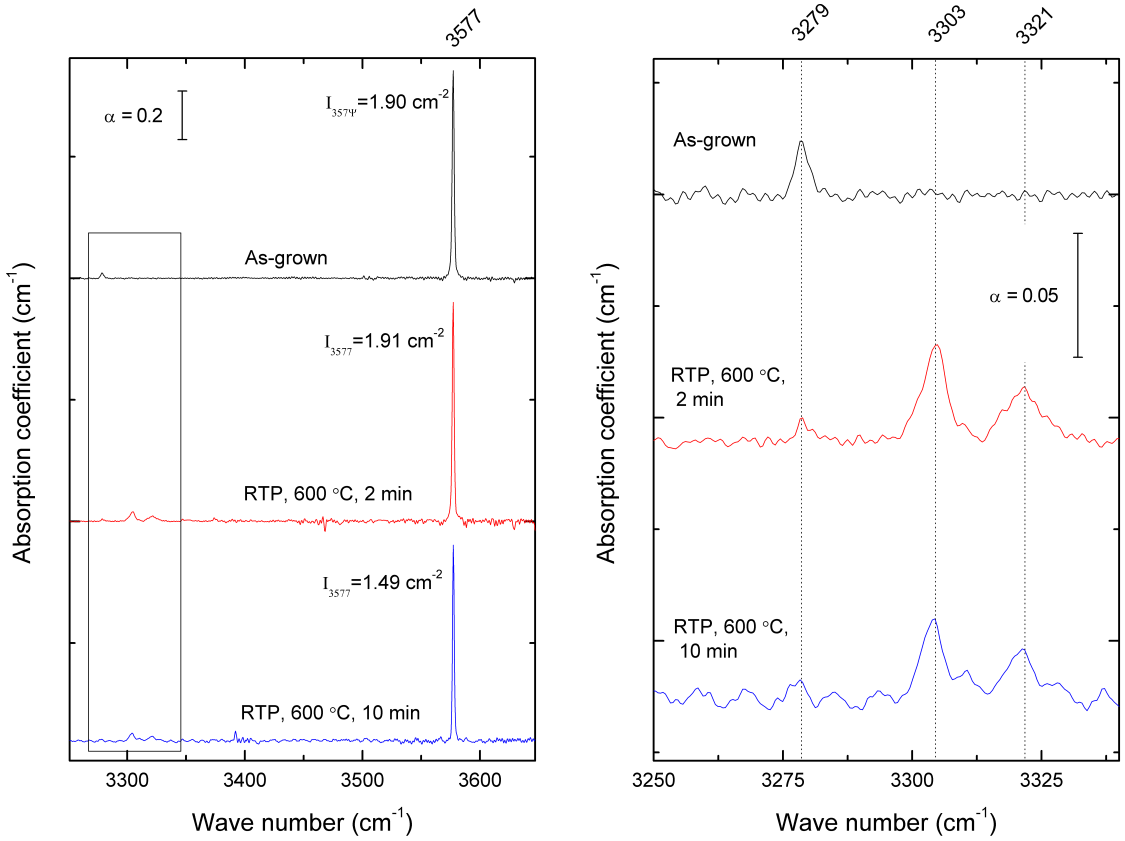

Figure 5.10: Left: IR absorption spectra measured on sample D in the as-grown state, and after two different rapid thermal processings at 600 °C. Right: Detailed view, marked with a box in the left graph, showing new peaks emerging at 3303 and 3321 cm^{-1}.

Sample	[Li] (cm^{-3})
A-2	$2 \cdot 10^{17}$
B-2	$3.8 \cdot 10^{17}$

Table 5.5: Li concentration in two different samples, calculated from an average of SIMS depth profiles.

From this, a lower bound for the absorption cross section can be found. The absorption cross section was defined in section 2.3 as

$$\epsilon_i = \frac{I_i}{c_i}, \tag{5.6}$$

where I_i is the integrated absorption coefficient $I = \int \alpha_i(\tilde{\nu}) d\tilde{\nu}$ caused by species i. By assuming a uniform H concentration and using the subscripts $_I$ and $_{II}$ to denote the various quantities in the as-grown state and after hydrogenation, we get:

$$\epsilon_{3577} = \frac{I_{3577,II}}{[OH - Li]_{II}} \geq \frac{I_{3577,II}}{[Li]} = \frac{2.54\ cm^{-2}}{2 \cdot 10^{17}\ cm^{-3}} \approx 1.27 \cdot 10^{-17}\ cm. \tag{5.7}$$

Previously, a lower bound for ϵ_{3577} has been estimated to be $1.72 \cdot 10^{-18}$ cm [85]. Hence, our results represent an adjustment of this value. Absorption cross sections ϵ_{OH} have also previously been accurately measured for unassociated O-H and O-D bonds in TiO_2, $LiNbO_3$ and SiO_2. A less direct calculation of ϵ_{OH} based on comparison with Raman data has also been done for the 3611 cm^{-1} LVM in ZnO, assigned to an unassociated O-H_{BC} donor [55]. The reported values are given in table 5.6 [2]. These calibration data, although only valid for specific materials, have also been used to determine H concentrations in several studies dealing with other compounds [10]. ϵ_{3577} extracted in eq. 5.7 lies in the lower range of the literature data, which seems reasonable considering that it is a minimum value. Note also that the highest reported ϵ_{OH} is not more than ~ 5 times higher than ϵ_{3577}, indicating that a significant fraction of the measured Li concentration is bound up in OH-Li after hydrogenation. As described in section 4.4.2, the H solubility during the hydrogenation conditions is estimated to be $\sim 5 \cdot 10^{17}$ cm^{-3}. If equilibrium conditions were reached, the H concentration should thus exceed the Li concentration in the bulk of the sample by a factor of ~ 2.5. Together with the high thermal stability of the OH-Li complex, this indicates that the value for ϵ_{3577} given

[2] Note that some of these values were originally reported using a base 10 logarithm for the absorbance, and have therefore been multiplied with $ln(10) = 2.30$ to be comparable to our values.

Material	ϵ_{OH} (10^{-17} cm)	ϵ_{OD} (10^{-17} cm)	Ref.
ZnO[a]	2.46	1.54	[55]
TiO_2	5.78	3.06	[86]
$LiNbO_3$	2.10	1.60	[87]
SiO_2	6.33	-	[88]

[a] Calibration of the unassociated O-H LVM at 3611 cm^{-1}

Table 5.6: Reported values for the absorption cross section ϵ of free O-H and O-D bonds in different materials.

in eq. 5.7 is reasonable.

From eq. 5.7 it is now possible to deduce the (maximum) OH-Li concentration in wafer A in the as-grown state:

$$[OH - Li]_I \leq \frac{I_{3577,I}}{\epsilon_{3577}} = \frac{1.73\ cm^{-2}}{1.27 \cdot 10^{-17}\ cm} \approx 1.4 \cdot 10^{17}\ cm^{-3} \tag{5.8}$$

If the value for ϵ_{OH} previously reported by Lavrov et al. [55] (see table 5.6) is used, the concentration of OH-Li in wafer A is estimated to be $7.0 \cdot 10^{16}$ cm^{-3} in the as-grown state and $1.0 \cdot 10^{17}$ cm^{-3} after hydrogenation.

5.6 The H-X defect

Figure 5.11 shows a selected region of the IR absorption spectra measured on sample A-2 in the as-grown state and on sample A-1, C and A-2 after heat treatment in H_2, mixed H_2/D_2 and D_2 gas, respectively. After these treatments the LVMs of the H-X defect emerges in the spectra. The intensities of the peaks in the different samples are given in table 5.1. By examining the different spectra given in figure 5.11 several general features can be noticed:

- In the hydrogenated sample, only the main 3303 cm^{-1} peak is observed in the $\vec{k}\|\vec{c}$ orientation, whilst an additional, nearby peak of similar intensity is seen at 3321 cm^{-1} in the $\vec{k}\perp\vec{c}$ orientation.

- In the sample treated with deuterium, the O-D replica of the 3303 cm^{-1} LVM can be seen to consist of a strong peak at 2465 cm^{-1} with a smaller peak on each side, at 2461 and 2480 cm^{-1}. However no O-H replicas of these peaks are observed near the 3303 cm^{-1} peak in the sample annealed in H_2 gas.

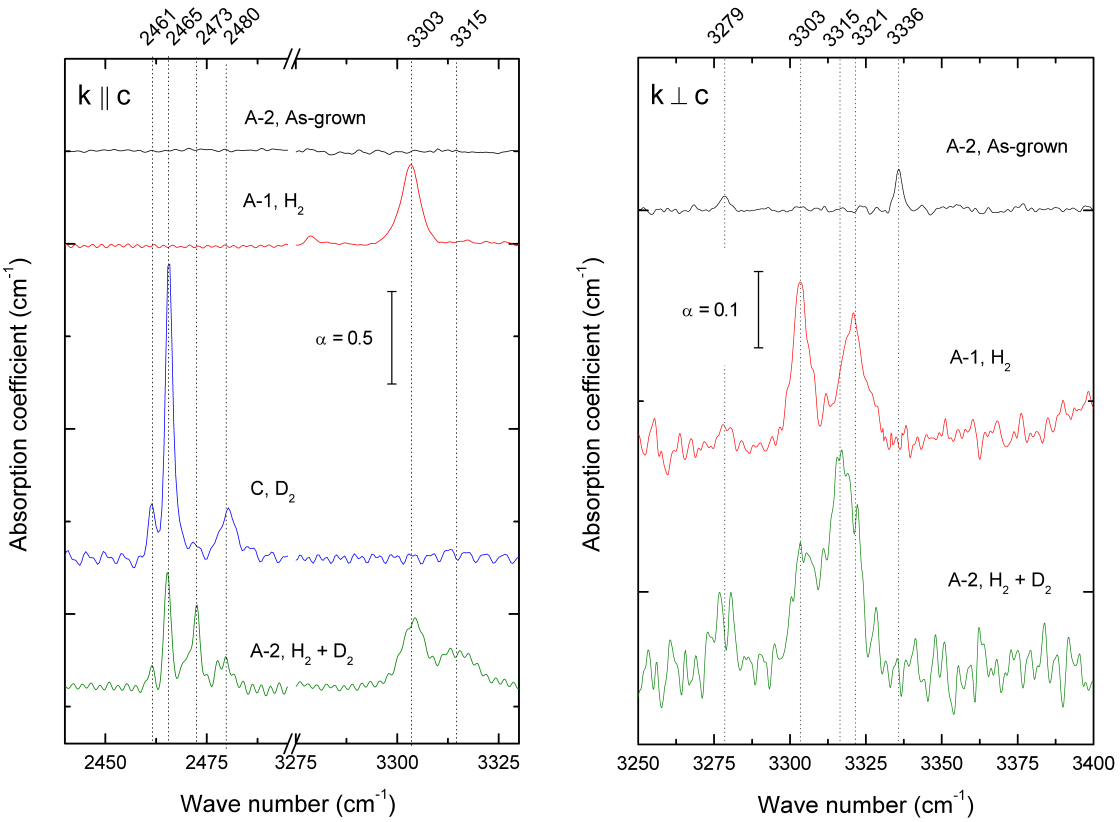

Figure 5.11: IR absorption spectra showing the peaks around 3303 and 2465 after various H_2 and/or D_2 gas anneals, measured in the $\vec{k}\|\vec{c}$ (left) and $\vec{k}\perp\vec{c}$ (right) orientations. A strong electronic absorption hindered the collection of data at low wave numbers in the $\vec{k}\perp\vec{c}$ direction.

- In the sample annealed in a gas mixture of H_2 and D_2, two additional lines at 2473 and 3315 cm^{-1} appear in the IR absorption spectrum.
- The intensity ratio between the 3303 and 3315 cm^{-1} peaks in the sample treated in mixed H_2/D_2 gas depend on the orientation of the measurement. In the $\vec{k}\|\vec{c}$ orientation 3303 is the strongest peak, with a weaker shoulder at 3315 cm^{-1}. In the $\vec{k}\perp\vec{c}$ orientation the absorption feature is broader, with a dominating peak near 3315 cm^{-1}.

5.6.1 Thermal stability

In order to investigate the thermal stability of these lines and look for possible correlations between them, IR absorption spectra were recorded on sample A-1 or

A-2 after each step in a series of isochronal annealings at temperatures in the range from 100 to 800 °C. The resulting spectra are presented in figure 5.12 and the total, normalized intensities of the peaks around 2465 and 3303 cm^{-1} as a function of annealing temperature are shown in figure 5.13. From the data it is evident that the two groups of peaks demonstrate a similar annealing dependency, indicating that they have the same origin. This also seems to hold for the two small peaks at 2461 and 2480 cm^{-1}. However, their relation to the other absorption lines is not entirely clear, due to the lack of O-H replicas in the vicinity of the main O-H peak at 3303 cm^{-1}.

In order to gain a further understanding of the annealing process, the first order dissociation model given by eqs. 5.3-5.5 has been applied, again assuming that the absorbing defect dissociates irreversibly during annealing. The model give a reasonably good fit to the data, using the values $E_a = 2.8$ eV for the activation energy and $c_o = 9.8 \cdot 10^{12}$ s^{-1} for the preexponential factor. Because of the limited amount of data, we can however not claim complete uniqueness of these parameters. Further investigations may therefore be needed, and some experiments are suggested in section 6.2. Notice from figure 5.13 that a low, remaining peak intensity after annealing at the highest temperatures could not be explained by the model, possibly indicating that some retrapping do occur when the sample is cooled.

5.6.2 Molecular model

To our knowledge, the IR absorption lines presented in this section are not previously reported in the literature. The appearence of extra lines after mixed H_2/D_2 treatment is a strong indication that the absorbing defect consist of more than one O-H bond, caused by a perturbation of the O-H (or O-D) stretch frequency by the neighboring D (or H) atom [64]. Moreover, the fact that only two new absorption lines are seen in the spectra indicates that the vibrational frequencies of the (O-H)...(O-D) and (O-D)...(O-H) configurations are equivalent. IR absorption signatures of both unassociated H and H bond to native point defects like V_{Zn} have previously been reported in other studies (see table 3.1). Hence, the fact that the 3303 cm^{-1} peak has not previously been observed by other groups indicates that H-X is associated with an impurity atom.

In an IR absorption measurement, only the component of a chemical bond's dipole moment directed along the electrical field vector of the light may take part in the absorption. Based on the observations of the peaks listed above, we propose

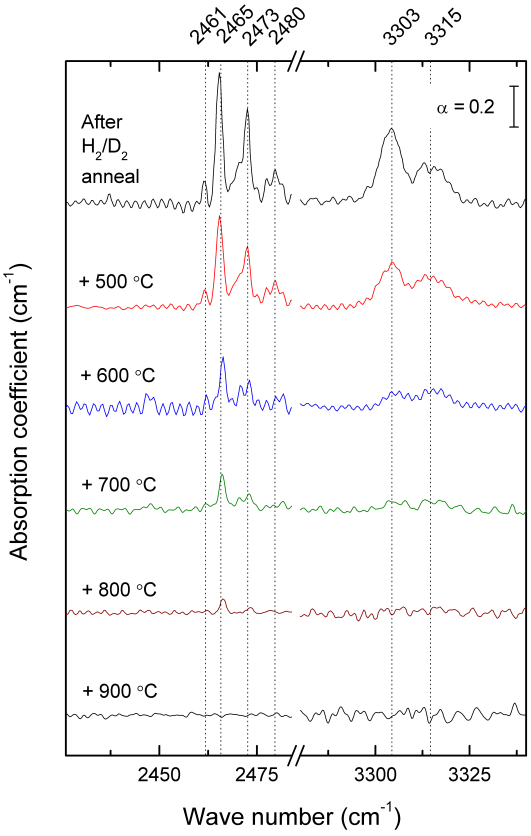

Figure 5.12: IR absorption spectra measured on sample A-2 in the $\vec{k}\|\vec{c}$ orientation, showing the peaks around 3303 and 2465 cm^{-1} after mixed H_2/D_2 treatment (top) and subsequent 30 min annealings.

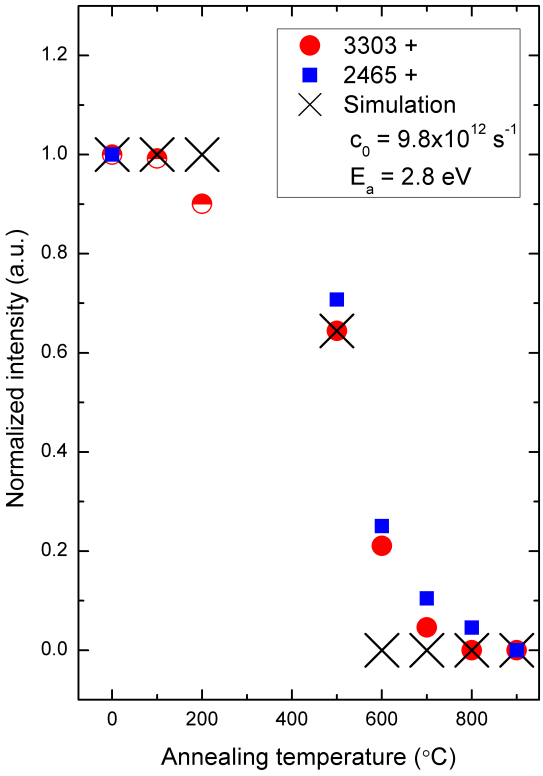

Figure 5.13: Normalized total intensity of the peaks around 3303 and 2465 cm^{-1} as a function of annealing temperature for a series of isochronal anneals (30 min each). Half-filled symbols are measured on sample A-1, filled symbols on sample A-2. Crosses indicate a fit to a model assuming first order dissociation kinetics.

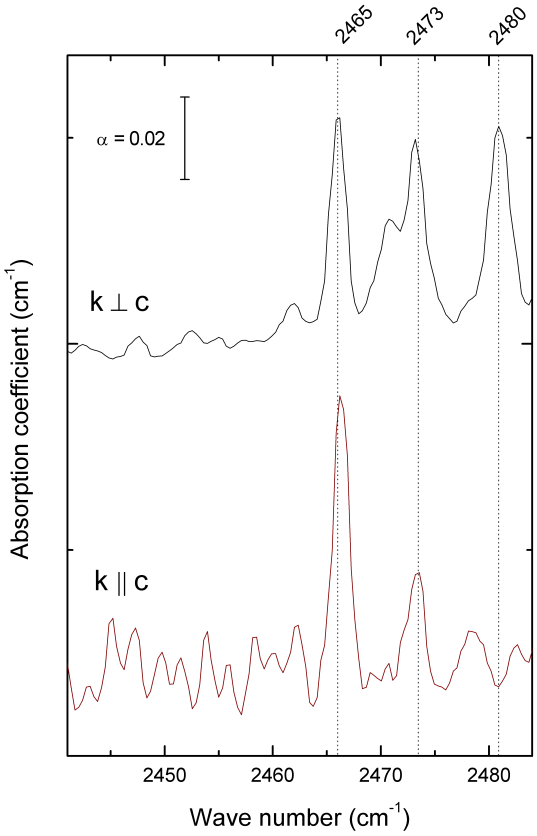

Figure 5.14: Selected region of two IR absorption spectra measured on sample A-2 after mixed H_2/D_2 treatment and subsequent annealing at 800 °C for 30 min. Spectra measured in the $\vec{k}\perp\vec{c}$ (top) and $\vec{k}\|\vec{c}$ (bottom) orientations are shown.

a model in which one of the O-H bonds is directed along the c-axis of the crystal with a LVM frequency of 3321 cm^{-1}, while the other is oriented at an angle from the c-axis, absorbing radiation at 3303 cm^{-1}. The O-H bond directed along the c-axis is only observable in the $\vec{k}\perp\vec{c}$ orientation. As described in section 5.2, IR absorption measurements in this region were not possible, due to a dominant electronic absorption. To determine the O-D replica of the 3321 cm^{-1} LVM a new IR measurement was therefore performed after annealing the sample at 800 °C. After the annealing, the carrier concentration was substantially lowered (see section 5.10), and a part of the H-X signal still remained in the spectrum. The result is presented in figure 5.14, showing three distinct peaks at 2465, 2473 and 2480 cm^{-1}. Like the 3321 cm^{-1} peak, the 2480 cm^{-1} peak is only visible in the $\vec{k}\perp\vec{c}$ orientation. It is thus highly probable that this peak is the O-D replica of the 3321 cm^{-1} LVM.

A proposed microstructural configuration for the H-X defect is shown in figure

5.15. The figure also includes the possible combinations of H and D in the three hydrogenated samples and the proposed absorption frequency for each O-H and O-D bond. Based on the expected number of O-H (or O-D) bonds in the model and their angle with the propagation direction of the IR beam, the predicted absorption peak intensities have been qualitatively determined, and are given in table 5.7. In order to quantify the intensity of the different overlapping peaks, the spectroscopic data were fitted to a sum of Lorentzian functions, as described in appendix A.4. The measured intensities of all the peak components are given in table 5.8, in reasonably good agreement with the predictions.

Some of the observed features are however still not accounted for. The model does not explain the presence of the weak absorption line at 2461 cm^{-1}. Also, the 2480 cm^{-1} LVM should not be observable in the $\vec{k}||\vec{c}$ orientation according to the model, contrary to results shown in figure 5.11.

In addition, the nature of the assumed impurity involved in the H-X defect is not yet clarified. The double peak at 3303 and 3321 cm^{-1} observed in the $\vec{k}\perp\vec{c}$ orientation after H_2 anneal (see figure 5.11) have also been observed in sample B-1 after annealing at 500 °C (figure 5.6) and in sample D after rapid thermal processing (RTP) at 600 °C for only 2 min (figure 5.10). No significant contamination is likely to occur during the 2 min RTP treatment, strongly indicating that the impurity involved in the H-X defect is present in the as-grown samples. From the integrated intensities presented in table 5.1 and the previously reported absorption cross sections shown in table 5.6, the H-X concentration after hydrogenation is estimated to be in the 10^{17} cm^{-3} range. No correlation have been found between the H-X LVMs and the Ni-related absorption lines (figure 5.17), indicating that Ni is not involved. However, impurities like Mg, Si and Fe are commonly present in similar concentrations (section 3.5.3), and may thus be responsible. Further investigations are needed to clarify these issues, and some possible experiments are suggested in section 6.2.

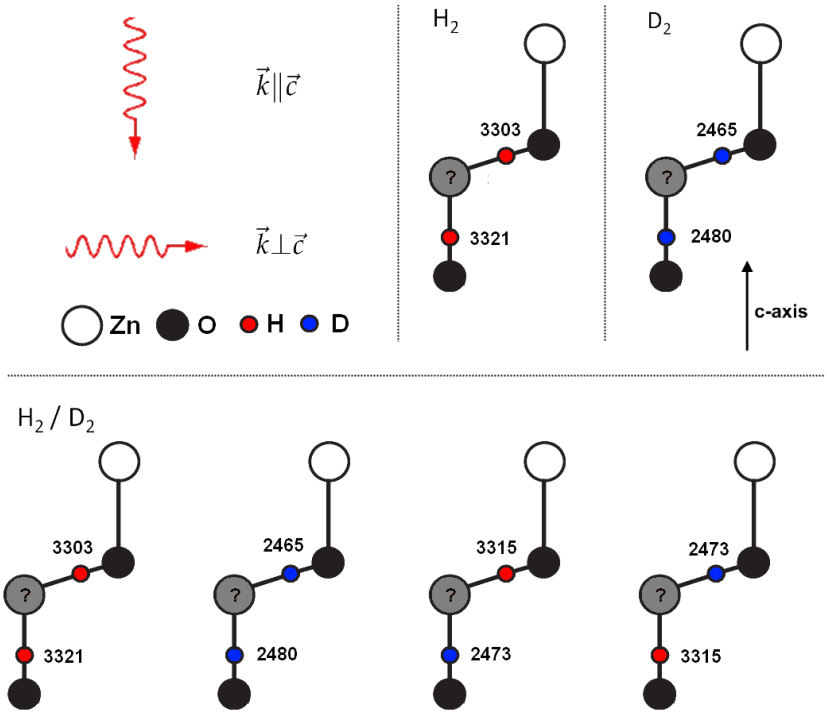

Figure 5.15: Possible configurations of the H-X defect after H_2 (top left), D_2 (top right) and H_2/D_2 (bottom) gas anneals. The frequency of the different O-H/O-D bonds are indicated in cm^{-1}, adjusted to fit the experimental data.

	Treatment	Orientation	2465	2473	2480	3303	3315	3321
	H_2	$\vec{k}\|\vec{c}$	-	-	-	Strong	-	-
	H_2	$\vec{k}\perp\vec{c}$	-	-	-	Medium	-	Strong
	D_2	$\vec{k}\|\vec{c}$	Strong	-	-	-	-	-
	D_2	$\vec{k}\perp\vec{c}$	Medium	-	Strong	-	-	
	H_2/D_2	$\vec{k}\|\vec{c}$	Medium	Medium	-	Medium	Medium	-
	H_2/D_2	$\vec{k}\perp\vec{c}$	Weak	Medium	Medium	Weak	Medium	Medium

Table 5.7: Expected intensities of the various peaks originating from the H-X defect, based on the model illustrated in figure 5.15.

Sample	Treatment	Orientation	2465	2473	2480	3303	3315	3321
A-1	H_2	$\vec{k}\|\vec{c}$	-	-	-	1.00	-	-
A-1	H_2	$\vec{k}\perp\vec{c}$	-	-	-	0.80	-	0.85
C	D_2	$\vec{k}\|\vec{c}$	1.43	-	0.28	-	-	-
C	D_2	$\vec{k}\perp\vec{c}$	NA	NA	NA	-	-	-
A-2	H_2/D_2	$\vec{k}\|\vec{c}$	0.49*	0.45*	0.19*	0.97	0.89	-
A-2	H_2/D_2	$\vec{k}\perp\vec{c}$	0.38	0.43	0.53	0.46	0.88	0.29

Table 5.8: Measured intensities of the peaks shown in figures 5.11 and 5.14, calculated by fitting the data to a sum of Lorentzian functions. Data are normalized to the intensity of the 3303 cm^{-1} peak measured in the $\vec{k}\|\vec{c}$ direction on sample A-1 (values marked with * are also corrected for loss of intensity due to annealing). "-" denotes no observable peak, and *"NA"* denotes that spectroscopic data were not available, due to a strong electronic absorption.

5.7 The H-Y defect

Figure 5.16 shows a selected region of the IR absorption spectra recorded in the $\vec{k}||\vec{c}$ orientation for sample A-2 in the as-grown state and samples A-1, C and A-2 after annealing in H_2, D_2 and a mixture of H_2 and D_2 gas at 750 °C, respectively. The two IR absorption peaks at 2783 and 2106 cm^{-1}, assigned to the H-Y defect, are observed in the spectrum of sample A-2 after treatment in the H_2 and D_2 gas mixture. As described in section 5.6, IR absorption peaks originating from defects consisting of more than one O-H bond can be split by mixed H/D treatment, as the oscillator frequency of the O-H bonds will be influenced by a neighboring O-D bond. No additional peaks were observed near the 2106 and 2783 cm^{-1} lines, which strongly implies that this is not the case and that the absorbing defect contains only a single O-H bond.

These results are all in agreement with the findings of Li et al. [47], who previously have reported similar results in an IR absorption study of hydrothermally grown ZnO. The authors assigned the IR absorption line at 2783 cm^{-1} to a OH-Ni_{Zn} complex with a single O-H bond oriented at an angle of 108 ° to the c-axis, where H resides in the bond-centered configuration [47] (see section 3.6.3 for details).

The deuterium-related peak at 2106 cm^{-1} is also observed in sample C after D_2 treatment, in addition to a low intensity peak at 2783 cm^{-1}, presumably caused by H present in the as-grown sample. However, contrary to the findings of Li et al. [47], the 2783 cm^{-1} peak is not observed in sample A-1 after H_2 gas annealing.

5.7.1 Thermal stability

In order to study the annealing behavior of the 2783 and 2106 cm^{-1} lines, IR absorption spectra were recorded on sample A-2 after each step in a series of annealings at temperatures in the range from 500 to 800 °C. The annealings were performed in an open tubular furnace and the duration of each treatment was 30 min. The resulting spectra are shown in figure 5.18 and the normalized intensities of the lines as a function of annealing temperature are shown in figure 5.19. Note that already after annealing at 500 °C a significant decrease is observed in the peak intensities, and after 600 °C the peaks have completely disappeared. To extract an activation energy for the dissociation process, the data have been fitted to a model assuming first order dissociation kinetics, as presented in section 5.5.1. The model gives a reasonable fit to the data by using an activation energy for dissociation of E_a 2.7 eV and a preexponential factor of $c_0 = 9.9 \cdot 10^{12}$ s^{-1}.

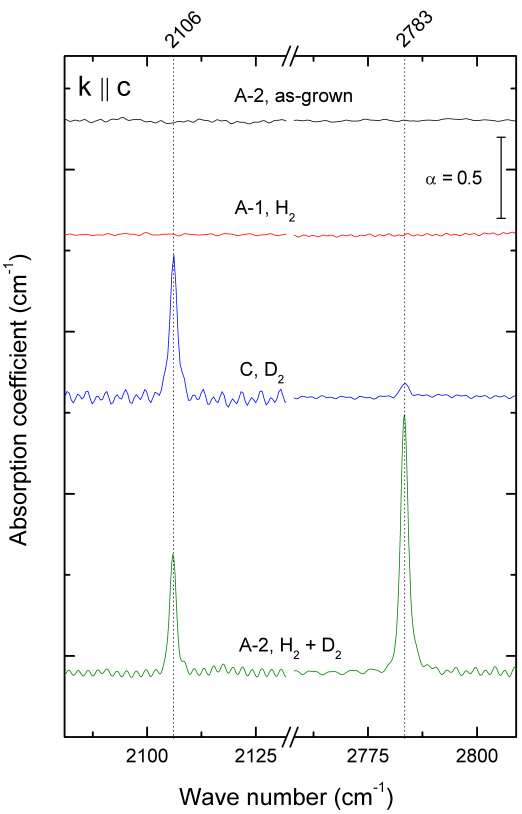

Figure 5.16: IR absorption spectra showing the peaks at 2783 and 2106 after various H_2 and/or D_2 gas anneals, measured in the $\vec{k}||\vec{c}$ orientation.

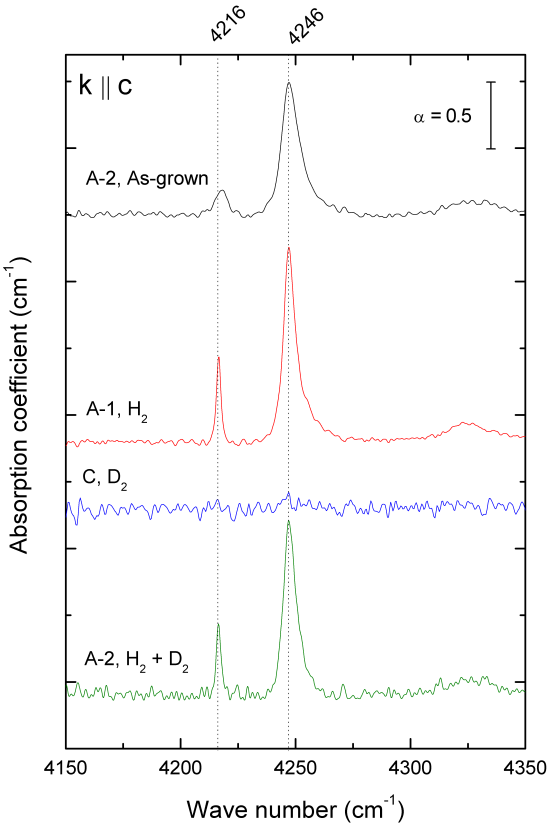

Figure 5.17: IR absorption spectra showing the Ni-related peaks near 4200 cm^{-1} after various H_2 and/or D_2 gas anneals, measured in the $\vec{k}||\vec{c}$ orientation.

These results are also in good agreement with those of Li et al. [47], who found that the absorption lines at 2783 and 2106 start to dissociate at 500 °C and completely disappear at 600 °C. Using the same dissociation model as described above, the authors arrive at an activation energy of dissociation of E_a = 2.8 eV, in close agreement with our value. The similarity of the calculated activation energies should however not be emphasized too much, as an insufficient number of measurements have been performed in this work to obtain enough statistical accuracy. More noteworthy is that the thermal behavior of the 2106 and 2783 cm^{-1} lines are almost identical, giving new strong indication that the two signals originate from the same defect.

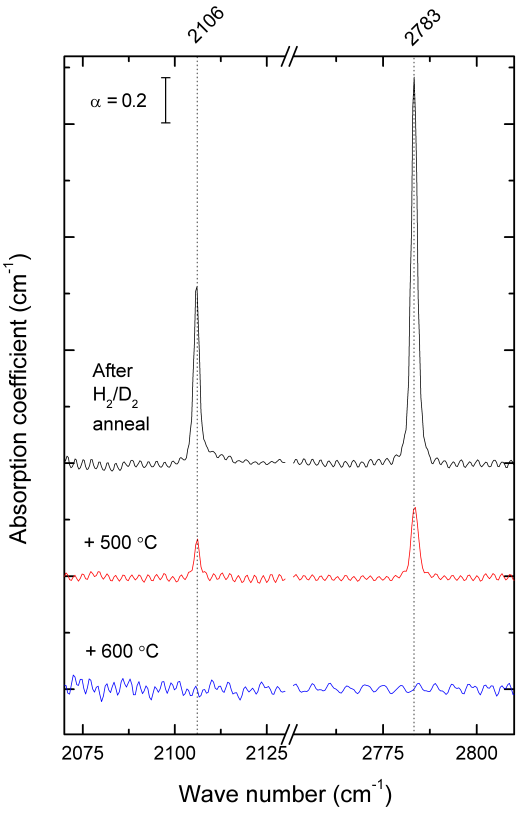

Figure 5.18: IR absorption spectra of sample A-2 showing the peaks at 2783 and 2106 cm^{-1} after mixed H_2/D_2 treatment (top) and subsequent 30 min annealings.

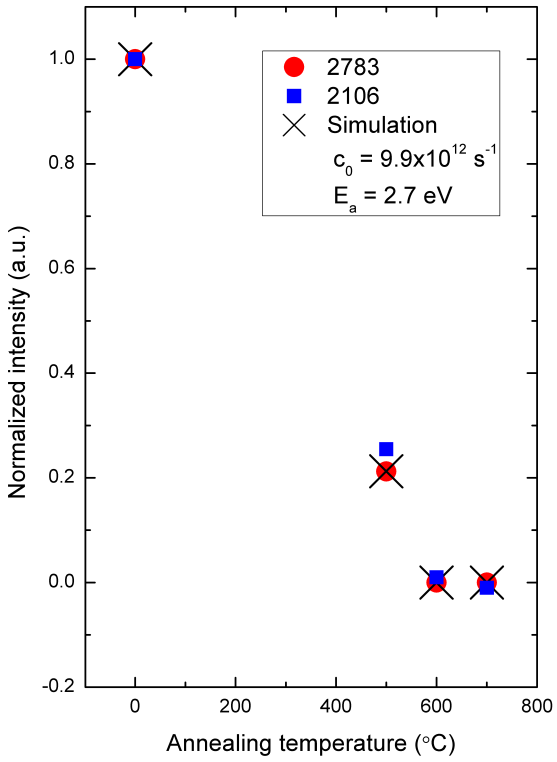

Figure 5.19: Normalized intensity of the peaks at 2783 and 2106 cm^{-1} as a function of annealing temperature for a series of isochronal anneals (30 min each). Crosses indicate a fit to a model assuming first order dissociation kinetics.

5.7.2 Molecular model

As described in section 3.6.3, the absorption lines at 2783 and 2106 cm^{-1} have previously been assigned to O-H and O-D stretch modes perturbed by a neighboring Ni atom on a substitutional Zn site. Several aspects of our results contradict this assignment. The H-Y signal were observed in the spectra of sample A-2 after annealing the sample in a mixed H_2/D_2 gas atmosphere, but was not observed in sample A-1 after a similar H_2 treatment. The two samples originate from the same wafer, and as seen in table 5.3 the intensity of the Ni-related absorption lines around 4200 cm^{-1} is comparable in the two samples before and after hydrogenation. The presence of strong Ni absorption lines in the spectra was used as an important argument in the original assignment of the 2783 cm^{-1} peak to a OH-Ni_{Zn} complex. Our results however indicate that there is no correlation between the Ni concentration and the presence of the 2783 cm^{-1} line after hydrogenation. Another counter-evidence of the assignment is the fact that a strong absorption from the O-D version of the defect is observed in sample C after D_2 gas annealing at 700 °C. As shown in figure 5.17, no Ni-related absorption lines are observed in this sample after the D_2 gas anneal. This is a further evidence that there is no correlation between the two signals. Instead, a variation in the hydrogenation conditions, e.g. via introduction of impurities, seems to cause the observed differences. Based on these results, the H-Y defect is tentatively assigned to single O-H stretch mode associated to an impurity introduced during annealing. This assignment is in agreement with the conclusion of Lavrov and Weber [73].

5.8 The H-Z defect

As shown in figure 5.20, six new peaks were observed in the course of the annealing series performed on sample A-2 after the mixed H_2 and D_2 treatment. Three of the peaks are O-H stretch modes, at 3347, 3361 and 3374 cm^{-1}, the other three are the O-D replica modes at 2485, 2495 and 2504 cm^{-1}. The frequency ratio between each pair of peaks is 1.347, close to the expected ratio between corresponding O-H/O-D modes, confirming that O-H bonds are involved in the absorbing defect.

These peaks have previously been studied in detail by Lavrov et al. [72] and were assigned to a defect complex involving two O-H bonds associated with a substitutional Cu atom (see section 3.6.3). The peaks at 3347 and 3374 cm^{-1} were shown to originate from the $(OH)_2$-Cu_{Zn} configuration of the defect, while 2485 and 2504 arise from the $(OD)_2$-Cu_{Zn} configuration. The 3361 and 2495 cm^{-1} lines are

found midway between each of these pairs, and arise from the O-H and O-D mode of the mixed (OH)-(OD)-Cu_{Zn} complex, respectively.

All the 6 peaks show similar annealing dependencies, appearing in the spectra after annealing at 600 °C and vanishing after annealing at 900 °C. A similar behavior was also found for the $(OH)_2$-Cu_{Zn} lines during the annealing study of sample B-1, described in section 5.4.1. As seen in figure 5.6, the peaks at 3347 and 3374 cm^{-1} appear in the spectra after annealing at 500 °C. The peaks are still observable after the annealings at 600 and 700 °C, before disappearing after 800 °C. This annealing behavior is consistent with the findings of Lavrov et al. [72], who found that the annealing dependency of the $(OH)_2$ Cu_{Zn} complex is not monotonous, regaining intensity after annealing at higher temperatures (see section 3.6.3 for details). A process similar to what has been suggested for the OH-Li defect, involving continuous dissociation and recapture of H, may explain the observed results.

An absorption line at 5781 cm^{-1}, assigned to electronic transitions in substitutional Cu impurities [50], and a line at 3192 cm^{-1}, assigned to a single O-H bond associated with a Cu atom [71] were also observed in the samples of Lavrov et al. [72]. Both signals were reported to have high intensities, with the OH-Cu_{Zn} signal at 3192 cm^{-1} being $\sim$ 50 times stronger than the 3347 and 3374 cm^{-1} lines. However, none of these signals have been observed at any stage in this work. In addition, no Cu signal was observed in the SIMS mass spectra of the as-grown samples. If Cu are present in the samples, it must therefore have been introduced as a contamination during annealing. The absence of any other Cu-related signal in the IR spectra and SIMS data is puzzling, questioning the assignment by Lavrov et al. [72] of the 3347 and 3374 cm^{-1} LVMs to a $(OH)_2$-Cu_{Zn} complex. The possibility that another impurity atom is involved should therefore be considered.

5.9 Summary of H-related LVMs

A list of the main H-related LVMs observed in this work is summarized in table 5.9. As described in section 2.2.6, the frequency ratio between the O-H and O-D stretch modes $R \equiv \frac{\tilde{\nu}_H}{\tilde{\nu}_D}$ should be equal to $\sqrt{\frac{\mu_H}{\mu_D}} = 1.374$ in the harmonic approximation. The observed deviations from the expected frequency shift is related to the anharmonicity of the vibrational potential. As described in section 2.2.7, the anharmonic potential is characterized by a harmonic wavenumber $\tilde{\nu}_e$ and an anharmonicity constant χ_e [10]. The observed O-H and O-D wavenumbers, the

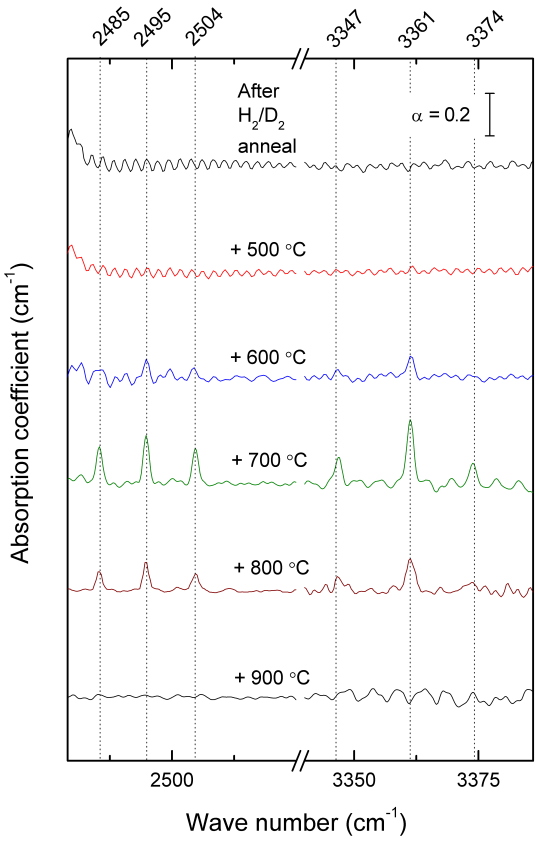

Figure 5.20: IR absorption spectra of sample A-2 in the $\vec{k}\|\vec{c}$ orientation, showing new peaks at 2485, 2495, 2504, 3347, 3361 and 3374 cm^{-1} emerging after H_2/D_2 treatment and subsequent annealing at 600 °C.

experimental frequency shift R and corresponding values for $\tilde{\nu}_e$ and χ_e for the observed LVMs are also presented in table 5.9. Note that the harmonic wavenumber for all the LVMs are found in the range 3600-3900 cm^{-1}, close to the value of 3748 cm^{-1} calculated for the harmonic O-H stretch mode, except for the H-Y LVM which is ~ 500 cm^{-1} lower. This mode also has a higher degree of anharmonicity.

Based on the integrated intensity of the absorption lines related to these defects (table 5.1), the previously reported absorption cross sections (table 5.6) and eq. 5.6 it is possible to estimate the concentration of the H-related defects presented in this work. However, many of the involved O-H/O-D bonds are oriented at an unknown angle to the c-axis, reducing the apparent concentration of absorbers. Also, the intensities of the absorption lines vary in the different samples after hydrogenation and the correct values for ϵ_{OH} and ϵ_{OD} are not known. The calculated concentrations should therefore be considered as a rough estimation. By using the value for $\epsilon_{OH}/\epsilon_{OD}$ calculated for the free O-H_{BC} donor in ZnO [55] the concentration of H-X, H-Y and H-Z complexes after hydrogenation is calculated to be $\sim 2-4\cdot 10^{17}$, $\sim 1-2\cdot 10^{17}$ and $\sim 5\cdot 10^{16}$ cm^{-3}, respectively. The concentration of the (H-related) defect responsible for the 3336 cm^{-1} line in the as-grown samples is estimated to be $\sim 6\cdot 10^{16}$ cm^{-3} in wafer B, which is comparable to the as-grown concentration of OH-Li complexes ($\sim 7\cdot 10^{16}$ cm^{-3}) calculated in section 5.5.2.

Assignment	$\tilde{\nu}_{OH}$ (cm^{-1})	$\tilde{\nu}_{OD}$ (cm^{-1})	$R \equiv \frac{\tilde{\nu}_H}{\tilde{\nu}_D}$	χ_e	$\tilde{\nu}_e$ (cm^{-1})	Previously reported in
H-Y	2783	2106	1.322	0.064	3190	[47]
?	3279	-	-	-	-	-
H-X[3]	3303	2465	1.340	0.043	3614	-
H-X[3]	3321	2480	1.339	0.044	3642	-
?	3336	-	-	-	-	[46]
H-Z[3]	3347	2485	1.347	0.035	3600	[72]
H-Z[3]	3374	2505	1.347	0.038	3625	[72]
?	3483	-	-	-	-	[46]
?	3516	-	-	-	-	[46]
OH-Li_{Zn}	3577	2644	1.353	0.028	3787	[64, 11]

Table 5.9: List of the H-related LVMs in ZnO presented in this work. The isotopic shift R, the harmonic wave number $\tilde{\nu}_e$ and the anharmonicity parameter χ_e are indicated.

[3]For defect complexes consisting of more than one O-H bond eqs. 2.17 and 2.18 are not directly applicable, caused by additional coupling between the vibrational modes. The calculated values for the H-X and H-Z defects is therefore less profound than those found for the OH-Li and H-Y defects. For a more comprehensive discussion of this subject, see ref. [72].

5.10 Electrical effects of hydrogenation

5.10.1 Resistivity measurements

Table 5.10 lists the resistivity of the different samples in the as-grown state and after hydrogenation and subsequent annealing steps. The resistivity decreases over four orders of magnitude as a result of the hydrogenation to $0.17 - 0.38\ \Omega cm$, depending on the sample. Assuming a room temperature mobility of 100 cm^2/Vs, previously reported [89] in similar samples as in this thesis, the electron concentration n can be estimated from eq. 4.17 to be $n = 1.6 - 3.7 \cdot 10^{17}$ cm^{-3}. Previously, Jokela and McCluskey [90] have measured an electron concentration of $4.7 \cdot 10^{17} cm^{-3}$ in ZnO crystals grown by the vapor phase method and annealed in H_2 gas at 710 °C for 10 h, in the same range as our results. However, their increased carrier density was not stable in room temperature, with a significant drop observed after a few days. Contrary to this, the low resistivity measured in sample A-1 after the H_2 anneal is stable even after annealing at 200 °C for 30 min. The excess carrier concentration in the work of Jokela and McCluskey [90] were attributed to an unstable shallow H donor. The results in table 5.10 suggest that a different mechanism is responsible in the samples used in this work. The discrepancy may be related to difference in growth technique and impurity concentration.

As shown in table 5.10, the low resistivity of sample A-2 after hydrogenation is not stable against annealing at higher temperatures, returning to nearly half its original value after annealing at 800 °C.

5.10.2 Free electron absorption

The increased electron concentration after the hydrogenations are also observed in the IR absorption spectra. As described in section 2.2.8, free electrons present in the sample give rise to a strong background absorption which increases with decreasing wavenumber. Also, the free electron absorption has been found to be proportional to the electron concentration n [91]. Figure 5.21 shows IR absorption spectra of sample A-2 after H_2/D_2 anneal and subsequent annealing steps. Contrary to the other spectra presented in this thesis, the baseline of the spectra are not subtracted, showing how the electron density at the measurement temperature decreases as the sample is annealed at 500 and 600 °C. According to theory, the wave number dependency of the absorption coefficient is expected to be of the form $\alpha(\tilde{\nu}) = k \cdot \tilde{\nu}^{-p}$, where the exponent p is dependent on the dominant scattering mechanism in the material. A least-squares fit of the data to such a function has

Sample	Treatment	Resistivity (Ωcm)	Standard deviation (Ωcm)
A-1	As-grown	5400	110
B-2	As-grown	420	1.3
A-1	H_2 anneal	0.38	$1.1 \cdot 10^{-2}$
A-1	+ 100 °C, 30 min	0.35	$6.0 \cdot 10^{-3}$
A-1	+ 200 °C, 30 min	0.33	$2.1 \cdot 10^{-2}$
A-2	H_2/D_2 anneal	0.17	$1.4 \cdot 10^{-3}$
A-2	+ 600 °C, 30 min	486	1.1
A-2	+ 700 °C, 30 min	1680	8.3
A-2	+ 800 °C, 30 min	2390	4.2
C	As-grown	Data not available	
C	D_2 anneal	0.27	$3.2 \cdot 10^{-2}$

Table 5.10: Measured resistivities on different samples before and after H_2 and/or D_2 gas anneals. Several measurements were averaged to obtain a better statistical accuracy, and the standard deviations are also indicated.

been performed, shown as dashed lines in figure 5.21, and some values for the exponent p are presented in table 5.11. The fit yields values for p between 2 and 2.5, which is expected for free-carrier absorption from electrons scattered by phonons [91]. Schifano et al. [89] have previously found the electronic conductivity in similar, as-grown samples are dominated by ionized impurity scattering at temperatures below $\sim$ 250 °C. Hence, this indicates that the hydrogenation procedure reduces the concentration of charged impurities in the samples (e.g. by passivation of acceptors) rather than introducing new, ionized donors.

Shi et al. [74] have reported a relation between the absorption coefficient at 2000 cm^{-1} $\alpha(2000\,cm^{-1})$ and the carrier density n, given as

$$n = 9.3 \cdot 10^{15} \cdot \alpha(2000\,cm^{-1})\ cm^{-2}. \tag{5.9}$$

The absorption coefficient at 2000 cm^{-1} and calculated values for the electron concentration at $\sim$ 20 K in the three hydrogenated samples A-1, A-2 and C are given in table 5.11. Note that this calibration is dependent on several factors such as the electron mobility [91], and may therefore not give an entirely correct estimate. Electron concentrations in the 10^{17} cm^{-3} range can however safely be assumed, indicating that a similar concentration of shallow donor states, not freezing out at 20 K, exist in the samples.

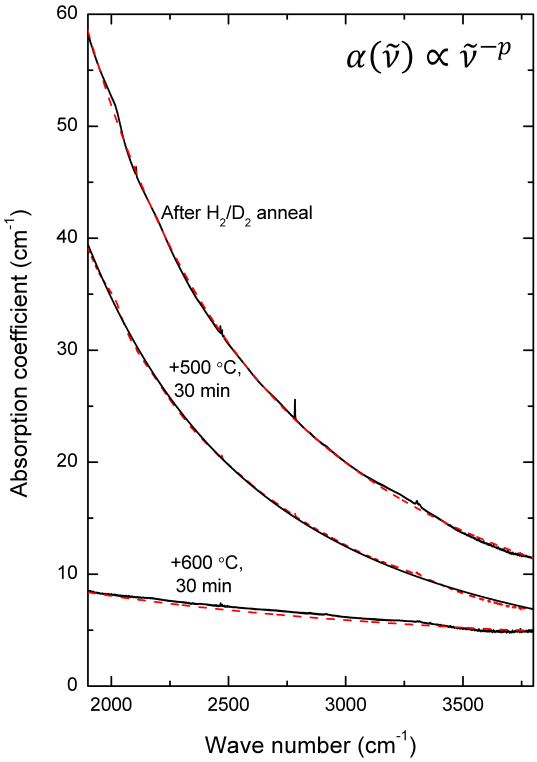

Figure 5.21: IR absorption spectra measured in the $\vec{k}||\vec{c}$ orientation on sample A-2 after hydrogenation and subsequent annealings, with a baseline arising from free electron absorption. The dashed lines shows a least squares fit of the data to a function of the form $\alpha(\tilde{\nu}) = k \cdot \tilde{\nu}^{-p}$

Sample	Treatment	$\alpha(2000\,cm^{-1})$ (cm^{-1})	n (cm^{-3})	p (in $\alpha(\tilde{\nu}) = k \cdot \tilde{\nu}^{-p}$)
A-1	H_2	29.50	$2.7 \cdot 10^{17}$	2.00
A-2	H_2/D_2	51.85	$4.7 \cdot 10^{17}$	2.36
C	D_2	27.50	$2.5 \cdot 10^{17}$	2.84

Table 5.11: (Baseline) absorption coefficient at 2000 cm^{-1} $\alpha(2000\,cm^{-1})$ and electron concentrations n for three different samples after hydrogenation, calculated from eq. 5.9. The exponent in the dependency of $\alpha(\tilde{\nu})$ on wave number is also indicated.

5.10.3 The role of hydrogen

Note that the reported IR absorption line at 3611 cm^{-1} associated to an unassociated H donor [55] is not observed at any stage of this work. The samples contain several impurities in the 10^{17} cm^{-3} range [42], similar to the H solubility during hydrogenation [7]. In addition, H is known to readily react with other defects and impurities [5]. Hence, it is reasonable to assume that H mainly resides in such complexes in our samples. The enhanced electron concentration after hydrogenations may therefore originate from stable H complexes acting as donors, H electrically neutralizing acceptors by passivation or (most likely) a combination of the two.

Annealing of ZnO in reducing atmospheres like H_2 has been shown to result in a preferential loss of oxygen [81]. The oxygen vacancy, V_O, has a low formation energy [37] and should therefore occur in large concentrations. With the simultaneous in-diffusion of H the H_O defect (described in section 3.6.2) may therefore be created. This defect is predicted to be a shallow donor, and may explain the observed drop in resistivity after hydrogenation (table 5.10). In contrast to the unassociated H_i donor, the H_O defect is reported to be stable up to 500 °C. This is consistent with the fact that the resistivity was found to be stable after annealing at 200 °C but increased after annealing at 500 °C and higher.

Alternatively, the electrical effect of hydrogenation is caused by H compensating acceptors in the samples. In contrast to the H_O defect, these complexes may be observed in the IR spectra. The formation of the previously mentioned H-X and H-Y complexes in the hydrogenated samples may have such an effect. However, the available amount of data is not sufficient to draw any conclusions on this subject. Nevertheless, it is interesting to notice that both defects anneal out around 500 - 600 °C, in the same temperature range where the carrier density rapidly decreases (see table 5.10 and figure 5.21).

On the other hand, Li is known to act as an important compensating acceptor in ZnO, and has been found to occur almost exclusively in the Li_{Zn}^{-} acceptor configuration in n-type material [42]. The increased number of Li acceptors bound up in the neutral OH-Li complex after hydrogenation (see table 5.1) is therefore expected to lower the acceptor concentration and thus decrease the resistivity, as observed. As a thought experiment, the absorption cross section for the OH-Li defect calculated in section 5.5.2 is assumed to be correct, so that all Li ions in the sample are associated to H after the H_2 anneal. Furthermore, the observed effect on the electrical conductivity of the sample after hydrogenation is assumed

to be entirely caused by hydrogen passivating Li acceptors. The change in electron concentration n after hydrogenation then equals the change in the concentration of the OH-Li complex:

$$n_{II} - n_I = [OH - Li]_{II} - [OH - Li]_I. \tag{5.10}$$

Here, the subscripts $_I$ and $_{II}$ have been used to denote the quantities in the as-grown state and after hydrogenation, respectively.

The electron concentration can be related to the measured resistivity ρ through the relation

$$\frac{1}{\rho} = nq\mu. \tag{5.11}$$

By combining eqs. 5.10 and 5.11, we get

$$n_{II} - n_I = \frac{1}{\rho_I q \mu_{II}} - \frac{1}{\rho_{II} q \mu_I} = [OH - Li]_{II} - [OH - Li]_I. \tag{5.12}$$

Because ρ_I is $\sim$ 4 orders of magnitude larger than ρ_{II} the second term on the left side of eq. 5.12 can be omitted without introducing any significant error. It is now possible to rearrange for the only unknown quantity, namely the electron mobility after hydrogenation:

$$\begin{aligned} \mu_{II} &= (\rho_{II} q([OH - Li]_{II} - [OH - Li]_I)^{-1} \\ &= (0.38\ \Omega cm \cdot 1.602 \cdot 10^{-19}\ C \cdot (2 \cdot 10^{17}\ cm^{-3} - 1.36310^{17}\ cm^{-3}))^{-1} \\ &= 258 cm^2/Vs. \end{aligned} \tag{5.13}$$

This value is in agreement with the Hall mobilities measured by Seager and Myers [60] on hydrothermal samples after similar hydrogen treatment.

Even if the increased carrier density after hydrogenation can be explained entirely by passivation of Li acceptors, this is probably not the complete picture. Other acceptors than Li are also present in the samples [89], and H-related donor states may also play a significant role. A more comprehensive study is needed to examine possible correlations between the H-related IR absorption signals and the carrier density in ZnO samples. Some future experiments are suggested in section 6.2.

Chapter 6

Summary

6.1 Conclusion

Hydrothermally (HT) grown ZnO single crystals have been investigated by FTIR, SIMS and four point resistivity measurements. The samples have been studied both in the as-grown state and after treatment in H_2 and/or D_2 atmosphere at temperatures between 700 and 750 °C, leading to in-diffusion of H/D.

A strong absorption line at 3577 cm^{-1}, previously assigned to the LVM of a OH-Li complex [11], dominates the IR spectra of the as-grown samples. The integrated intensity of the 3577 cm^{-1} line was found to vary between 1.5 and 2.5 cm^{-2} after annealing in the temperature range from 100 to 1250 °C, before the LVM disappeared after annealing at 1300 °C. This annealing dependency could not be explained by an irreversible, first order dissociation model, indicating that the thermal stability of the OH-Li LVM is controlled by a complex process involving dissociation, diffusion and recapture of H. The absorption cross section for the 3577 cm^{-1} line has been estimated to be $\epsilon_{OH} \geq 1.27 \cdot 10^{-17}$ cm, giving an OH-Li concentration of $[OH - Li] \leq 1.4 \cdot 10^{17}$ cm^{-3} in the as-grown samples.

Not previously reported absorption lines at 3303 and 3321 cm^{-1} have been observed in both as-grown and hydrogenated samples. These lines are assigned to LVMs of a defect complex labeled H-X, consisting of two O-H bonds associated to an unknown impurity atom. The 3321 cm^{-1} mode is oriented along the c-axis of the sample, while the 3303 cm^{-1} mode is oriented at an angle with the c-axis. The defect anneals out at $\approx$ 600 °C, consistent with an activation energy for dissociation of 2.8 eV.

The absorption line at 2783 cm^{-1}, labeled H-Y, has also been observed in hydrogenated samples. This line has previously been assigned to the LVM of an

OH-Ni_{Zn} complex [47]. However, no correlation has been found between the presence of this line and the Ni concentration in the samples, suggesting that the original assignment should be revisited. Instead, the 2783 cm^{-1} line is assigned to a single O-H bond associated to an impurity atom introduced during annealing. The complex was found to anneal out at $\approx$ 500 °C, with an activation energy for dissociation of 2.7 eV.

The H-Z defect, consisting of two O-H bonds with LVM frequencies of 3347 and 3374 cm^{-1}, have been observed in both as-grown and hydrogenated samples after annealing at moderate temperatures (500-800 °C). The previous assignment [72] of these lines to a $(OH)_2$-Cu_{Zn} defect is questioned, based on the lack of other Cu-related signals in the IR absorption and SIMS data.

A group of absorption lines at 4216, 4240 and 4246 cm^{-1} have been related to the Ni concentration measured by SIMS, supporting the previous assignment of these lines to internal electronic transitions of substitutional Ni^0_{Zn} impurities [24]. The absorption cross section for the lines have been found to be $\epsilon_{Ni} \geq 2.91 \cdot 10^{-17}$ cm.

Finally, a drop of 4 orders of magnitude was observed in the resistivity of the samples after hydrogenation. The increased carrier density was found to be stable against annealing at 200 °C, but decreased after annealing at higher temperatures, regaining almost half its original value after 800 °C. Donor activity from stable H donors species like H_O and/or H passivation of compensating acceptors like Li_{Zn} may account for the observed results.

6.2 Suggestions for further work

On the instrumentation side, an operational temperature controller should be installed in the cryogenic cooling system to obtain a better control of the sample temperature during the FTIR measurements. This would also enable measurements of IR peak positions and widths as a function of sample temperature, which may be used to obtain a further understanding of the microstrucure of the observed H-related defects.

In addition, a wire-grid polarizer may be implemented in the IR beam line, enabling measurements of the polarization dependency of the observed IR absorption lines, which may be used for determination of O-H bond angles. To our knowledge, such results are not previously reported for i.e. the 3303 and 3336 cm^{-1} LVMs.

The nature of the species involved in the defects labeled H-X and H-Y observed

after hydrogen in-diffusion is still not clarified. It would therefore be interesting to record SIMS mass spectra on the hydrogenated samples and compare those with the ones recorded in the as-grown state to unveil impurities introduced during hydrogenation. Particularly, the possibility of Cu contamination during annealing should be examined to investigate the validity of the assignment of the H-Z defect to a $(OH)_2$-Cu_{Zn} complex.

To obtain a more precise determination of the dissociation kinetics of the H-X and H-Z defects, isothermal annealing studies should be performed. The choice of annealing temperature(s) may be based on the isochronal annealing studies presented in this work.

A more thorough study of the annealing dependency of the carrier concentration after hydrogenation should also be performed. Preferably, temperature dependent Hall effect studies should be employed, but four point resistivity measurements may also be used. Such an experiment may give a further understanding of the electrical properties of H in HT ZnO, including both its donor activity and ability to passivate acceptors. In addition, a good calibration of free electron absorption versus carrier concentration should be performed. FTIR measurements may then also be used as a simple, contact-free and non-destructive method for measuring carrier concentrations at various temperatures.

According to the findings of Lavrov et al. [55], a substantial concentration of H_O donors is only formed in a region down to $\sim$ 10 μm from the sample surface after in-diffusion of hydrogen from the gas phase. The effect of H_O on the measured resistivity may therefore possibly be determined by measuring the sample resistivity before and after grinding/polishing this region away.

The thermal stability of the OH-Li complex has been found to be different from sample to sample, and may also be influenced by the H_2 gas anneals. It would therefore be interesting to repeat the experiment of measuring the 3577 cm^{-1} line intensity as a function of annealing temperature on a hydrogenated sample. This may also be used to examine possible correlations between the 3577 cm^{-1} line and the resistivity, presumably resulting in a further understanding of H passivation of Li acceptors.

Appendix

A.1 IR peak intensities

Table A.1 lists all the measured IR absorption peak intensities presented in this work, given as integrated absorption coefficients. The integration was performed by manually defining a point at the baseline on each side of the peak, drawing a straight line between these two points and calculating the area enclosed by the line and the data points above it. By doing the calculation in this manner, the integration is almost insensitive to changes in the baseline of the spectrum.

A.2 Temperature profile for RTP treatment

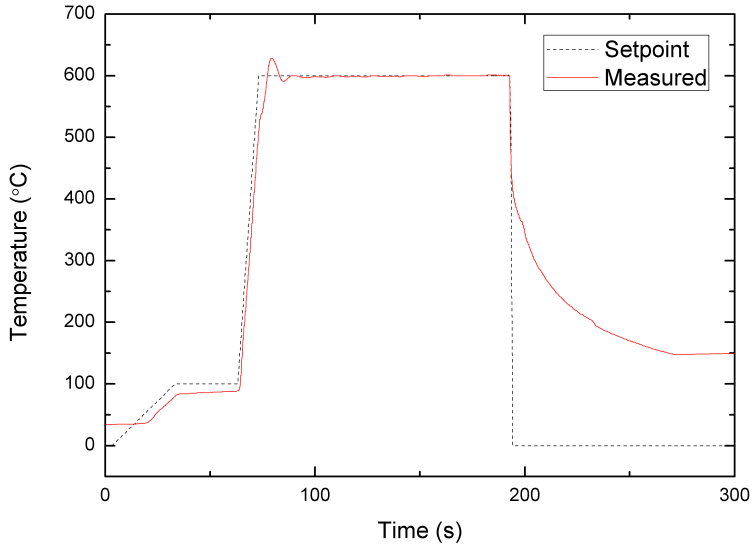

Figure A.1: Temperature profile used for the 2 min RTP treatment of sample D, described in section 5.5.1.

Measurement			Absorption peaks (cm^{-2})																		
Sample	Treatment	Orientation	O-D LVMs						O-H LVMs											Ni^{2+}-transitions	
			2106	**2465+**[a]	**2485**	**2495**	**2504**	**2644**	**2783**	**3279**	**3303+**[b]	**3321**	**3336**	**3347**	**3361**	**3374**	**3483**	**3516**	**3577**	**4216**	**4240/4246**
A-1	H_2	$\vec{k}\perp\vec{c}$	NA	NA	NA	NA	NA	NA	-	-	0.99	1.04	-	-	-	-	-	-	2.54	0.73	13.14
A-1	H_2	$\vec{k}\parallel\vec{c}$	-	-	-	-	-	-	-	S	2.59	-	-	S	-	-	-	-	-	1.65	10.60
A-1	H_2 + 100 °C	$\vec{k}\parallel\vec{c}$	-	-	-	-	-	-	-	S	2.57	-	-	-	-	-	-	-	-	0.98	8.61
A-1	H_2 + 200 °C	$\vec{k}\parallel\vec{c}$	-	-	-	-	-	-	-	S	2.34	-	-	-	-	-	-	-	-	0.81	8.55
A-2	As-grown	$\vec{k}\perp\vec{c}$	-	-	-	-	-	-	-	S	-	-	0.16	-	-	-	S	S	1.73	0.54	10.93
A-2	As-grown	$\vec{k}\parallel\vec{c}$	-	-	-	-	-	-	-	-	-	-	0.33	-	-	-	-	-	-	1.30	9.45
A-2	H_2/D_2	$\vec{k}\perp\vec{c}$	NA	NA	NA	NA	NA	NA	NA	-	3.35	-	-	-	-	-	-	-	1.79	0.66	11.17
A-2	H_2/D_2	$\vec{k}\parallel\vec{c}$	1.52	3.07	-	-	-	-	3.73	-	4.44	-	-	-	-	-	-	-	-	1.35	9.55
A-2	H_2/D_2 + 500 °C	$\vec{k}\parallel\vec{c}$	0.39	2.18	-	-	-	-	0.79	-	2.86	-	-	-	-	-	-	-	-	1.05	9.01
A-2	H_2/D_2 + 600 °C	$\vec{k}\parallel\vec{c}$	-	0.77	S	S	S	-	-	-	0.93	-	-	S	S	S	-	-	-	1.19	9.25
A-2	H_2/D_2 + 700 °C	$\vec{k}\parallel\vec{c}$	-	0.32	0.27	0.30	0.26	-	-	-	0.20	-	-	0.27	0.48	0.21	-	-	-	1.54	10.58
A-2	H_2/D_2 + 800 °C	$\vec{k}\parallel\vec{c}$	-	0.14	0.11	0.18	0.13	-	-	-	-	-	-	S	0.29	S	-	-	-	0.91	10.25
A-2	H_2/D_2 + 800 °C	$\vec{k}\perp\vec{c}$	-	0.33	S	S	S	0.25	-	-	S	S	-	0.11	0.21	0.10	-	-	0.29	0.73	11.25
A-2	H_2/D_2 + 900 °C	$\vec{k}\parallel\vec{c}$	-	-	-	-	-	-	-	-	-	-	-	-	-	-	-	-	-	1.11	9.95
A-2	H_2/D_2 + 900 °C	$\vec{k}\perp\vec{c}$	-					0.11	-	-			-	0.11			-	-	0.73	0.79	12.90
B-1	As-grown	$\vec{k}\parallel\vec{c}$	-	-	-	-	-	-	-	-	-	-	1.55	-	-	-	-	-	-	0.14	0.87
B-1	As-grown	$\vec{k}\perp\vec{c}$	-	-	-	-	-	-	-	S	-	-	0.64	-	-	-	0.49	0.25	1.72	0.10	1.43
B-1	100 °C	$\vec{k}\perp\vec{c}$	-	-	-	-	-	-	-	S	-	-	0.42	-	-	-	0.25	0.18	2.49	0.12	1.04
B-1	100 °C	$\vec{k}\perp\vec{c}$	-	-	-	-	-	-	-	S	-	-	0.12	-	-	-	0.08	0.07	2.12	S	1.21
B-1	200 °C	$\vec{k}\perp\vec{c}$	-	-	-	-	-	-	-	S	-	-	0.16	-	-	-	0.11	0.07	2.27	S	1.32
B-1	250 °C	$\vec{k}\perp\vec{c}$	-	-	-	-	-	-	-	S	-	-	0.28	-	-	-	0.21	0.15	2.49	S	1.26
B-1	250 °C + RT	$\vec{k}\perp\vec{c}$	-	-	-	-	-	-	-	S	-	-	S	-	-	-	S	S	2.06	S	1.08
B-1	500 °C	$\vec{k}\perp\vec{c}$	-	-	-	-	-	-	-	0.22	1.14	0.67	0.11	0.12	-	0.17	0.10	-	2.11	S	1.23
B-1	600 °C	$\vec{k}\perp\vec{c}$	-	-	-	-	-	-	-	S	0.24	S	-	S	-	S	-	-	1.52	S	1.22
B-1	700 °C	$\vec{k}\perp\vec{c}$	-	-	-	-	-	-	-	S	0.53	0.32	-	S	-	S	-	-	1.76	S	1.1
B-1	800 °C	$\vec{k}\perp\vec{c}$	-	-	-	-	-	-	-	-	-	-	-	-	-	-	-	-	1.63	P	1.2
B-1	900 °C	$\vec{k}\perp\vec{c}$	-	-	-	-	-	-	-	-	-	-	-	-	-	-	-	-	1.73	P	0.9
B-1	1000 °C	$\vec{k}\perp\vec{c}$	-	-	-	-	-	-	-	-	-	-	-	-	-	-	-	-	2.00	P	1.0
B-1	1100 °C	$\vec{k}\perp\vec{c}$	-	-	-	-	-	-	-	-	-	-	-	-	-	-	-	-	1.85	P	1.3
B-1	1150 °C	$\vec{k}\perp\vec{c}$	-	-	-	-	-	-	-	-	-	-	-	-	-	-	-	-	1.70	P	1.1
B-1	1200 °C	$\vec{k}\perp\vec{c}$	-	-	-	-	-	-	-	-	-	-	-	-	-	-	-	-	1.90	P	P
B-1	1250 °C	$\vec{k}\perp\vec{c}$	-	-	-	-	-	-	-	-	-	-	-	-	-	-	-	-	2.24	P	P
B-1	1300 °C	$\vec{k}\perp\vec{c}$	-	-	-	-	-	-	-	-	-	-	-	-	-	-	-	-	-	P	P
C	D_2	$\vec{k}\perp\vec{c}$	NA	NA	NA	NA	NA	1.0	-	-	-	-	-	-	-	-	-	-	-	P	P
C	D_2	$\vec{k}\parallel\vec{c}$	2.01	6.00	-	-	-	-	0.18	-	-	-	-	-	-	-	-	-	-	P	P
D	As-grown	$\vec{k}\perp\vec{c}$	-	-	-	-	-	-	-	S	-	-	-	-	-	-	-	-	1.90	0.09	1.07
D	RTP, 600 °C, 2 min	$\vec{k}\perp\vec{c}$	-	-	-	-	-	-	-	S	0.15	0.12	-	-	-	-	-	-	1.91	0.06	0.95
D	RTP, 600 °C, 10 min	$\vec{k}\perp\vec{c}$	-	-	-	-	-	-	-	S	0.25	0.18	-	S	-	S	-	-	1.49	0.06	1.07

Table A.1: List of all the IR peak intensities reported in this work, given by their integrated absorption coefficients. "-" denotes no observable peak. *"S"* denotes a small peak, so that the intensity could not be accurately determined. *P* denotes that a peak of the expected intensity is observed, but that the integrated absorbance could not be determined due to a low signal-to-noise ratio. Finally, *"NA"* denotes that spectroscopic data were not available in the relevant region, e.g. due to to much electronic absorption.

[a] Given as the total integrated area under the 2461, 2465, 2473 and 2480 cm^{-1} peaks.

[b] In the cases where the peak is split into two components, the total area under the 3303 and 3315 cm^{-1} peaks is given.

A.3 Derivation of Morse-potential parameters

In section 5.9, eqs. 2.17 and 2.18 were used to relate the anharmonic parameters $\tilde{\nu}_e$ and χ_e to the measured isotope shifts of O-H stretch modes. In this section a derivation of the equations will be given, as treated by Wöhlecke and Kovács [10]:

To describe the real behavior of chemical bonds, an anharmonic potential has to be assumed. A commonly used anharmonic potential for which the Schroedinger equation have an exact solution is the Morse-potential [92]:

$$U(r - r_e) = D_e(1 - e^{-\beta(r-r_e)})^2, \tag{A.1}$$

where r_e is the equilibrium distance, and D_e (the binding energy) and β are constants. This potential gives the solution for the vibrational energies as

$$E_{vib}(n) = \hbar\omega_e[(n + \frac{1}{2}) - \chi_e(n + \frac{1}{2})^2], \tag{A.2}$$

where ω_e is the harmonic frequency, χ_e is a dimensionless anharmonicity constant and n is an non-negative integer. ω_e and χ_e may be expressed by the Morse-potential parameters as

$$\omega_e = \beta\sqrt{\frac{\hbar D_e}{\pi c\mu}} \tag{A.3}$$

$$\chi_e = \frac{\beta}{4}\sqrt{\frac{\hbar}{\pi c\mu D_e}}. \tag{A.4}$$

Here, μ is the reduced mass of the molecule. In terms of wave numbers, eq. A.2 may be written:

$$G(n) = \tilde{\nu}_e(n + \frac{1}{2}) - \tilde{\nu}_e\chi_e(n + \frac{1}{2})^2. \tag{A.5}$$

The $n = 0 \rightarrow 1$ transition will be the primary allowed transition between these states, and can be written as:

$$\tilde{\nu}_0^H = \Delta G_{01} = G(1) - G(0) = \tilde{\nu}_e^H(1 - 2\chi_e). \tag{A.6}$$

Here, the superscript H indicates that the corresponding expression of the OH^- molecule is used. Since isotopic molecules have the same electronic structure, the general shape of the potential has to be the same for OH^- and OD^- molecules. Thus the solution for the energies of the O-D bond can be obtained by rewriting eq. A.5

and introducing $\eta^{-1} = \sqrt{\frac{\mu_H}{\mu_D}}$, where μ_H and μ_D are the reduced masses of the free O-H and O-D bonds, respectively:

$$G_D(n) = \eta\tilde{\nu}_e^H(n+\frac{1}{2}) - \eta^2\tilde{\nu}_e^H\chi_e(n+\frac{1}{2})^2. \tag{A.7}$$

The first fundamental transition $n = 0 \rightarrow 1$ of the OD^- molecule will be given as

$$\tilde{\nu}_{0,D} = \Delta G_{D,01} = G_D(1) - G_D(0) = \eta\tilde{\nu}_e^H - 2\eta^2\tilde{\nu}_e^H\chi_e. \tag{A.8}$$

Introducing R as the ratio of the fundamental vibrational transitions of the OH^- and OD^- molecules, $R = \frac{\tilde{\nu}_0^H}{\tilde{\nu}_0^D}$, the anharmonic parameter χ_e can be expressed as a function of η and R

$$\chi_e = \frac{1 - R\eta}{2(1 - R\eta^2)}. \tag{A.9}$$

The harmonic wavenumber ${\tilde{\nu}_e}^H$ can then be obtained from eq. A.6:

$$\tilde{\nu}_e^H = \frac{\tilde{\nu}_0^H}{1 - 2\chi_e} \tag{A.10}$$

A.4 Peak analysis

As a good approximation, IR absorption peaks may normally be represented by a Lorentzian function [93], expressed by:

$$y(x) = y_0 + \frac{2A}{\pi}\frac{w}{4(x - x_c)^2 + w^2}, \tag{A.11}$$

where A is the area under the peak, w is the full width at half height (FWHH) and $(x_c, y_c) = (x_c, y_0 + \frac{2A}{w\pi})$ is the point of maximum intensity. To separate overlapping peaks occurring in this work, the spectroscopic data was fitted to a sum of such functions using a least-squares optimization algorithm. An example is shown in figure A.2.

A similar procedure was also used to quantify the heights and widths of the most important single absorption peaks reported in this work, and the results are summarized in table A.2. The observed variation in sample temperature from measurement to measurement resulted in a small variation ($\pm 10\%$) in these parameters. The data presented in the table should therefore be taken as typical values.

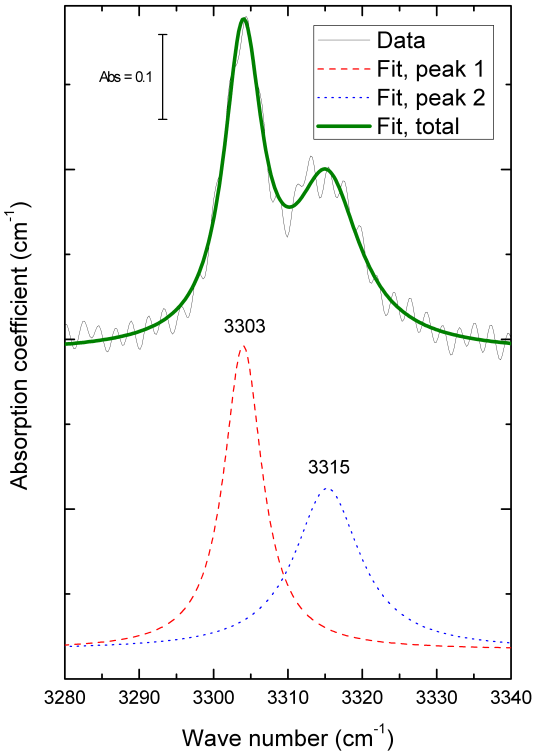

Figure A.2: Procedure used to separate the intensities of overlapping peaks, here shown for the peaks at 3303 and 3315 cm^{-1} measured in the $\vec{k}\|\vec{c}$ orientation of sample A-2 after annealing in mixed H_2/D_2 gas.

Peak (cm^{-1})	Sample	Treatment	Orientation	α_{max} (cm^{-1})	FWHH (cm^{-1})	$I = \int \alpha(\tilde{\nu})d\tilde{\nu}$ (cm^{-2})
2783	A-2	H_2/D_2	$\vec{k}\|\vec{c}$	1.49	1.91	3.73
3303	A-1	H_2	$\vec{k}\|\vec{c}$	0.43	5.00	2.59
3321	A-1	H_2	$\vec{k}\perp\vec{c}$	0.17	11.11	1.04
3336	B-1	As-grown	$\vec{k}\|\vec{c}$	0.52	2.61	1.55
3577	B-1	As-grown	$\vec{k}\perp\vec{c}$	0.65	2.38	1.73

Table A.2: Peak height (α_{max}), width (FWHH) and integrated intensity (I) for selected absorption peaks.

A.5 Documentation of Matlab scrips

The Matlab functions used for modeling the data from the isochronal annealing experiments are given below.

```
function I = Isochronal_anneal_fit(Xdata,Ydata)

%Ydata should be normalized, Xdata gives the annealing temperatures
%Starting parameters:
x01 = 9.8;
x02 = 12;  %c0=x01*10^x02 (Preexponential factor in s^(-1)
x03 = 2.8; %Activation energy in eV
x0 = [x01 x02 x03];

lb = [1 12 0.5];   % lower bound for parameters
hb = [9.999 14 8]; % higher bound for parameters
options = optimset('MaxFunEvals',100000); %Increase the number of iterations.

% Non-linear optimalization algoritm to fit Xdata and Ydata to the function
% defined in the function @Diss_fun using the parameters above:
[y,resnorm]=lsqcurvefit(@FOD_function,[x01 x02 x03],Xdata,Ydata,lb,hb,options);

%Print fitted paramters
c0=y(1)*10^(y(2))
Ea=y(3)
resnorm

% Calculate fitted values
k = 8.617343e-5;           % Boltzmanns constant in eV
I = zeros(length(Xdata),1);
I(1) = 1;
t_step = 30*3600;          % Annealing time step in seconds
for i=2:length(Xdata)
c=c0*exp(-Ea/(k*(Xdata(i)+273.15)));
I(i)=I(i-1)*exp(-c*t_step);
end

%Plot data and fit
figure;
plot(Xdata,Ydata,'ob');
hold on
plot(Xdata,I,'x','MarkerSize',20)
hold off

% Function that calculates the remaining concentration
% after each annealing step following a first order
% dissociation model with given parameters x:

function I = FOD_function(x,Xdata)

                      % c0 = x(1)*10^x(2)
                      % x(3) = activation energy in eV
k=8.617343e-5;        % boltzmanns constant in eV
I=zeros(length(Xdata),1);
I(1)=1;               % initial concentration
t=3600*30;            % time step in seconds

for i=2:length(Xdata)
c=x(1)*10^(x(2))*exp(-x(3)/(k*(Xdata(i)+273.15)));
I(i)=I(i-1)*exp(-c*t);
```

Bibliography

[1] J Nelson. *The Physics of Solar Cells*. Imperial College Press, 2007.

[2] V.A. Coleman and C.. Jagadish. *Basic Properties and Applications of ZnO*. Zinc Oxide Bulk, Thin Films and Nanostructures - Processing, Properties and Applications. Elsevier Ltd., 1st edition, 2006.

[3] U. Ozgur, Ya I. Alivov, C. Liu, A. Teke, M. A. Reshchikov, S. Dogan, V. Avrutin, S. J. Cho, and H. Morkoc. A comprehensive review of zno materials and devices. *Journal of Applied Physics*, 98(4):041301–103, 2005.

[4] M. D. McCluskey and S. J. Jokela. Defects in zno. *Journal of Applied Physics*, 106(7):071101, 2009.

[5] E. V. Monakhov and et al. Zinc oxide: bulk growth, role of hydrogen and schottky diodes. *Journal of Physics D: Applied Physics*, 42(15):153001, 2009.

[6] L. E. Halliburton, Lijun Wang, Lihua Bai, N. Y. Garces, N. C. Giles, M. J. Callahan, and Buguo Wang. Infrared absorption from oh- ions adjacent to lithium acceptors in hydrothermally grown zno. *Journal of Applied Physics*, 96(12):7168–7172, 2004.

[7] D. G. Thomas and J. J. Lander. Hydrogen as a donor in zinc oxide. *The Journal of Chemical Physics*, 25(6):1136–1142, 1956.

[8] Chris G. Van de Walle. Hydrogen as a cause of doping in zinc oxide. *Physical Review Letters*, 85(5):1012, 2000.

[9] Xiaonan Li, Brian Keyes, Sally Asher, S. B. Zhang, Su-Huai Wei, Timothy J. Coutts, Sukit Limpijumnong, and Chris G. Van de Walle. Hydrogen passivation effect in nitrogen-doped zno thin films. *Applied Physics Letters*, 86(12):122107–3, 2005.

[10] M. Wohlecke and L. Kovacs. Oh- ions in oxide crystals. *Critical Reviews in Solid State and Materials Sciences*, 26(1):1–86, 2001.

[11] G. Alvin Shi, Michael Stavola, and W. Beall Fowler. Identification of an oh-li center in zno: Infrared absorption spectroscopy and density functional theory. *Physical Review B (Condensed Matter and Materials Physics)*, 73(8):081201–3, 2006.

[12] R.J.D. Tilley. *Understanding Solids - The Science of Materials*. John Wiley and Sons Inc, 1st edition, 2004.

[13] B.G. Streetman and S.K. Banerjee. *Solid State Electronic Devices*. Pearson Education, Inc., 6th edition, 2006.

[14] P.R. Griffiths and J.A. de Haseth. *Fourier Transform Infrared Spectrometry*. John Wiley Sons, Inc., 2nd edition, 2007.

[15] H.D. Young and R.A. Freedman. *University Physics*. Pears Education, Inc., 11th edition, 2004.

[16] David Griffiths. *Introduction to Quantum Mechanics*. 2nd edition, 2004. March 31, 2004.

[17] Siegfried Wartewig. *IR and Raman Spectroscopy - Fundamental Processing*. WILEY-WHC Verlag GmbH and Co. KGaA, Weinheim, 2003.

[18] G. Rayner-Canham and T. Overton. *Descriptive Inorganic Chemistry*. W. H. Freeman and Company, 4th edition, 2006.

[19] Neil Ashcroft and David Mermin. *Solid State Physics*. Thomson Learning, 1976.

[20] Charles Kittel. *Introduction to Solid State Physics*. John Wiley and Sons, 2005.

[21] R.C. Newman. *Infra-red studies of crystal defects*. Taylor and Francis LTD, 1973.

[22] D.R. Lide. *CRC Handbook of chemistry and physics: A Read-Reference Book of Chemical and Physical Data*. CRC Press, 2004.

[23] P. Emelie, J. Phillips, B. Buller, and U. Venkateswaran. Free carrier absorption and lattice vibrational modes in bulk zno. *Journal of Electronic Materials*, 35(4):525–529, 2006.

[24] A. U. Kaufmann, A. P. Koidl, and A. O. F Schirmer. Near infrared absorption of ni2+ in zno and zns: dynamic jahn-teller effect in the 3t2 state. *Journal of Physics C: Solid State Physics*, 2:310, 1973.

[25] C. Klingshirn. *Semiconductor Optics*. Springer-Verlag Berlin, 3rd edition, 2007.

[26] W.L. Bond. Measurement of the refractive indices of several crystals. *Journal of Applied Physics*, 36(5), 1965.

[27] D. G. Thomas. Infrared absorption in zinc oxide crystals. *Journal of Physics and Chemistry of Solids*, 10(1):47–51, 1959.

[28] B.C. Smith. *Fundamentals of Fourier Transform Infrared Spectroscopy*. CRC Press, Inc., 1st edition, 1996.

[29] S. J. Pearton, D. P. Norton, K. Ip, Y. W. Heo, and T. Steiner. Recent progress in processing and properties of zno. *Progress in Materials Science*, 50(3):293–340, 2005.

[30] H.E. Jinlang and et al. *Electrical parameter statistic analysis and parallel coordination of ZnO varistors in low-voltage protection devices*, volume 20. Institute of Electrical and Electronics Engineers, New York, NY, ETATS-UNIS, 2005.

[31] Minami Tadatsugu. Transparent conducting oxide semiconductors for transparent electrodes. *Semiconductor Science and Technology*, 20(4):S35, 2005.

[32] John. F. Wager. Applied physics: Transparent electronics. *Science*, 300(5623):1245–1246, 2003.

[33] C. Liu, F. Yun, and H. MorkoÃS. Ferromagnetism of zno and gan: A review. *Journal of Materials Science: Materials in Electronics*, 16(9):555–597, 2005.

[34] Young Mok Cho, Woong Kil Choo, Hyojin Kim, Dojin Kim, and YoungEon Ihm. Effects of rapid thermal annealing on the ferromagnetic properties of sputtered zn(1-x)(co0.5fe 0.5)xo thin films. *Applied Physics Letters*, 80(18):3358–3360, 2002.

[35] R. Triboulet, V. Munoz-Sanjos, R. Tena-Zaera, M. Martinez-Tomas, and S. Hassani. *The Scope of Zinc Oxide Bulk Growth*. Zinc Oxide - A Material for Micro- and Optoelectronic Applications. 2005.

[36] D. Look. *Doping and Defects in ZnO*. Zinc Oxide Bulk, Thin Films and Nanostructures - Processing, Properties and Applications. Elsevier Ltd., 1st edition, 2006.

[37] A. F. Kohan, G. Ceder, D. Morgan, and Chris G. Van de Walle. First-principles study of native point defects in zno. *Physical Review B*, 61(22):15019, 2000.

[38] S. B. Zhang, S. H. Wei, and Alex Zunger. Intrinsic n-type versus p-type doping asymmetry and the defect physics of zno. *Physical Review B*, 63(7):075205, 2001.

[39] Fumiyasu Oba, Shigeto R. Nishitani, Seiji Isotani, Hirohiko Adachi, and Isao Tanaka. Energetics of native defects in zno. *Journal of Applied Physics*, 90(2):824–828, 2001.

[40] Anderson Janotti and Chris G. Van de Walle. Native point defects in zno. *Physical Review B (Condensed Matter and Materials Physics)*, 76(16):165202–22, 2007.

[41] F. Tuomisto, V. Ranki, K. Saarinen, and D. C. Look. Evidence of the zn vacancy acting as the dominant acceptor in n-type zno. *Physical Review Letters*, 91(20):205502, 2003.

[42] L. Vines, E. V. Monakhov, R. Schifano, W. Mtangi, F. D. Auret, and B. G. Svensson. Lithium and electrical properties of zno. *Journal of Applied Physics*, 107(10):103707–7, 2010.

[43] J. J. Lander. Reactions of lithium as a donor and an acceptor in zno. *Journal of Physics and Chemistry of Solids*, 15(3-4):324–334, 1960.

[44] A. Carvalho, A. Alkauskas, Alfredo Pasquarello, A. K. Tagantsev, and N. Setter. A hybrid density functional study of lithium in zno: Stability, ionization levels, and diffusion. *Physical Review B*, 80(19):195205, 2009.

[45] M. G. Wardle, J. P. Goss, and P. R. Briddon. Theory of fe, co, ni, cu, and their complexes with hydrogen in zno. *Physical Review B*, 72(15):155108, 2005.

[46] E. Lavrov, F. Borrnert, and J. Weber. *Hydrogen-Related Defects in ZnO Studied by IR Absorption Spectroscopy*. Zinc Oxide - A Material for Micro- and Optoelectronic Applications. 2005.

[47] Y. J. Li, B. Zhang, and W. Lu. Infrared absorption spectroscopy on oh–ni complex in hydrothermally grown zno. *Journal of Applied Physics*, 105(9):093516–6, 2009.

[48] H. J. Schulz and M. Thiede. Optical spectroscopy of 3d7 and 3d8 impurity configurations in a wide-gap semiconductor (zno:co,ni,cu). *Physical Review B*, 35(1):18, 1987.

[49] U. Wahl, E. Rita, J. G. Correia, T. Agne, E. Alves, and J. C. Soares. Lattice sites of implanted cu and ag in zno. *Superlattices and Microstructures*, 39(1-4):229–237, 2006.

[50] R. E. Dietz, H. Kamimura, M. D. Sturge, and A. Yariv. Electronic structure of copper impurities in zno. *Physical Review*, 132(4):1559, 1963.

[51] N. H. Nickel. Hydrogen migration in single crystal and polycrystalline zinc oxide. *Physical Review B*, 73(19):195204, 2006.

[52] K. M. Johansen, J. S. Christensen, E. V. Monakhov, A. Yu Kuznetsov, and B. G. Svensson. Deuterium diffusion and trapping in hydrothermally grown single crystalline zno. *Applied Physics Letters*, 93(15):152109–3, 2008.

[53] S. F. J. Cox, E. A. Davis, S. P. Cottrell, P. J. C. King, J. S. Lord, J. M. Gil, H. V. Alberto, R. C. Vilao, J. Piroto Duarte, N. Ayres de Campos, A. Weidinger, R. L. Lichti, and S. J. C. Irvine. Experimental confirmation of the predicted shallow donor hydrogen state in zinc oxide. *Physical Review Letters*, 86(12):2601, 2001.

[54] Detlev M. Hofmann, Albrecht Hofstaetter, Frank Leiter, Huijuan Zhou, Frank Henecker, Bruno K. Meyer, Sergei B. Orlinskii, Jan Schmidt, and Pavel G. Baranov. Hydrogen: A relevant shallow donor in zinc oxide. *Physical Review Letters*, 88(4):045504, 2002.

[55] E. V. Lavrov, F. Herklotz, and J. Weber. Identification of two hydrogen donors in zno. *Physical Review B (Condensed Matter and Materials Physics)*, 79(16):165210–13, 2009.

[56] A. Schildknecht, R. Sauer, and K. Thonke. Donor-related defect states in zno substrate material. *Physica B: Condensed Matter*, 340-342:205–209, 2003.

[57] Anderson Janotti and Chris G. Van de Walle. Hydrogen multicentre bonds. *Nat Mater*, 6(1):44–47, 2007.

[58] E. V. Lavrov, F. Borrnert, and J. Weber. Dominant hydrogen-oxygen complex in hydrothermally grown zno. *Physical Review B*, 71(3):035205, 2005.

[59] D. C. Look, B. Claflin, and H. E. Smith. Origin of conductive surface layer in annealed zno. *Applied Physics Letters*, 92(12):122108–3, 2008.

[60] C. H. Seager and S. M. Myers. Quantitative comparisons of dissolved hydrogen density and the electrical and optical properties of zno. *Journal of Applied Physics*, 94(5):2888–2894, 2003.

[61] J. Bang, E. A. Choi, and K. J. Chang. The effect of impurities on hydrogen bonding site and local vibrational frequency in zno. *Journal of Applied Physics*, 106(5):5, 2009.

[62] E. V. Lavrov, F. Borrnert, and J. Weber. Hydrogen motion in zno. *Physica B: Condensed Matter*, 401-402:366–369, 2007.

[63] Xian-Bin Li, Sukit Limpijumnong, Wei Quan Tian, Hong-Bo Sun, and S. B. Zhang. Hydrogen in zno revisited: Bond center versus antibonding site. *Physical Review B*, 78(11):113203, 2008.

[64] E. V. Lavrov. Infrared absorption spectroscopy of hydrogen-related defects in zno. *Physica B: Condensed Matter*, 340-342:195–200, 2003.

[65] S. J. Jokela and M. D. McCluskey. Unambiguous identification of nitrogen-hydrogen complexes in zno. *Physical Review B*, 76(19):193201, 2007.

[66] M. G. Wardle, J. P. Goss, and P. R. Briddon. Theory of li in zno: A limitation for li-based p -type doping. *Physical Review B*, 71(15):155205, 2005.

[67] Eun-Cheol Lee and K. J. Chang. Possible p -type doping with group-i elements in zno. *Physical Review B*, 70(11):115210, 2004.

[68] C. H. Park and D. J. Chadi. Hydrogen-mediated spin-spin interaction in zncoo. *Physical Review Letters*, 94(12):127204, 2005.

[69] H. J. Lee, C. H. Park, S. Y. Jeong, K. J. Yee, C. R. Cho, M. H. Jung, and D. J. Chadi. Hydrogen-induced ferromagnetism in zncoo. *Applied Physics Letters*, 88(6):062504–3, 2006.

[70] F. G. Gartner and E. Mollwo. Ir absorption of oh and od centres and oh/oh, od/od, and oh/od complexes in cu-doped zno single crystals. *physica status solidi (b)*, 89(2):381–388, 1978.

[71] F. Borrnert, E. V. Lavrov, and J. Weber. Hydrogen motion in the cu-h complex in zno. *Physical Review B*, 75(20):205202, 2007.

[72] E. V. Lavrov, J. Weber, and F. Borrnert. Copper dihydrogen complex in zno. *Physical Review B (Condensed Matter and Materials Physics)*, 77(15):155209–10, 2008.

[73] E. V. Lavrov. Hydrogen in zno. *Physica B: Condensed Matter*, 404(23-24):5075–5079, 2009.

[74] G. Alvin Shi, Marjan Saboktakin, Michael Stavola, and S. J. Pearton. "hidden hydrogen" in as-grown zno. *Applied Physics Letters*, 85(23):5601–5603, 2004.

[75] E. V. Lavrov, F. Herklotz, and J. Weber. Identification of hydrogen molecules in zno. *Physical Review Letters*, 102(18):185502–4, 2009.

[76] G. Alvin Shi, Michael Stavola, S. J. Pearton, M. Thieme, E. V. Lavrov, and J. Weber. Hydrogen local modes and shallow donors in zno. *Physical Review B*, 72(19):195211, 2005.

[77] E. V. Lavrov, J. Weber, F. Borrnert, Chris G. Van de Walle, and R. Helbig. Hydrogen-related defects in zno studied by infrared absorption spectroscopy. *Physical Review B*, 66(16):165205, 2002.

[78] E.L. Dereniak and G.D. Boreman. *Infrared Detectors and Systems*. John Wiley and Sons, 1st edition, 1996.

[79] D. G. Brandon and W. D. Kaplan. *Microstructural characterization of materials*. John wiley and Sons, Ltd, 1st edition, 1999.

[80] SPC Goodwill. Hydrothermally grown single crystal zno substrates - data sheet, http://www.spcgoodwill.com/catalog$_f$.html, 2010.

[81] S. Lew, A.F. Sarofim, and M. Flytzani-Stephanopoulos. The reduction of zinc titanate and zinc oxide solids. *Chemical Engineering Science*, 47(6):1421–1431, 1992.

[82] Schroeder D.V. *An Introduction to Thermal Physics*. Addison Wesley Longman, 2000.

[83] J. Crank. *The mathematics of diffusion*. Oxford University Press, 2nd edition, 1980.

[84] S. J. Jokela, M. D. McCluskey, and K. G. Lynn. Infrared spectroscopy of hydrogen in annealed zinc oxide. *Physica B: Condensed Matter*, 340-342:221–224, 2003.

[85] Hans Bjorge Normann. *A Fourier transform infrared absorption study of hydrogen and deuterium in hydrothermal ZnO, Master thesis*. University of Oslo, 2008.

[86] O. W. Johnson, John DeFord, and J. W. Shaner. Experimental technique for the precise determination of h and d concentration in rutile (tio[sub 2]). *Journal of Applied Physics*, 44(7):3008–3012, 1973.

[87] S. Klauer, M. Wohlecke, and S. Kapphan. Isotope effect of protonic conductivity in linbo3. *Radiation Effects and Defects in Solids: Incorporating Plasma Science and Plasma Technology*, 119(2):699 – 704, 1991.

[88] P. Beneventi and et al. Ftir spectroscopy of oh stretching modes in bso, bgo and bto sillenites. *Journal of Physics: Condensed Matter*, 6(31):6329, 1994.

[89] R. Schifano, E. V. Monakhov, L. Vines, B. G. Svensson, W. Mtangi, and F. D. Auret. Defects in virgin hydrothermally grown n-type zno studied by temperature dependent hall effect measurements. *Journal of Applied Physics*, 106(4):043706–7, 2009.

[90] S. J. Jokela and M. D. McCluskey. Structure and stability of o-h donors in zno from high-pressure and infrared spectroscopy. *Physical Review B*, 72(11):113201, 2005.

[91] J. Pankove. *Optical processses in semiconductors*. Prentice-Hall, Inc., 1971.

[92] Philip M. Morse. Diatomic molecules according to the wave mechanics. ii. vibrational levels. *Physical Review*, 34(1):57, 1929.

[93] K. S. Seshadri and R. Norman Jones. The shapes and intensities of infrared absorption bands–a review. *Spectrochimica Acta*, 19(6):1013–1085, 1963.